Geodynamics of Earth's Deep Mantle

Thesis by

Dan J. Bower

In Partial Fulfillment of the Requirements

for the Degree of

Doctor of Philosophy

California Institute of Technology

Pasadena, California

2012

(Defended May 1st, 2012)

Geology is the study of pressure and time. That's all it takes really, pressure, and time. That, and a big goddamn poster.

—*Ellis Boyd 'Red' Redding, The Shawshank Redemption*

Acknowledgements

Embarking on an intrepid voyage of discovery to the deep Earth would not have been possible without the inspiring guidance of my Navigation Officer, Mike Gurnis. I thank you for posing thought-provoking, challenging, and diverse research questions and ensuring safe passage through uncharted waters. Whenever I felt lost at sea our discussions would invariably steer me back on course. Furthermore, I appreciate the supportive, collaborative, and vibrant research environment that you foster and your timely, focused feedback on manuscripts.

I am most grateful to Jennifer Jackson for ensuring that I did not run aground in the shallow waters of mineral physics. And Don Helmberger for instilling confidence that I would not capsize in the unpredictable waves of seismology. Additionally, thanks for your frequent reminders that "the Earth is real complicated". The freedom to venture into these disciplines greatly broadened my depth of knowledge and ability to tackle multifaceted research problems.

My watchmen, Paul Asimow and Dave Stevenson, ensured plain sailing by maintaining a clear view of the horizon to spot uncertain weather and hazards from afar. I appreciate your measured advice, and several of your insights and suggestions feature in this Captain's Log. Field trip leaders including Jason Saleeby, John Eiler,

Jean-Philippe Avouac, Rob Clayton, and Joann Stock, enticed me to flirt with the "shallow subsurface" (less than 670 km depth), although my heart always remained true to structure below the transition zone.

Senior explorers, Drs. Eh Tan and Daoyuan Sun, graciously provided mentorship and expertise when I was a fledgling adventurer learning the ropes. A gifted and extensive crew also offered encouragement throughout the mission: in particular, discussions with Dr. Lijun Liu, June Wicks, Aaron Wolf, and Laura Alisic uncovered common ground between my own research and other fields. My office mates and I engaged in stimulating discussions and good-spirited humor: Dr. Eun-Seo Choi, Dr. Ravi Kanda, Dr. Michelle Selvans, Zhongwen Zhan, Dongzhou Zhang, Yingdi Luo, and Chris Rollins.

The warm and positive atmosphere within the Seismological Laboratory and GPS division solidifies their reputation as truly extraordinary venues for conducting research. This environment is amplified by the thoughtful and caring staff, including Viola Carter and Dian Buchness. I thank the Computational Infrastructure for Geodynamics (CIG), GPlates developers, and collaborators at the University of Sydney, for supplying source code and datasets. I am grateful to Naveed Near-Ansari, John Lilley, Mike Black, and Scott Dungan for their exceptional administration of computing resources and rapid response to e-mail queries. Mark Turner introduced me to the power of Python and programming paradigms.

Involvement with numerous campus organizations and activities ensured that I remained on an even keel during my journey to the deep Earth. These include athletic

endeavours, dance, social and environmental activism, and student council. Through these activities I have built a global friendship circle of talented individuals who passionately champion a cause alongside their academic obligations. It is impossible to acknowledge the many friendships that enrich my life; for brevity I include the Chapmans, Matzens, Kelbers (soon to be), Dolbys (also soon to be), Steve Chemtob, and Kristin Phillips. I thank Pratyush Tiwary and Patrick Sanan for spearheading regular exoduses to mountainous terrain and the camaraderie within the Caltech Alpine Club.

Frequent radio contact with friends and family at my home port helped me to ride out stormy weather during my adventure. I am indebited to my parents and sister for always believing I could walk on water and enabling me to venture to the new world. I remain buoyed up by your love and support. Final thanks to my stowaway, Danielle Bower, for providing endless distractions en route, and for sailing into the sunset with me.

Abstract

Seismic tomography and waveform modeling reveal several prominent structures in the Earth's lower mantle: (1) the D″ discontinuity, defined by a seismic velocity increase of 1–3% about 250 km above the core-mantle boundary (CMB), (2) Ultralow-velocity zones (ULVZs), which are thin, isolated patches with anomalously low seismic wavespeed at the CMB, and (3) two large, low-shear velocity provinces (LLSVPs) beneath Africa and the Pacific Ocean. The geodynamics of these structures are investigated using numerical convection models that include new discoveries in mineral physics and recent insight from seismology. In addition, I assess the influence of an iron spin transition in a major lower mantle mineral (ferropericlase) on the style and vigor of mantle convection.

A phase change model for the D″ discontinuity produces significant thermal and phase heterogeneity over small distances due to the interaction of slabs, plumes, and a phase transition. Perturbations to seismic arrivals are linked to the evolutionary stage of slabs and plumes and can be used to determine phase boundary properties, volumetric wavespeed anomaly beneath the discontinuity, and possibly the lengthscale of slab folding near the CMB.

I simulate convection within D″ to deduce the stability and morphology of a

chemically distinct iron-enriched ULVZ. The chemical density anomaly largely dictates ULVZ shape, and the prescribed initial thickness (proxy for volume) of the chemically distinct layer controls its size. I synthesize the dynamic results with a Voigt-Reuss-Hill mixing model to provide insight into the inherent seismic trade-off between ULVZ thickness and wavespeed reduction.

The dynamics of the LLSVPs are investigated using global 3-D models of thermochemical structures that incorporate paleogeographic constraints from 250 Ma to present day. The structures deform and migrate along the CMB, either by coupling to plate motions or in response to slab stresses. Slabs from Paleo-Tethys and Tethys Ocean subduction push the African structure further to the southwest than inferred from tomography. Dense and viscous slabs can severely compromise the stability of thermochemical structures with a high bulk modulus at the CMB.

Finally, I explore the consequences of the intrinsic density change caused by the Fe^{2+} spin transition in ferropericlase on the style and vigor of mantle convection. The transition generates a net driving density difference for both upwellings and downwellings that dominantly enhances the positive thermal buoyancy of plumes in 2-D cylindrical geometry. Although the additional buoyancy does not fundamentally alter large-scale dynamics, the Nusselt number increases by 5–10%, and vertical velocities increase by 10–40% in the lower mantle. Advective heat transport is more effective and temperatures in the CMB region are reduced by up to 12%.

Contents

List of Figures

List of Tables

Chapter 1

Introduction

Unveiling the nature of the deep Earth demands a multidisciplinary approach and there are exciting new research directions at the intersection of mineral physics, seismology, and geodynamics. Seismic methods provide the most comprehensive sampling of the mantle and constrain wavespeeds, the sharpness of features, and the geographical distribution of heterogeneity. The dominant lower mantle minerals are aluminous ferromagnesian silicate perovskite, (Mg,Fe,Al)(Si,Al)O_3, and magnesium iron oxide, (Mg,Fe)O, which occupy about 75 and 15 volume percent of the lower mantle, respectively (*Ringwood*, 1991). Recent advancements in mineral physics, notably diamond anvil cell technology, are enabling experimentalists to determine the wavespeeds and material properties of these phases to compare with seismic and dynamic inferences. New discoveries in the behavior of (Mg,Fe)SiO_3 and (Mg,Fe)O at extreme conditions motivate the research presented in three chapters of this thesis. Convection calculations elucidate how mass and heat transfer influence the morphology, stability, and longevity of structures in the mantle.

The core-mantle boundary (CMB) (3300–4400 K) separates the liquid iron-rich outer core from the solid silicate mantle at $\sim$ 2890 km depth (e.g., *Lay et al.*, 2008).

This interface defines the largest contrast in material and dynamic properties in the Earth. The high viscosity subsolidus lower mantle deforms by slow, creeping flow ($\sim$ 1 cm/yr) (e.g., *Davies*, 1999), whereas the inviscid outer core is rapidly convecting ($\sim$ 1 mm/s) (e.g., *Glatzmaier and Roberts*, 1995). Heat transfer across the CMB occurs predominantly by conduction and mass exchange is negligible. Total heat flow from the core to the mantle controls the power available to drive the geodynamo, the cooling rate of the core, and the growth rate of the inner core. The outer core boundary behaves as an isothermal free-slip surface to mantle convection because of the vastly different timescales associated with core and mantle dynamics.

Seismic waveform modeling elucidates the fine-scale features of the CMB region through the analyses of wavetrains that arrive before or after well-identified reference phases on seismograms. These wavetrains are sometimes visible on individual seismograms or may require data stacking to increase the signal-to-noise ratio. Arrivals with neighboring raypaths can be analyzed together to eliminate source dependency and constrain mantle heterogeneity along a particular segment of a propagation path. Waveform modeling can often distinguish between volumetric heterogeneity and sharp seismic gradients and has proven instrumental in shaping our view of the CMB region.

Lay and Helmberger (1983) discovered the D$''$ discontinuity, a seismic interface characterized by a shear velocity increase of 1–3% approximately 250 km above the CMB. The boundary is inferred from an extra phase, known as SdS, that arrives between the direct S-wave, S, and the core-reflected S-wave, ScS, at post-critical distances. SdS turns in the higher velocity layer below the discontinuity, which produces

a triplication in seismic data. Seismologists identify the triplication beneath regions of inferred paleosubduction including Alaska, the Caribbean, Central America, India, and Siberia. Detections beneath the seismically slow central Pacific are contrary to this trend and may suggest that the discontinuity height above the CMB or velocity increase are modulated by composition.

There are three probable explanations for the discontinuity, which are not necessarily mutually exclusive: phase change, thermal heterogeneity, or a chemical boundary. A phase change best explains the seismic data (*Sidorin et al.*, 1998). Contary to observations, thermal heterogeneity alone does not produce a strong SdS arrival, and a pre-existing chemical layer is pushed away from downwelling regions. Subsequent experimental and theoretical verification of a phase transition in $MgSiO_3$ from silicate perovskite, the major phase of the lower mantle, to a new phase, termed "post-perovskite", supports the phase change interpretation (*Murakami et al.*, 2004; *Oganov and Ono*, 2004). Furthermore, a "double crossing" of the phase boundary may explain neighboring seismic discontinuities (*Hernlund et al.*, 2005).

In Chapter 2 I investigate the fine-scale interaction of a slab as it descends through the phase transition and perturbs the thermal boundary layer at the CMB. The temperature anomalies of slabs and plumes elevate and suppress the phase boundary, respectively. I elucidate the expected perturbations to temperature and phase that map to variations in seismic structure and produce waveform complexity in synthetic seismograms. Modern three-component broadband seismic arrays such as USArray will provide data to compare with the predictions.

Ultralow-velocity zones (ULVZs) are thin ($<$ 100 km), isolated patches with anomalously low seismic wavespeed (reductions of $\sim$ 10–30%) at the CMB originally detected beneath the western Pacific but since discovered in other regions. They were identified by the late arrival of the seismic phase SPdKS relative to SKS for distances between 105 and 120 degrees. SKS travels through the mantle and outer core and SPdKS follows a similar path except for a short diffracted segment (Pd) along the CMB. Waveform modeling using differential travel time and amplitude therefore constrains the P-wave velocity for this segment. Additionally, precursors and postcursors to core-reflected phases (PcP, ScP, ScS) can potentially constrain the P and S wavespeed, thickness, and density of ULVZs, although data stacking is required to enhance the signal-to-noise ratio.

Iron enrichment of solid phases, specifically the increase in Fe/(Fe+Mg) ratio, can simultaneously increase density and reduce compressional and shear velocity (e.g., *Karato and Karki*, 2001). This partly inspired the notion of solid, iron-rich ULVZs, such as a metal-bearing layer (*Knittle and Jeanloz*, 1991; *Manga and Jeanloz*, 1996), subducted banded iron formations (*Dobson and Brodholt*, 2005), or iron-enriched post-perovskite (*Mao et al.*, 2006; *Stackhouse and Brodholt*, 2008). Iron-rich systems are typically denser than the surrounding mantle, which is required to explain the locations of ULVZs at the base of the mantle.

Recent high-pressure experiments have uncovered very low sound velocities in iron-rich (Mg,Fe)O that could explain the origin of some ULVZs (*Wicks et al.*, 2010). I explore this hypothesis in Chapter 3 by developing a thermochemical convection model

of a solid-state ULVZ that contains a small volume fraction of iron-rich (Mg,Fe)O. A mineral physics mixing model combines the material properties for the oxide phase and ambient material using select chemical partitioning models to determine the thermoelastic parameters of the assemblage. The model satisfies current seismic modeling constraints.

The behavior of (Mg,Fe)O at high pressure and temperature conditions also motivates the study presented in Chapter 4. A high-spin (four unpaired d electrons) to low-spin (no unpaired d electrons) electronic transition of ferrous iron in an octahedral local environment increases the density of (Mg,Fe)O ferropericlase by 2–4% at mid-lower mantle pressure around 50 GPa (*Sturhahn et al.*, 2005; *Badro et al.*, 2003). This transformation occurs over a pressure range that is small at ambient temperature ($\sim$ 300 K) and broad at high temperature ($\sim$ 3000 K). The spin transition is continuous along a lower mantle geotherm (*Sturhahn et al.*, 2005; *Tsuchiya et al.*, 2006). However, downwellings and upwellings may generate substantial temperature anomalies in the mantle, so that convective flow may be modified by buoyancy forces arising through the spin-state of the material.

I investigate how the spin transition in (Mg,Fe)O impacts the large-scale style and vigor of mantle convection in Chapter 4. The body-force due to the spin-state of the material is included in the momentum equation. To determine the influence of the spin transition I observe the pattern of convection, time average heat flux, and time average depth profiles for the horizontally averaged temperature and RMS vertical velocity.

Seismic tomography reveals two antipodal large, low-shear velocity provinces (LLSVPs) at the base of the mantle beneath the Pacific Ocean and Africa. The circum-Pacific belt of fast material is attributed to relic slabs from paleosubduction (*Richards and Engebretson*, 1992). The LLSVPs occupy approximately 20% of the surface area of the CMB and contain about 1.6 vol. % and 1.9 mass % of the mantle (e.g., *Burke et al.*, 2008). *Ni and Helmberger* (2003a) model the 3-D geometry of the African LLSVP as a ridge-like structure approximately 1200 km high and 1000 km wide that extends 7000 km from central Africa to the Indian Ocean. The Pacific LLSVP may be divided into a western province that is 1000 km wide and rises 740 km above the CMB and an eastern section that is 1800 km wide and 340–650 km high (*He and Wen*, 2009).

A thermochemical origin is necessary to explain anti-correlated shear wave and bulk sound velocity anomalies (*Su and Dziewonski*, 1997; *Masters et al.*, 2000), putative anti-correlated shear wave and density anomalies (*Ishii and Tromp*, 1999, 2004), multipathing for waves sampling its steep edges (*Ni et al.*, 2002), and geological inferences of stability over 200–300 Myr (*Burke and Torsvik*, 2004). These observations are suggestive of a material with a higher bulk modulus and higher zero-pressure density than ambient mantle (*Tan and Gurnis*, 2005). Furthermore, surface plate history influences the morphology and location of the LLSVPs (*McNamara and Zhong*, 2005).

In Chapter 5 I investigate the response of high bulk modulus structures in the lower mantle to evolving surface tectonics from 250 Ma to present day. A novel time-dependent thermal and kinematic boundary condition is derived from a high-

resolution plate history model that encodes global plate motions and paleosubduction locations. These paleogeographic constraints are incorporated into 3-D spherical convection models with a high bulk modulus material with a higher zero-pressure density than ambient mantle.

Chapter 2

Dynamic origins of seismic wavespeed variation in D″

To be submitted as:

Bower, D. J., M. Gurnis, and D. Sun (2012), Dynamic origins of seismic wavespeed variation in D″, *Phys. Earth Planet. In.*

2.1 Abstract

The D″ discontinuity is defined by a seismic velocity increase of 1–3% about 250 km above the core-mantle boundary (CMB), and is mainly detected beneath locations of inferred paleosubduction. A phase change origin for the interface can explain a triplicated arrival observed in seismic waveform data and is supported by the recent discovery of a post-perovskite phase transition. We investigate the interaction of slabs, plumes, and the phase change within D″ in 2-D compressible convection calculations, and predict waveform complexity in synthetic seismic data. The dynamic models produce significant thermal and phase heterogeneity in D″ over small distances and reveal a variety of behaviors including: (1) distinct pPv blocks separated by upwellings, (2) notches at the top of a pPv layer caused by plume heads, (3)

regions of Pv embedded within a pPv layer due to upwellings. Advected isotherms produce complicated thermal structure that enable multiple crossings of the phase boundary. Perturbations to S, SdS, and ScS arrivals (distances < 84 degrees) are linked to the evolutionary stage of slabs and plumes, and can be used to determine phase boundary height and velocity increase, volumetric wavespeed anomaly beneath the discontinuity, and possibly the lengthscale of slab folding near the CMB. Resolving fine-scale structure beneath the interface requires additional seismic phases (e.g., Sd, SKS) and larger distances (> 80 degrees).

2.2 Introduction

The D″ discontinuity is characterized by a seismic velocity increase of 1–3% approximately 250 kilometers above the core-mantle boundary (CMB) (see review by *Wysession et al.*, 1998). Seismic waveform modeling detects a velocity jump beneath locations of inferred paleosubduction, including Alaska, the Caribbean, Central America, India, and Siberia. Furthermore, in seismic tomography the high velocity and deep anomalies in these regions are interpreted as slabs (e.g., *Grand*, 2002).

The discontinuity can explain a triplicated arrival SdS (PdP) between S (P) and ScS (PcP) observed in waveform data (*Lay and Helmberger*, 1983). Between epicentral distances 65–83 degrees, SdS is a composite arrival from a discontinuity reflection Sbc (Pbc) and a ray turning below the interface Scd (Pcd). The horizontally-polarized S-wave (SH) triplicated arrival is often analyzed at ~ 10 s period and is not contaminated by other phases or mode conversions. Shorter periods (~ 1 s) can detect the

P-wave triplication (PdP) but data stacking is required to suppress noise.

There are generally fewer or weaker SdS (PdP) detections outside high-velocity areas which suggests subduction history influences the presence and strength of the arrival. In contrast to seismic observations, a pre-existing basal chemical layer generates strong (weak) SdS below upwellings (downwellings) (*Sidorin and Gurnis*, 1998; *Sidorin et al.*, 1998) and does not generate short wavelength heterogeneity on the discontinuity (*Tackley*, 1998). However, detections of SdS beneath the seismically slow central Pacific suggest the discontinuity height above the CMB or velocity increase may be modulated by composition in some regions (*Garnero et al.*, 1993a).

Early dynamic calculations and waveform modeling propose a thermal slab interacting with a phase change with a positive Clapeyron slope can explain the origin of the D″ discontinuity (*Sidorin et al.*, 1999a, 1998). Incident rays are refracted by a high velocity thermal slab above D″ and turn beneath the discontinuity in the higher velocity phase to produce the SdS arrival. Furthermore, a high-temperature thermal boundary layer generates a negative seismic velocity gradient at the CMB. This counteracts the velocity step to ensure that differential travel times (e.g., ScS–S) and diffracted waveforms match data (*Young and Lay*, 1987, 1990). *Sidorin et al.* (1999b) unify regional seismic models from waveform studies by proposing a global discontinuity with an ambient phase change elevation of 200 km above the CMB and a Clapeyron slope of 6 MPa K^{-1}. The actual boundary locally is thermally perturbed upward and downward.

The subsequent discovery of a phase transition in $MgSiO_3$ from silicate perovskite

(Pv) to "post-perovskite" (pPv) at CMB conditions supports the phase change hypothesis (*Murakami et al.*, 2004; *Oganov and Ono*, 2004). *Ab initio* calculations at 0 K suggest that the transformation of isotropic aggregates of Pv to pPv increases the S-wave velocity by 1–1.5% and changes the P-wave velocity by -0.1–0.3% (*Oganov and Ono*, 2004; *Tsuchiya et al.*, 2004; *Iitaka et al.*, 2004). First principle calculations at high temperature produce similar wavespeed variations (*Stackhouse et al.*, 2005; *Wentzcovitch et al.*, 2006), and high pressure experiments resolve a 0–0.5% increase in S-wave velocity (*Murakami et al.*, 2007). Lattice-preferred orientation in the pPv phase may reconcile the small variation in wavespeeds from mineral physics with the 1–3% increase across the D″ discontinuity deduced from seismic data (e.g., *Wookey et al.*, 2005). Fe content in Pv may decrease (*Mao et al.*, 2004) or increase (*Tateno et al.*, 2007) the phase transition pressure, and Al may broaden the mixed phase region (*Catalli et al.*, 2010; *Akber-Knutson et al.*, 2005). However, other researchers find that compositional variations have little effect (*Hirose et al.*, 2006; *Murakami et al.*, 2005). Independent of the width of the mixed phase region, strain-partitioning into weak pPv can produce a sharp seismic discontinuity due to the rapid change in seismic anisotropy (*Ammann et al.*, 2010).

The phase transformation destabilizes the lower thermal boundary layer, which produces more frequent upwellings (*Sidorin et al.*, 1999a; *Nakagawa and Tackley*, 2004). A dense basal layer interacting with a chemically heterogeneous slab and the Pv-pPv transition produces strong lateral gradients in composition and temperature that may also explain finer structure within D″ (*Tackley*, 2011). A "double crossing"

of the phase boundary occurs when pPv transforms back to Pv just above the CMB and may explain neighboring seismic discontinuities (*Hernlund et al.*, 2005). However, the precritical reflection from the second putative phase transition is a relatively low amplitude arrival and therefore difficult to detect (*Flores and Lay*, 2005; *Sun et al.*, 2006). The Clapeyron slope and transition temperature (or pressure) control the topography of the pPv layer (e.g., *Monnereau and Yuen*, 2007),

The CMB beneath Central America is illuminated through the propagation of seismic waves along a narrow corridor from South American subduction zone events to broad-band networks in North America. Furthermore, seismic tomography and plate reconstructions indicate deeply penetrating slab material (e.g., *Grand*, 2002; *Ren et al.*, 2007). Under the Cocos Plate, the D″ discontinuity can be modeled at constant height above the CMB with S-wave variations of 0.9–3.0% (*Lay et al.*, 2004; *Ding and Helmberger*, 1997) or as an undulating north–south dipping structure from 300 km to 150 km above the CMB with constant D″ velocity (*Thomas et al.*, 2004). The Pv-pPv transition may account for the positive jump seen in S-wave models and smaller negative P-wave contrast (*Hutko et al.*, 2008; *Kito et al.*, 2007; *Wookey et al.*, 2005). Furthermore, its interaction with a buckled slab may explain an abrupt 100 km step in the discontinuity (*Sun and Helmberger*, 2008; *Hutko et al.*, 2006; *Sun et al.*, 2006). A second deeper negative reflector appears in some locations about 200 km below the main discontinuity. This may originate from the base of a slab, a plume forming beneath a slab (*Tan et al.*, 2002), back-transformation of pPv-Pv, chemical layering (*Kito et al.*, 2007; *Thomas et al.*, 2004), or out-of-plane scatterers (*Hutko*

et al., 2006).

It is now timely to reanalyze the role of slabs in the deep mantle and their seismic signature following discovery of the Pv-pPv transformation and a proposed "double crossing" of the phase boundary. In this study we follow a similar approach to *Sidorin et al.* (1998) using a compressible formulation and viscoplastic rheology. Compressibility promotes an irregular, more sluggish, flow field and encourages greater interaction between upper and lower boundary instabilities (*Steinbach et al.*, 1989). Viscous heating redistributes buoyancy sources (*Jarvis and McKenzie*, 1980) and latent heat can reverse phase boundary distortion caused by the advection of ambient temperature (*Schubert et al.*, 1975). These non-Boussinesq effects could play an important role in determining the lateral variations in temperature and phase that may give rise to rapidly varying waveforms. Using constraints from experimental and theoretical mineral physics we predict seismic wavespeed structure from the temperatures and phases determined by the convection calculations. Finally, we compute synthetic seismograms to analyze S, SdS, and ScS arrivals.

2.3 Numerical convection models

2.3.1 Equations

We employ the truncated anelastic liquid approximation (TALA) for infinite-Prandtl-number flow (*Jarvis and McKenzie*, 1980; *Ita and King*, 1994) with a divariant phase change using CitcomS (*Zhong et al.*, 2000; *Tan et al.*, 2007). The conservation equa-

tions of mass, momentum, and energy (non-dimensional) are:

$$(\bar{\rho}u_i)_{,i} = 0 \tag{2.1}$$

$$-P_{,i} + \tau_{ij,j} = (Rb\Gamma - Ra\bar{\rho}\bar{\alpha}T)\bar{g}\delta_{ir} \tag{2.2}$$

$$\tau_{ij} = \eta\left(u_{i,j} + u_{j,i} - \frac{2}{3}u_{k,k}\delta_{ij}\right) \tag{2.3}$$

$$\bar{\rho}c'(T_{,t} + u_i T_{,i}) = \bar{\rho}\bar{c}\bar{\kappa}T_{,ii} - \bar{\rho}\bar{g}\alpha' u_r Di(T + T_S) + \frac{Di}{Ra}\tau_{ij}u_{i,j} + \bar{\rho}H \tag{2.4}$$

where ρ is density, u velocity, P dynamic pressure, τ deviatoric stress tensor, Ra thermal Rayleigh number, α thermal expansivity, T temperature, Rb phase Rayleigh number, Γ phase function, g gravitational accceleration, η viscosity, t time, c heat capacity, κ thermal diffusivity, T_S surface temperature, $Di = \alpha_0 g_0 R_0/c_{p0}$ dissipation number, and H internal heat production rate. Depth-dependent reference state parameters are denoted by overbars, and the r subscript denotes a unit vector in the radial direction. Phase buoyancy and latent heat are included using a phase function Γ, effective heat capacity c', and effective thermal expansivity α' (*Richter*, 1973; *Christensen and Yuen*, 1985), defined as:

$$\Gamma(p_h, T_\Gamma) = \frac{1}{2}\left(1 + \tanh\left(\frac{p_h - p_\Gamma - \gamma(T - T_\Gamma)}{d}\right)\right) \tag{2.5}$$

$$\alpha'/\bar{\alpha} = 1 + \gamma\frac{Rb}{Ra}\frac{\partial\Gamma}{\partial p_h} \tag{2.6}$$

$$c'/\bar{c} = 1 + Di(T + T_S)\gamma^2\frac{Rb}{Ra}\frac{\partial\Gamma}{\partial p_h} \tag{2.7}$$

where (p_Γ, T_Γ) is the reference pressure and temperature of the phase transition, γ Clapeyron slope, d phase transition width, and p_h hydrostatic pressure. The phase function $\Gamma = 0$ for Pv and $\Gamma = 1$ for pPv.

The thermal Rayleigh number, Ra is defined by dimensional surface values:

$$Ra = \frac{\rho_0 \alpha_0 \Delta T {R_0}^3 g_0}{\eta_0 \kappa_0}. \tag{2.8}$$

Our Ra is therefore about an order-of-magnitude larger than a definition with mantle thickness (Table 2.1).

2.3.2 Rheology

We use a temperature-dependent viscosity, governed by an Arrhenius law, and with plastic yielding to generate a mobile upper surface and strong slabs (*Moresi and Solomatov*, 1998; *Tackley*, 2000):

$$\eta(T) = \exp\Big(\frac{20}{T+1} - \frac{20}{2}\Big). \tag{2.9}$$

The reference viscosity η_0 is defined at the CMB ($T = 1$). We define the strength envelope of the lithosphere using Byerlee's Law (*Byerlee*, 1978):

$$\sigma(r) = \min[a + b(1-r), \sigma_y] \tag{2.10}$$

where r is the radius, σ yield stress, a cohesion, b brittle stress gradient, and σ_y ductile yield stress. The effective viscosity η_{eff} is computed by:

$$\eta_{\text{eff}} = \min\left[\eta(T), \frac{\sigma_r(r)}{2\dot{\epsilon}}\right] \tag{2.11}$$

where $\dot{\epsilon}$ is the second invariant of the strain rate tensor.

The cohesion is set to a small value $a = 1 \times 10^4$, and remains constant to limit the number of degrees of freedom. We define a yield stress envelope characterized by brittle failure from the surface to 160 km depth and ductile failure for greater depths ($b = 40\sigma_y$). Preliminary models reveal $b = 1.6 \times 10^9$ produces plate-like behavior with strong downwellings.

2.3.3 Model setup

We solve the conservation equations in a 2-D cylindrical section (2 radians) with free-slip and isothermal upper and lower surfaces and zero heat flux sidewalls. Internal heating is neglected ($H = 0$). Radial mesh refinement provides the highest resolution of 14 km within the thermal boundary layers and the lowest resolution of 40 km in the mid-mantle. Lateral resolution is 0.45 degrees (50 and 28 km at the top and bottom, respectively).

We construct a depth-dependent reference state for density using a polynomial fit to PREM in the lower mantle (*Solheim and Peltier*, 1990; *Dziewonski and Anderson*, 1981). The pressure-dependence of the thermal expansion coefficient is derived from experimental data for $MgSiO_3$ (*Mosenfelder et al.*, 2009) and varies by approximately

a factor of 4 across the mantle. Gravity and heat capacity are approximately constant throughout the mantle and therefore we adopt uniform profiles. Thermal conductivity is likely dependent on pressure and temperature, although there are significant uncertainties, particularly in multi-phase and chemically complex systems. We choose to neglect this complexity by assigning the same thermal conductivity to Pv and pPv independent of pressure.

The initial condition is derived from a precalculation (extended-Boussinesq) with similar parameters (Table 2.1) while excluding the phase transition. This reduces the spin-up time for the TALA model. We integrate the model for several 10,000s of time steps (dimensionally several Gyr) such that the initial condition no longer affects our results.

2.3.4 Post-perovskite phase transition

We set the ambient phase transition temperature ($T_\Gamma = 2600$ K) to the horizontally averaged temperature 300 km above the CMB in the precalculation. The free parameters are the ambient phase transition pressure p_Γ and the Clapeyron slope γ, which we vary to explore a range of dynamic scenarios and consequences for seismic wave propagation. The Clapeyron slope is varied between 7.5 MPa K^{-1} and 13.3 MPa K^{-1}, which is consistent with geophysical constraints (*Hernlund and Labrosse*, 2007) and mineral physics theory and experiment (see review by *Shim*, 2008). *Sidorin et al.* (1999b,a) favor a Clapeyron slope of 6 MPa K^{-1}, although larger values fit the data nearly as well.

The interaction of a simple conductive geotherm with the phase transition can produce a double crossing of the phase boundary (*Hernlund et al.*, 2005). Ambient mantle enters the pPv stability field in D″ and then transforms back to Pv just above the CMB. In this scenerio a double crossing occurs when the phase transition temperature at the CMB is less than the CMB temperature. This is in part because a conductive temperature profile increases monotonically with pressure. However, temperature profiles that sample thermal heterogeneity in D″ (slabs, plumes) can intersect the pPv phase space multiple times even for phase transition temperatures that are greater than the CMB temperature. The CMB is an isothermal boundary so we can always compute the stable phase at the base of the mantle for each model *a priori* (Table 2.2). If pPv is stable at the CMB, at least one phase transition must occur independent of temperature. If Pv is stable, a double crossing is facilitated for mantle regions in the pPv stability field.

2.4 Seismic waveform modeling

We express the relative perturbation to a parameter X using the notation $\delta X = \partial \ln X \equiv \Delta X/X$ where ΔX is the change in X. The perturbation to the P-wave velocity, δvp, and S-wave velocity, δvs, can be expressed as (*Tan and Gurnis*, 2007):

$$\delta vp = \frac{1}{2}\left(\frac{\delta K + 4R_1\delta G/3}{1 + 4R_1/3} - \delta\rho\right) \tag{2.12}$$

$$\delta vs = \frac{1}{2}\left(\delta G - \delta\rho\right) \tag{2.13}$$

Table 2.1: Generic model parameters

Parameter	Symbol	Value	Units	Non-dim Value
Rayleigh number	Ra	-	-	1.437×10^9
Dissipation number	Di	-	-	1.95
Surface temperature	T_S	300	K	0.081
Density	ρ_0	3930	kg m^{-3}	1.0
Thermal expansion coefficient	α_0	3.896×10^{-5}	K^{-1}	1.0
Temperature drop	ΔT	3700	K	1.0
Earth radius	R_0	6371	km	1.0
Gravity	g_0	9.81	m s^{-2}	1.0
Thermal diffusivity	κ_0	10^{-6}	m^2 s^{-1}	1.0
Heat capacity	c_0	1250	J kg^{-1} K^{-1}	1.0
Reference viscosity	η_0	1.0×10^{21}	Pa s	1.0
Cohesion	a	246	kPa	1.0×10^4
Brittle yield stress gradient	b	6.187	MPa km^{-1}	1.6×10^9
Ductile yield stress	σ_y	986	MPa	4.0×10^7
Phase Rayleigh number	Rb	-	-	1.99×10^8
Phase transition temperature	T_Γ	2603	K	0.704
Phase transition width	d	10	km	1.5×10^{-3}

Table 2.2: Model specific parameters. [a] Phase transition pressure (equivalent height above CMB in km). [b] Clapeyron slope (equivalent in MPa K^{-1}). [c] Stable phase at CMB: Perovskite (Pv), post-Perovskite (pPv)

Model	p_Γ[a]	γ[b]	CMB phase[c]
S1	No phase transition		
S2	0.403 (300)	0.114 (7.6)	pPv
S3	0.403 (300)	0.160 (10.6)	Pv
S4	0.379 (450)	0.160 (10.6)	pPv
S5	0.426 (150)	0.160 (10.6)	Pv
S6	0.426 (150)	0.114 (7.6)	Pv
S7	0.438 (75)	0.114 (7.6)	Pv
S8	0.445 (32)	0.200 (13.3)	Pv
S9	0.410 (255)	0.200 (13.3)	Pv

where K is the adiabatic bulk modulus, G shear modulus, ρ density, and $R_1 = G/K$ is equal to 0.45, which is similar to PREM at 2700 km depth. $\delta\rho$ is computed directly from the geodynamic calculations (Appendix A). The perturbations to the elastic moduli are decomposed into phase and thermal parts, assuming they are linearly independent:

$$\delta K(\Gamma, T) = \frac{\partial \ln K}{\partial \Gamma}\Gamma + \frac{\partial \ln K}{\partial T}dT \tag{2.14}$$

$$\delta G(\Gamma, T) = \frac{\partial \ln G}{\partial \Gamma}\Gamma + \frac{\partial \ln G}{\partial T}dT \tag{2.15}$$

where dT is a temperature perturbation relative to a reference adiabat. We derive the reference adiabat semi-empirically by considering the horizontally averaged temperature field for the models with a phase transition (Fig. 2.1). Since a phase transition with a positive Clapeyron slope enhances convection we exclude the model without a phase transition because the adiabatic temperature gradient is less steep and the thermal boundary layers thicker, although the differences are not significant. We construct a reference adiabat with a foot temperature of 0.49 (dimensionally 1700 K) using the dissipation number and thermal expansion profile defined for the geodynamic calculations. These temperatures are contained within the range of time-average geotherms from the models (grey region in Fig. 2.1) between 500 and 2250 km depth. Temperature perturbations are then determined by removing the reference adiabat from the computed temperatures.

We use $\partial \ln K/\partial T = -0.1217$ and $\partial \ln G/\partial T = -0.319$ derived from a theoretical calculation for $MgSiO_3$ (*Oganov et al.*, 2001). However, we apply these values to both

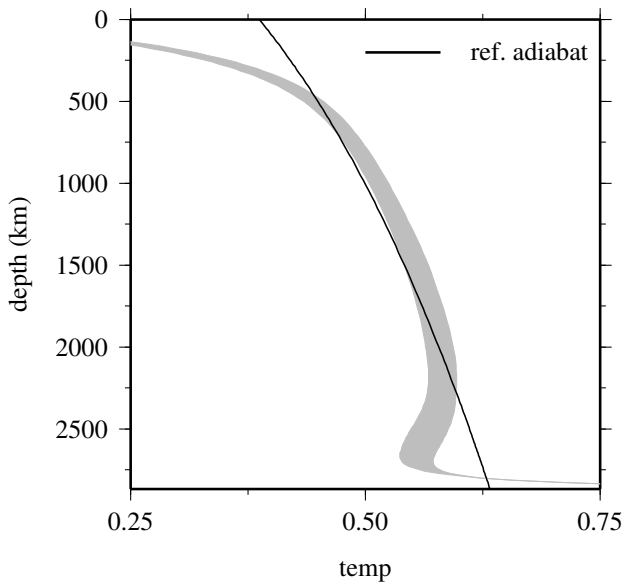

Figure 2.1: Geotherms and reference adiabat. Time-average geotherms (horizontally averaged temperature) of models with a phase transition are contained within the grey region. The reference adiabat is illustrated with a black solid line.

the Pv and pPv phase. Note that these derivatives are non-dimensional because T is a non-dimensional temperature.

Across the Pv-pPv transition, we prescribe fractional changes in both the shear wave and the compressional wave and compute the corresponding derivatives (Appendix A):

$$\frac{\partial \ln G}{\partial \Gamma} = 2\delta vs^{\Gamma} + \frac{Rb}{Ra}\alpha_0 \Delta T \tag{2.16}$$

$$\frac{\partial \ln K}{\partial \Gamma} = \Big(2\delta vp^{\Gamma} + \frac{Rb}{Ra}\alpha_0 \Delta T\Big)(1 + 4R_1/3) - 4R_1/3\frac{\partial \ln G}{\partial \Gamma} \tag{2.17}$$

where δvs^{Γ} and δvp^{Γ} are fractional perturbations to the S- and P-wave velocity, respectively, due to the pPv phase transition. Beneath the Cocos Plate the average S-wave increase is approximately 2% ($\delta vs^{\Gamma} = 0.02$) and the P-wave variation is a few fractions of a percent (*Hutko et al.*, 2008). For simplicity we assign $\delta vp = 0$. The 1-D

seismic model IASP91 (*Kennett and Engdahl*, 1991) converts velocity perturbations to absolute values.

We generate synthetic seismograms using the WKM technique to resolve the SdS triplication originating from high-velocity regions of D″ (*Ni et al.*, 2000). In this initial study we trace rays through seismic models computed from 1-D temperature and phase profiles extracted from the 2-D convection calculations. We select a Gaussian source time function with 4 s duration and bandpass the synthetic data between 4 and 100 s.

2.5 Results

2.5.1 Overview of D″ slab dynamics

We describe typical slab dynamics using model S2 (Fig. 2.2) as all models exhibit similar behavior. The pPv phase boundary is 300 km above the CMB and the Clapeyron slope is 7.6 MPa K^{-1}. Initially, the upper boundary layer thickens and the CMB region warms (Fig. 2.2A). The pPv region has constant thickness except where a few thin stationary plumes emanate from the lower thermal boundary layer and the phase boundary is perturbed to higher pressure. A slab forms from the upper thermal boundary layer when the yield stress is exceeded; sometimes the downwelling is generated by several instabilities that unite to form a dominant downwelling. As the slab descends it warms through adiabatic and viscous heating in addition to diffusion.

Pre-existing plumes at the CMB are displaced laterally by the downwelling, such

as the plume at the tip of the slab (Fig. 2.2B). The cold slab geotherm (Fig. 2.2G, black solid line) intersects the phase boundary (grey dashed line) at lower pressure than ambient mantle, which warps the phase boundary upward producing a thick pPv layer. Latent heat release acts to restore the phase boundary to its unperturbed position and generate a body force that opposes the motion of the slab. However, the amplitude of the thermal anomaly and phase boundary deflection from advected temperature generate the dominant buoyancy forces that are largely unmodified by latent heating.

The slab smothers the CMB, trapping a portion of hot mantle that begins to vigorously convect. During this period the temperature-dependent rheology causes the slab to deform more easily as it warms. The trapped mantle accumulates buoyancy, forming a plume that pushes up the overlying slab (Fig. 2.2C). As the hot upwelling rises from the CMB it enters the Pv stability field which creates strong phase heterogeneity and provides additional positive buoyancy because it is surrounded by pPv. However, latent heat absorption cools the plume and retards the deflection of the phase boundary, although these effects appear negligible. The upwelling erupts through the slab and suppresses the height of the phase boundary (Fig. 2.2D). The upwelling loses its thermal buoyancy through adiabatic cooling and thus its temperature anomaly (relative to the reference adiabat) decreases rapidly as it rises.

Secondary plumes form from patches of thickened boundary layer on either side of the original upwelling (Fig. 2.2D). These also punch through the slab and entrain some of the remaining cooler material to create patches of deformed slab separated by plume

conduits (Fig. 2.2E, but more clearly visible in Fig. 2.2O). A second downwelling at the rightmost edge of the domain displaces these patches and thermal contrasts create topography on top of the pPv layer. As heat diffuses into the slab the thermal anomaly is eradicated and the pPv layer returns to uniform thickness punctuated by a few plumes as in Fig. 2.2A. This process is aperiodic.

2.5.2 Overview of seismic wavespeed anomalies

We compute P- and S-wave velocity anomalies using the geodynamic data (Fig. 2.2) assuming that the P-wave is unperturbed by the phase boundary (δvp^{Γ}=0%) and the S-wave experiences a step-wise increase in velocity (δvs^{Γ}=2%) (Fig. 2.3). P and S phases with similar paths in the lower mantle will therefore generate different waveform complexity. Furthermore, seismic profiles depend on the evolutionary stage of the slab and its interaction with the thermal boundary layer and pPv phase transition (Fig. 2.3).

At 0 Myr, the seismic profiles are largely unperturbed except for the pPv phase boundary (Fig. 2.3P) and reduced basal velocity caused by the lower thermal boundary layer. The slab introduces thermal heterogeneity that produces a strong seismic gradient across its top surface (Fig. 2.3Q). This thickens the pPv layer and generates a much steeper velocity gradient for the S-wave than just the pPv transition alone (Fig. 2.3Q). In this region the wavespeed reduction above the CMB is also larger than it would be without an overlying slab.

The growth of a plume beneath the slab produces four distinctive seismic velocity

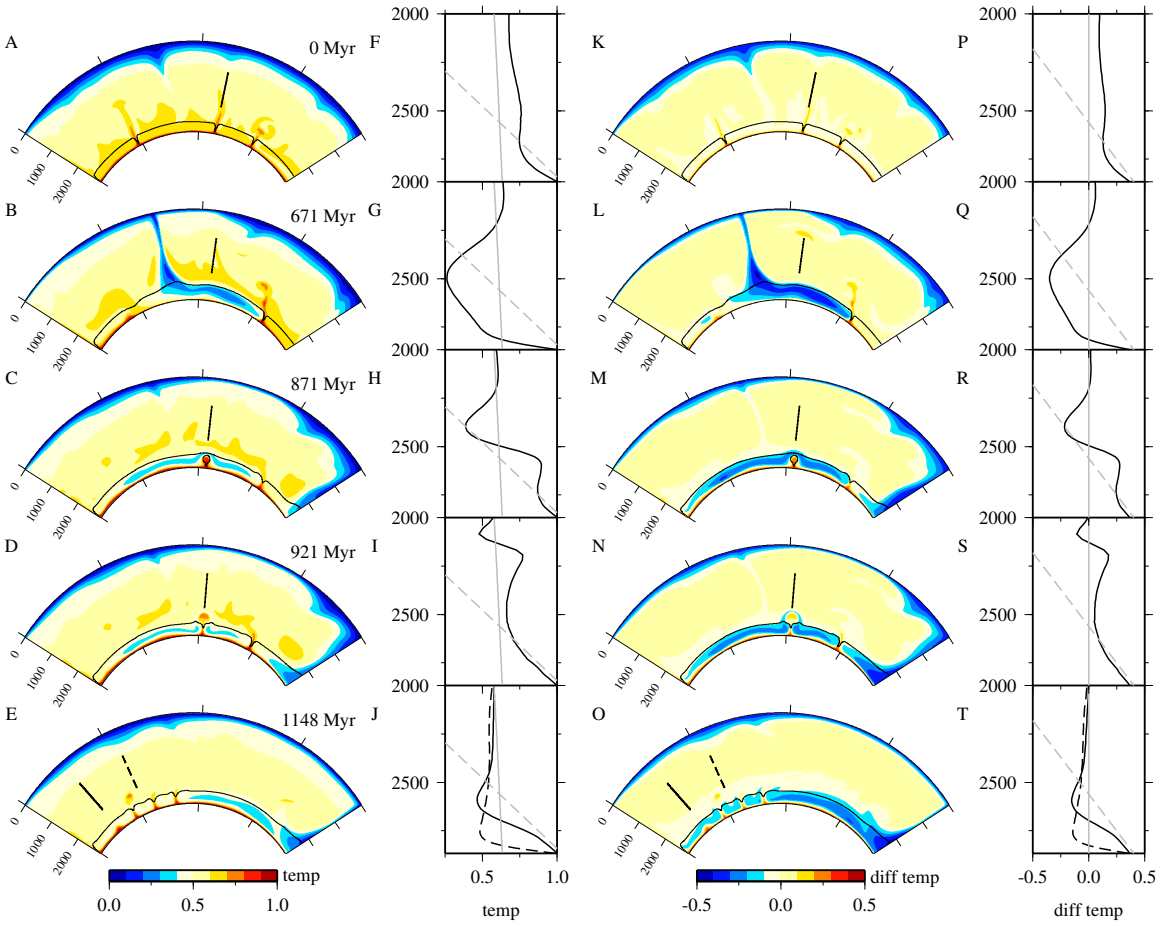

Figure 2.2: Representative evolution of a slab in D″ (model S2). Each row represents a different time slice and given times are relative to the top row. (A–E) Temperature, (K–O) differential temperature (reference adiabat removed). The pPv layer at the CMB is contoured in black. Black solid and dashed lines represent profile locations. (F–J) Temperature profiles for A–E at the profile locations, (P–T) differential temperature profiles for K–O. The grey solid line denotes the reference adiabat (zero differential temperature for K–O) and the grey dashed line shows the Pv-pPv phase boundary.

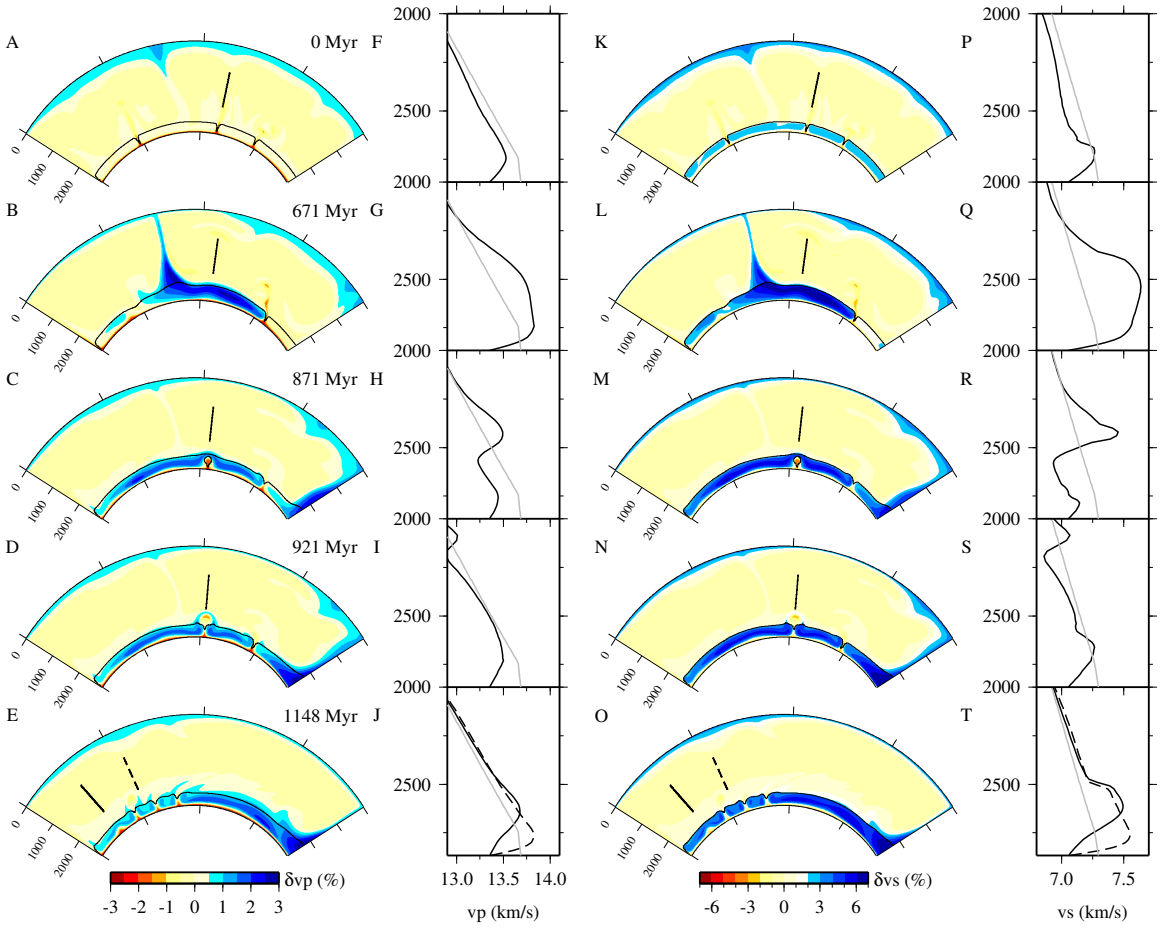

Figure 2.3: P- and S-wave velocity to compare with Fig. 2.2 (model S2, δvp^{Γ}=0%, δvs^{Γ}=2%). (A–E) P-wave, (K–O) S-wave velocity anomaly. (F–J) P-wave velocity profiles for A–E, (P–T) S-wave velocity profiles for K–O. The grey line denotes the 1-D seismic model IASP91.

gradients (Figs. 2.3H,R). Across the top of the slab the gradient is positive and steep, but wavespeeds rapidly decline in the plume due to temperature and phase (S-wave only). Wavespeeds are consistently low in the plume with a gradient comparable to the 1-D model. The thermal boundary layer at the base of the mantle generates a second negative velocity gradient, although the actual decrease in velocity is significantly less than the transition from slab to plume.

When the plume punches through the slab the rising hot material suppresses wavespeeds and generates seismic profiles similar to those at 0 Myr (compare Figs. 2.3I,S with Figs. 2.3F,P). The plume head is surrounded by cooler remnant slab which introduces a negative wavespeed gradient at 2100 km depth. Secondary plumes develop in the lower thermal boundary layer and break apart the remnant slab. Velocity profiles through a developing plume in the pPv stability field (Figs. 2.3J,T, black solid line) exhibit a low negative gradient at the CMB. This contrasts to a Pv plume otherwise within a pPv layer which produces a positive velocity gradient except for the very base of the mantle (compare Figs. 2.3J,T with Figs. 2.3H,R, black solid line). The neighboring blocks of cool deformed slab produce a sharp phase boundary with relatively high wavespeeds (Figs. 2.3J,T, black dashed line). The lower thermal boundary is suppressed beneath the slab, which generates a high negative velocity gradient at the base.

2.5.3 Dynamic and seismic variations

Our models explore variations in the phase boundary height and Clapeyron slope. Increasing the pPv transition pressure at fixed temperature is equivalent to reducing the pPv transition temperature at a fixed pressure because the pPv stability field is simply translated in P–T space.

The leftmost columns of Figs. 2.4 and 2.5 show models with an increased Clapeyron slope of 10.6 MPa K^{-1}. Models S3, S4, and S5 have equivalent transition pressures of 300 km, 450 km, and 150 km above the CMB, respectively. We show the S-wave velocity but the perturbations to the P-wave are comparable except for the step-wise increase due to the pPv phase transition. Model S3 (Figs. 2.4A,E,B,F) has a transition pressure of 300 km above the CMB which is the same as the "typical" model in Section 2.5.1. However, the Clapeyron slope is larger so the stable phase at the CMB is now Pv rather than pPv and plumes form at the CMB in the Pv stability field (Figs. 2.4A,E, black solid line). This accentuates the wavespeed contrast with the overlying cooler pPv by producing a lower velocity basal layer (compare Figs. 2.3O,T with Figs. 2.5A,E, black solid line). Figs. 2.4A,E reveal lower boundary layer instabilities at various stages of their life cycle. This includes thickening of the boundary layer, plume detachment from the CMB, and eruption through the pPv layer with a trailing conduit. Plume heads become Pv within the pPv layer. Seismic waves may therefore sample all of this complexity within small ranges of azimuth or epicentral distance. At later time, several plumes punch through the slab and generate separate blocks of pPv that are surrounded at the base and edges by hot Pv (Figs. 2.4B,F).

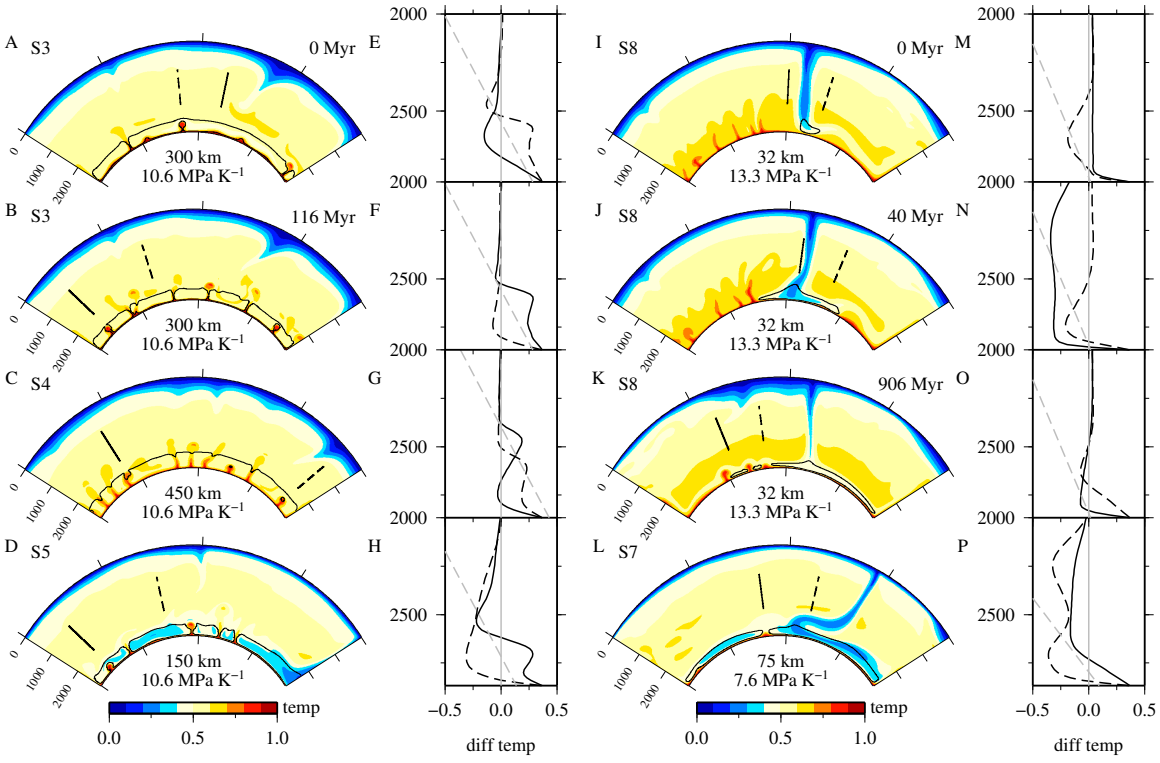

Figure 2.4: D″ dynamic outcomes from parameter variation. (A–D) and (I–L) Temperature. The pPv layer at the CMB is contoured in black and the phase transition parameters (height above the CMB and Clapeyron slope) are given below each panel. Black solid and dashed lines represent profile locations. (E–H) and (M–P) correspond to differential temperature profiles at the profile locations for A–D and I–L, respectively. The grey solid line denotes the reference adiabat (defined zero) and the grey dashed line shows the Pv-pPv phase boundary. Given times are relative to 0 Myr for that particular model.

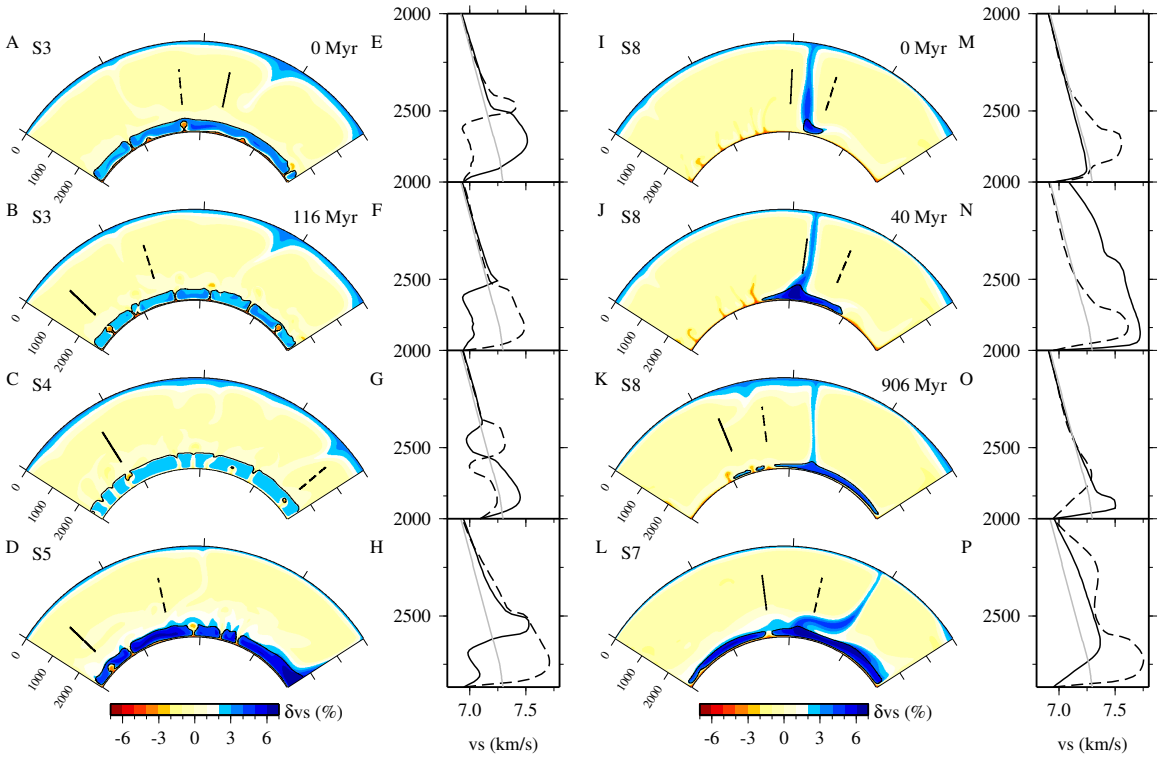

Figure 2.5: S-wave velocity to compare with Fig. 2.4 (δvp^{Γ}=0%, δvs^{Γ}=2%). (A–D) and (I–L) S-wave velocity perturbation. (E–H) and (M–P) corresponding S-wave velocity at the profile locations for A–D and I–L, respectively. The grey solid line denotes the 1-D seismic model IASP91.

Model S4 has a lower transition pressure than S3 (450 km versus 300 km) which is equivalent to translating the phase boundary to higher temperature (Figs. 2.4C,G) such that the stable phase at the CMB is pPv. Plumes form in the pPv stability field and intersect the Pv-pPv phase boundary as they rise through D″. This forms isolated pockets of hot Pv within the pPv-dominated layer (Fig. 2.4G, black dashed line) which causes multiple perturbations to the S-wave velocity (Fig. 2.5G, black dashed line). The thermal profile crosses the phase boundary multiple times and is an example of a "triple crossing" (Fig. 2.4G, black dashed line). Escaping plume heads also create concave-up notches in the phase boundary at the top of D″ (Figs. 2.4C,G, black solid line). This is also observed in S2 (Figs. 2.2O,T) but is more noticeable here because the Clapeyron slope is larger. The pPv layer has a smooth upper surface at longer wavelength, which contrasts with models that produce distinct pPv blocks. However, the layer is permeated by plumes that produce low-velocity regions extending radially from the CMB.

Model S5 has a higher transition pressure than S3 (150 km versus 300 km above the CMB) but behavior is comparable because both models facilitate a double crossing for the average 1-D geotherm. However, perturbations to the phase boundary height are more comparable to the ambient thickness of the pPv layer (Fig. 2.4D). Blocks of pPv are more separate and there is relatively larger topography on their tops.

A larger Clapeyron slope (13.3 MPa K^{-1}) enables greater lateral phase heterogeneity (Figs. 2.4I,J,K). In model S8, pPv only forms within cold slabs in D″ because the average 1-D geotherm is too warm to sustain a permanent pPv layer (Fig. 2.4I,M,

black solid line). For example, pPv occurs around the tip of a slab as it penetrates D″ (Fig. 2.4I) causing substantial variations in phase boundary height (Figs. 2.4M,N). Plumes can penetrate through older slabs whilst downwelling material continues to accumulate nearby, which forms both regions of pPv blocks and a continuous layer (Fig. 2.4K).

Finally, a folded slab at the CMB has considerable complexity. Two negative temperature perturbations are generated by the uppermost and lowermost parts of the slab fold with ambient material sandwiched between (Fig. 2.4L). The top of the lowermost thermal anomaly accompanies the transition to pPv. These features are clearly evident in the seismic profile (Fig. 2.5P, black dashed line). Seismic velocity gradients are steeper in the cold regions, with the second perturbation accentuated by the phase transition. The negative velocity gradient at the base of the mantle is large because of the overlying slab and Pv is the stable phase at the CMB.

2.5.4 Waveform predictions

Thermal and phase heterogeneity produce wavespeed perturbations that can be explored through waveform modeling. We produce 1-D synthetic seismograms for the S-wave velocity profiles in Figs. 2.3 and 2.5. First we overview basic features that are necessary to interpret the synthetic data.

The seismograms are aligned on the IASP91-predicted S arrival and the triplicated SdS phase arrives before ScS. IASP91 (grey seismograms) does not produce a SdS arrival as it lacks a velocity discontinuity just above the CMB. The height of the

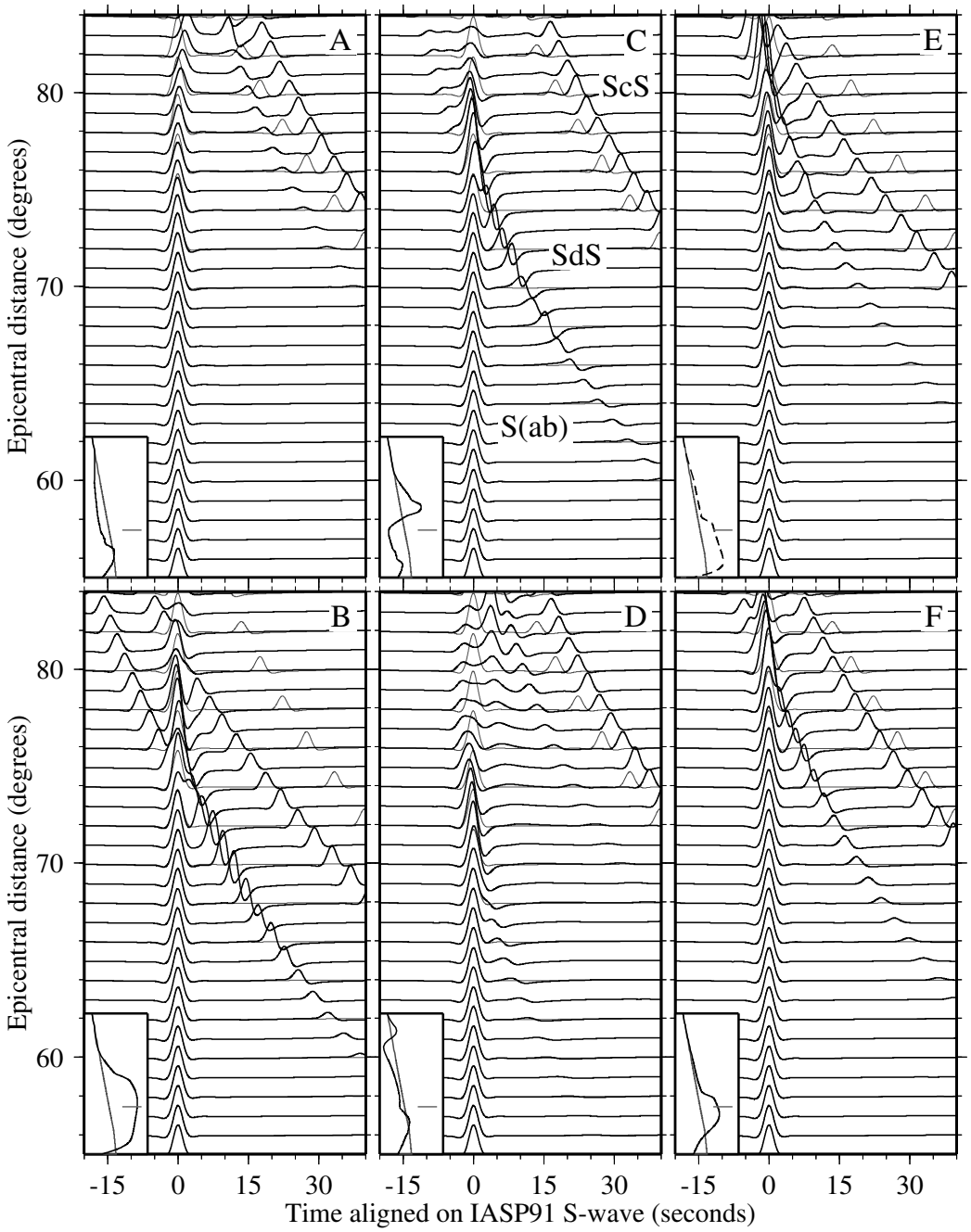

Figure 2.6: Synthetic seismograms (S-wave) for the reference model to compare with Fig. 2.3. (A–F) Seismograms for the profiles in Figs. 2.3P–T, respectively, are in black and IASP91 are in grey. The S-wave structure is shown inset (same as Figs. 2.3P–T, axes from 6.8 to 7.8 km/s and 2000 to 2890 km depth, grey line denotes IASP91, dark grey horizontal line denotes 300 km above the CMB).

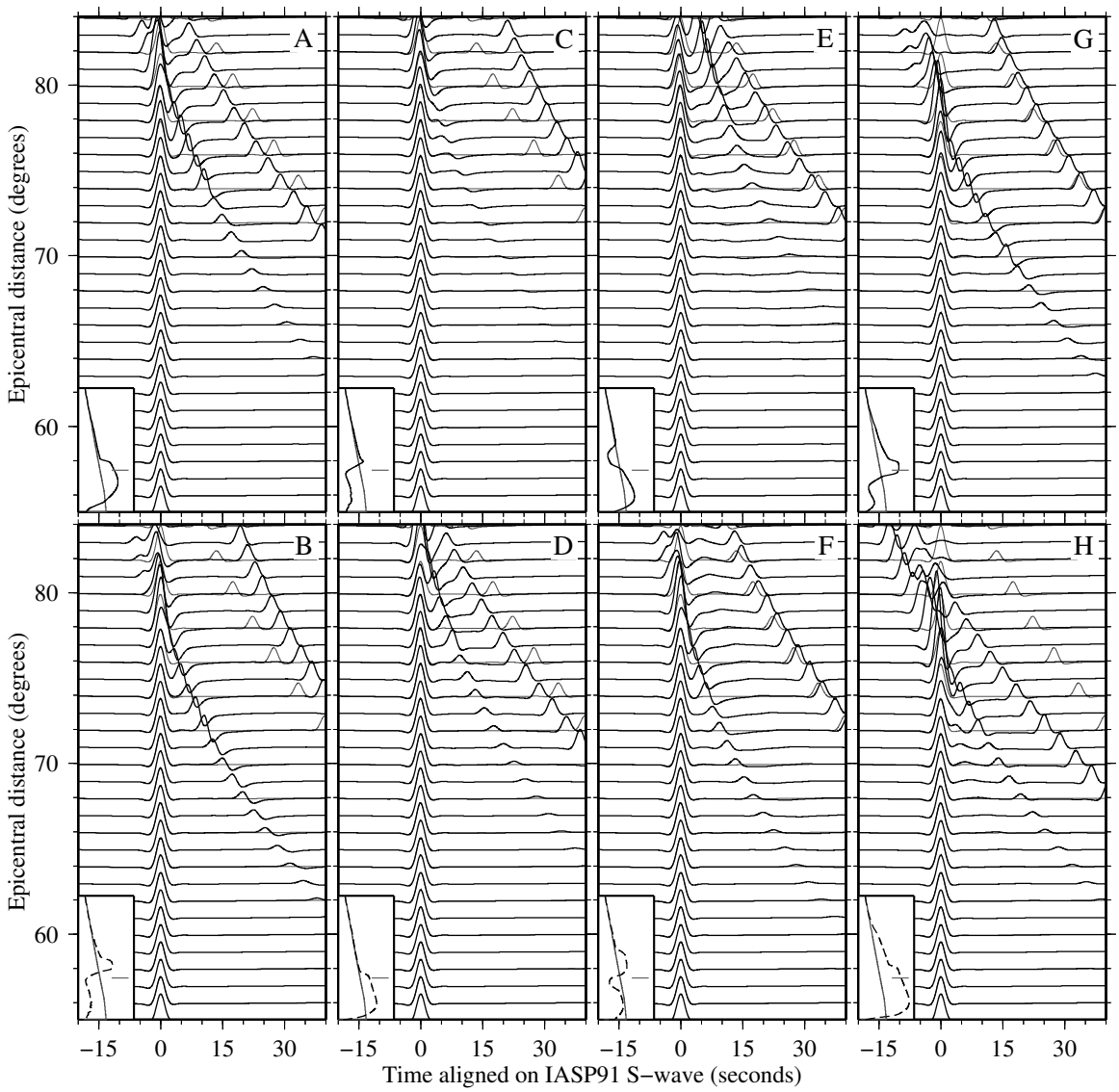

Figure 2.7: Synthetic seismograms (S-wave) for dynamic variations to compare with Fig. 2.5. (A–B) Seismograms for the black solid and dashed profiles from Fig. 2.5E, respectively. Similarly for (C–D) Fig. 2.5F, (E–F) Fig. 2.5G, (G–H) Fig. 2.5H. See Fig. 2.6 caption.

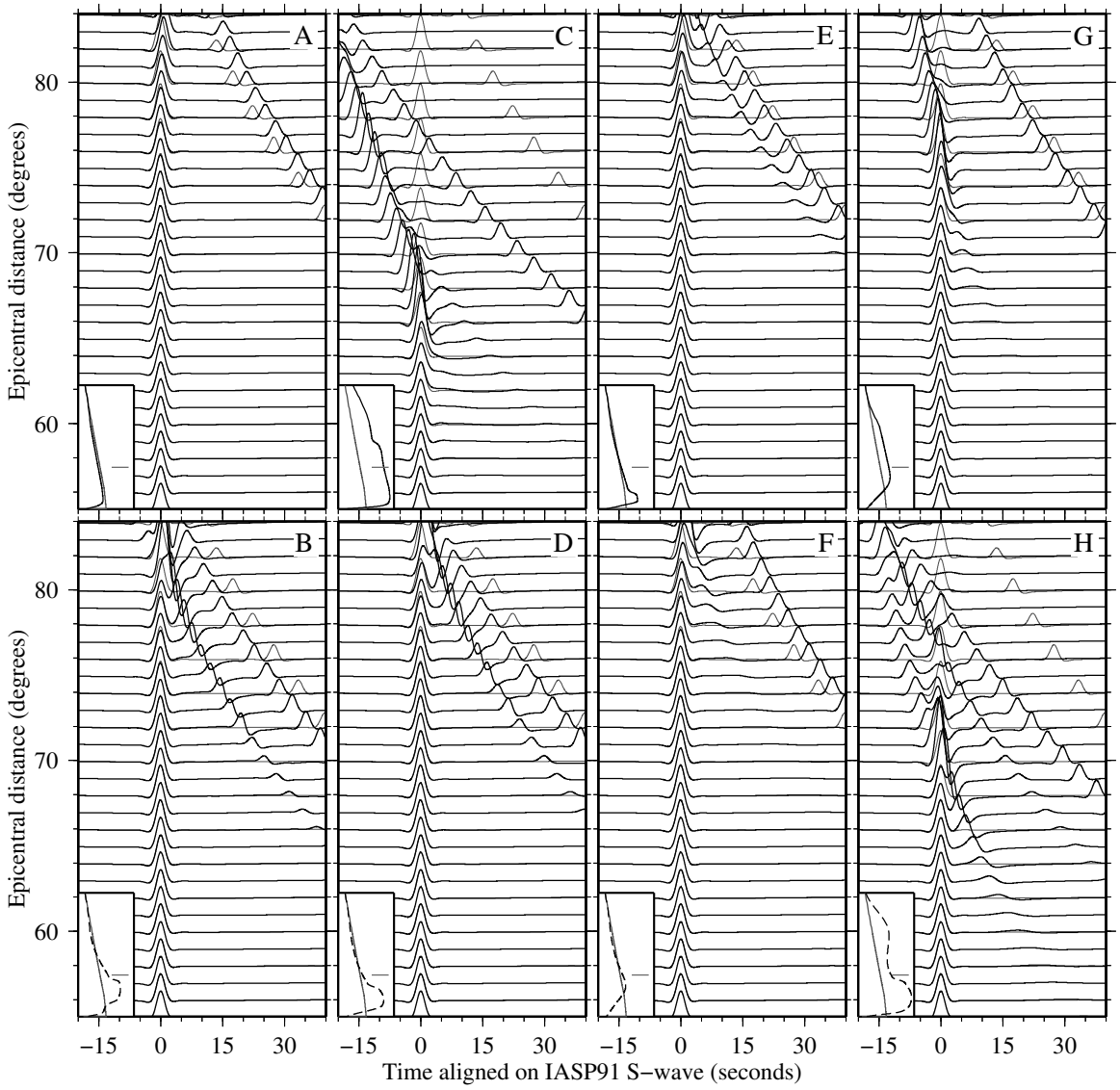

Figure 2.8: Synthetic seismograms (S-wave) for dynamic variations to compare with Fig. 2.5. (A–B) Seismograms for the black solid and dashed profiles from Fig. 2.5M, respectively. Similarly for (C–D) Fig. 2.5N, (E–F) Fig. 2.5O, (G–H) Fig. 2.5P. See Fig. 2.6 caption.

interface can be determined by SdS-S and ScS–SdS differential travel times. For a given epicentral distance, SdS–S increases and ScS–SdS decreases as the phase boundary is perturbed to high pressure. The relative amplitude response of SdS depends on the magnitude of the velocity increase across the discontinuity and ScS–S constrains the volumetric velocity anomaly within D″ (below the interface). SdS overtakes S as the first arrival at post-crossover distances, which is $\sim$ 85 degrees for the 1-D seismic model SLHO for a focal depth of 600 km (*Lay and Helmberger*, 1983). A negative seismic velocity gradient above the CMB slows SdS which pushes the post-crossover SdS and S arrivals together. Furthermore, more energy turns below the discontinuity, which weakens the post-crossover S phase (*Young and Lay*, 1987).

A recently subducted slab produces a large velocity increase at the phase boundary because of the coincident strong thermal gradient and phase jump (Fig. 2.3L) which generates large SdS amplitude (Fig. 2.6B). Conversely, for a slab that has warmed at the CMB the thermally induced velocity jump at the D″ discontinuity is less and the SdS amplitude is reduced (Fig. 2.6E). Relative to a thinner D″ region, a slab with a broad thermal anomaly elevates the phase boundary, which causes SdS to appear at shorter distances, decreases SdS–S, and reduces the SdS–S crossover distance (compare Fig. 2.6B with Fig. 2.6E). Thick D″ regions with cold slabs have a large positive volumetric wavespeed anomaly which causes ScS to arrive early (ScS–S decreases) and therefore reduces the ScS–S crossover distance (Fig. 2.6B). As D″ becomes increasingly thin, ScS arrives closer to the IASP91 prediction, SdS–S increases, and ScS–SdS decreases until SdS arrives as a precusory shoulder to ScS (Figs. 2.8D,E).

Post-crossover SdS amplitude is large for fast regions that extend from the phase boundary to the CMB (e.g., Fig. 2.6B).

A thickening boundary layer at the base of a slab has a negative wavespeed anomaly which increases the arrival time of ScS (ScS–S increases) by reducing the volumetric wavespeed anomaly (Fig. 2.6F). As a plume develops, the wavespeeds beneath the D″ discontinuity continue to decrease and ScS arrives with the IASP91 prediction (Fig. 2.7G) or is delayed (Fig. 2.6C and Fig. 2.7B). These results are consistent with the volumetric velocity anomaly controlling ScS–S travel times (e.g., *Sidorin et al.*, 1999a). The temperature anomaly at the phase interface decreases as the plume heats the overlying slab, which reduces SdS amplitude by decreasing the velocity jump (Fig. 2.7C). However, SdS–S does not vary because this is sensitive to the height of the discontinuity above the CMB, which is unaffected by plume growth within D″ until the plume erupts through the phase boundary. A warm plume bends rays away from the normal which reduces S and SdS amplitude beyond the SdS–S crossover relative to a horizontal slab (compare Fig. 2.7G and Fig. 2.7H beyond ~ 80 degrees).

Fig. 2.7F shows the seismogram for a Pv plume head within a pPv layer (Fig. 2.4C, black dashed line). SdS arrives from the top of the pPv layer but a second triplicated arrival from the warm plume to pPv transition at higher pressure is absent. The slow velocity within the plume presumably creates a shadow zone that suppresses this second arrival. The waveforms for this profile are similar to those produced by a simple phase transition overlying a thermal boundary layer (Fig. 2.7A). Although

the velocity structure differs from IASP91, the arrival time of S and ScS is similar.

The seismogram for a plume erupting through a pPv layer has an additional (weak) triplication phase that arrives after S for distances 60–68 degrees (Fig. 2.6D). This phase originates from cooler slab material carried above the plume head. Beyond 75 degrees the direct S arrival enters a shadow zone due to ray bending from sampling the slower velocity plume. Since the wavespeed anomalies are generally negative throughout D″, the SdS–S and ScS–S crossover distances are > 84 degrees. Two triplicated arrivals are also produced by a folded slab interacting with the phase transition (Figs. 2.4L,2.5L). The first arrives between 62–70 degrees and originates from the top of the uppermost slab fold (Fig. 2.8H). The second arrives beyond 65 degrees and is SdS from the velocity increase caused by the slab interacting with the phase boundary. Combined analysis of multiple triplicated arrivals, possibly with other phases, may be able to determine the characteristic lengthscale of slab folding above the CMB.

A simple thermal boundary layer at the CMB delays ScS, and marginally delays the arrival time for S at large distances (> 80 degrees) (Figs. 2.8A,F). A warm conduit emanating from the CMB delays S beginning at shorter distances (> 76 degrees) and further suppresses the amplitude of the arrival (Fig. 2.6A). Additionally, a weak SdS phase is faintly visible beyond about 72 degrees and is generated by the small velocity increase at the phase transition (Fig. 2.6A). ScS–SdS is small because the discontinuity is close to the CMB.

2.6 Discussion

Slabs rapidly advect and blanket the CMB from episodic flushing of the upper thermal boundary layer. The maximum thermal anomaly of slabs at the CMB is 0.33 (1200 K), which is at the upper bound of estimates (*Steinbach and Yuen*, 1994). Additionally, the simple two-phase model (Pv and pPv) and uncertainties in material properties preclude an accurate mapping of temperature and phase to seismic wavespeed. However, we focus on changes in seismic velocity gradient because the absolute magnitude of velocity perturbation is not critical for analyzing trends in seismic triplication data. Similarly, choosing an alternative reference geotherm would not significantly affect our results. The largest discrepancy between the horizontally averaged temperature and reference adiabat is in the region of subadiabatic temperature gradients above the CMB. If we choose a horizontally averaged temperature as reference (extrapolating across the boundary layers) the wavespeed anomaly for slabs (plumes) will slightly decrease (increase) in amplitude. Finally, diffuse thermal anomalies at the CMB would not produce sharp seismic gradients and lateral variation in the phase boundary necessary to investigate high-frequency waveform complexity.

Downwellings displace pre-existing plumes at the CMB because low-viscosity conduits are established between subduction cycles. Therefore plumes infrequently develop at slab tips in comparison to models with an unperturbed lower thermal boundary layer (*Sidorin et al.*, 1998; *Tan et al.*, 2002). Episodic subduction promotes plume development beneath slabs because existing basal instabilities are swept aside. Slabs

insulate the CMB allowing the boundary layer to thicken and form upwellings. *Tan et al.* (2002) investigate these dynamics and propose two types of outcomes: "normal plumes" and "mega-plumes". Qualitatively the plumes that we observe are more akin to "normal plumes" because they are not voluminous eruptions and dissipate quickly above the CMB. We anticipate different behavior because our models are compressible with a phase transition, whereas the fine-scale models of *Tan et al.* (2002) are Boussinesq. Convective vigor and adiabatic cooling control the temperature anomaly of plumes in compressible flow models (*Zhao and Yuen*, 1987). After plumes dissipate the thermal anomaly of the slab they combine into a few single upwellings (*Vincent and Yuen*, 1988).

Nevertheless, the seismic profile for a mega-plume beneath an ancient slab (Fig. 11, right panel in *Tan et al.*, 2002) is comparable to a plume within a pPv layer (e.g., Fig. 2.3M,R). The later includes an S-wave velocity increase across the Pv-pPv phase boundary. Uncertainties when mapping temperature and phase to seismic wavespeed prevent 1-D seismic analyses from identifying a warm plume (seismically slow) versus a hot mega-plume (slower). Furthermore, we extract 1-D temperature and phase profiles from 2-D convection calculations and are therefore insensitive to the total volume of the plume. The profiles above the CMB are different because *Tan et al.* (2002) compute δvs using the horizontally averaged temperature field as a reference geotherm, whereas we use an adiabat. Our models therefore include a negative seismic velocity gradient just above the CMB in accordance with seismic data (*Cleary*, 1974).

The models suggest several mechanisms that may explain the origin of some seis-

mic scatterers. First are small-scale plumes at different stages of development forming in a pPv layer (Fig. 2.4A). The phase difference between a Pv plume and the surrounding pPv layer will further increase wavespeed variations in comparison to just the temperature effect. Second are steep-sided isolated blocks of pPv (Fig. 2.4B). Third are concave-up notches in the phase boundary caused by escaping plume heads (Fig. 2.4C). Furthermore, these processes often operate in combination.

The synthetic seismograms reveal triplicated arrivals originating from the D″ discontinuity and large thermal gradients, e.g., a folded slab (Fig. 2.8H). The timing and amplitude response of the arrivals provide insight into the velocity increase, height of the phase transition above the CMB, and approximate thickness of the fast region. However, S, SdS and ScS in the distance range 60–83 degrees are largely insensitive to small-scale features beneath the phase boundary. Negative seismic gradients are inherently difficult to resolve because energy is not refracted to the surface, which means that low-amplitude reflected arrivals, often below the noise level, have to be analyzed (e.g., *Flores and Lay*, 2005). The ScS–S differential travel time constrains the volumetric wavespeed anomaly of D″ but is not sensitive to the distribution of heterogeneity.

2.7 Conclusions

The models reveal complex interaction of slabs, plumes, and the Pv-pPv transition which produces significant thermal and phase heterogeneity in D″ over small distances. Slabs deflect the phase boundary and disturb the lower thermal boundary layer,

pushing aside pre-existing upwellings. Plumes regularly develop beneath slabs and distort the phase boundary and slab morphology as they erupt from the CMB. Plume formation occurs less frequently at slab edges because a few stationary upwellings drain the boundary layer between cycles of subduction. Advected isotherms produce more complicated thermal structure than conductive profiles. This enables multiple crossings of the phase boundary, e.g., a Pv plume head within a pPv layer can produce a "triple crossing".

The topology of the pPv layer depends on the transition pressure (or equivalently transition temperature since both translate the phase boundary in P–T space) and the Clapeyron slope. The models reveal a variety of behavior including: (1) distinct pPv blocks separated by upwellings, (2) notches at the top of a pPv layer caused by plume heads, (3) regions of Pv embedded within a pPv layer due to upwellings. Furthermore, these scenerios have interesting consequences for seismic scattering phenomena which will be explored in a future study.

In synthetic seismograms, we cannot resolve small-scale complexity beneath the D″ discontinuity using solely S, SdS, and ScS triplication data to 84 degrees. This is because of inherent limitations in resolving negative seismic velocity gradients. In future work we will model the seismic wavefield using a finite difference approach to explore SH-, SV-, and P-waves for many D″ arrivals (e.g., S, Scd, ScS, SKS, SKKS) and potentially reverberations in the pPv layer. Extending the distance range to 110 degrees will also allow us to analyze diffracted phases (e.g., Sd) and arrivals beyond the SdS–S crossover distance. 2-D models can explore the focusing and defocusing

of seismic rays due to topography on the phase boundary, and the effects of seismic anisotropy also need evaluating.

There are possibilities for developing more complex dynamic models. Compositionally stratified slabs, possibly interacting with a chemical layer at the CMB, will also generate waveform complexity (*Tackley*, 2011). Furthermore, chemical heterogeneity in D″ influences seismic velocities and the Pv-pPv transition pressure and depth of the mixed phase region. Thermal conductivity strongly controls heat transport at the CMB and therefore the thermal evolution of slabs.

Chapter 3

A geodynamic and mineral physics model of a solid-state ultralow-velocity zone

Originally published in:

Bower, D. J., J. K. Wicks, M. Gurnis, and J. M. Jackson (2011), A geodynamic and mineral physics model of a solid-state ultralow-velocity zone, *Earth Planet. Sc. Lett.*, *303*, 193–202, doi:10.1016/j.epsl.2010.12.035.

3.1 Abstract

Recent results (*Wicks et al.*, 2010) suggest that a mixture of iron-enriched (Mg,Fe)O and ambient mantle is consistent with wavespeed reductions and density increases inferred for ultralow-velocity zones (ULVZs). We explore this hypothesis by simulating convection to deduce the stability and morphology of such chemically distinct structures. The buoyancy number, or chemical density anomaly, largely dictates ULVZ shape, and the prescribed initial thickness (proxy for volume) of the chemically distinct layer controls its size. We synthesize our dynamic results with a Voigt-Reuss-Hill mixing model to provide insight into the inherent seismic trade-off between ULVZ thickness and wavespeed reduction. Seismic data are compatible with a solid-state

origin for ULVZs, and a suite of these structures may scatter seismic energy to produce broadband PKP precursors.

3.2 Introduction

The large chemical, density, and dynamical contrasts associated with the juxtaposition of liquid iron-dominant alloy and solid silicates at the core-mantle boundary (CMB) are associated with a rich range of complex seismological features. Seismic heterogeneity at this boundary includes small patches of anomalously low sound velocities, called ultralow-velocity zones (ULVZs). Their small size (5 to 40 km thick) (e.g., *Garnero and Helmberger*, 1996) and depth ($>$ 2800 km) present unique challenges for seismic characterization.

ULVZs were first noted with teleseismic SPdKS phase diffracting along the CMB to determine the P-wave velocity at the base of the mantle beneath the central Pacific (e.g., *Garnero et al.*, 1993b; *Garnero and Helmberger*, 1995, 1996; *Helmberger et al.*, 1996). The compressional wavespeed decreases by 5 to 10% over a depth of 5 to 40 km above the CMB, consistent with PcP precursors (e.g., *Mori and Helmberger*, 1995; *Revenaugh and Meyer*, 1997; *Hutko et al.*, 2009). In other locations, ULVZs are seismically absent or below the detection threshold, such as the North Pacific (*Rost et al.*, 2010a), which may imply they are not globally ubiquitous (see *Thorne and Garnero*, 2004). ULVZs have been correlated with the location of hotspots (*Williams et al.*, 1998) and tentatively to the edges of large low-shear velocity provinces (e.g., *Lay et al.*, 2006). Recent thermochemical convection calculations lend support to

these spatial correlations (*McNamara et al.*, 2010).

Precursors and postcursors to the converted core-reflected phase ScP can potentially constrain the P and S wavespeed, thickness, and density of ULVZs (e.g., *Garnero and Vidale*, 1999; *Reasoner and Revenaugh*, 2000). Based on this approach, analyses using small-aperature and short-period arrays have elucidated the structure between Tonga–Fiji and Australia at high resolution (*Rost and Revenaugh*, 2003; *Rost et al.*, 2005, 2006; *Idehara et al.*, 2007; *Rost et al.*, 2010b). These studies report P and S wavespeed reductions of $\approx 8\%$ and $\approx 24\%$, respectively, a thickness of about 10 km, and a density increase of around 10%.

All of these studies characterize structure with a 1-D model. Although quasi-1D models utilize different structures for the source and receiver paths (e.g., *Garnero and Helmberger*, 1996; *Helmberger et al.*, 1996), only a few 2-D models have been reported. Probing the CMB beneath the southwest Pacific, *Wen and Helmberger* (1998a) model SKS-SPdKS observations with Gaussian-shaped ULVZs of approximately 40 km in height, 250 to 400 km lateral extent, and a P-wavespeed drop of about 10%. PKP precursors suggest that these larger structures are composed of smaller undulations (*Wen and Helmberger*, 1998b). A concave-down upper interface is necessary to model structures beneath Africa and the eastern Atlantic (*Helmberger et al.*, 2000). In both 1-D and 2-D models there are trade-offs between the height and velocity decrease of ULVZs (e.g., *Garnero and Helmberger*, 1998; *Wen and Helmberger*, 1998a).

A partial-melt origin for the ULVZs predicts a P-to-S wavespeed reduction of about 1:3 (*Williams and Garnero*, 1996; *Berryman*, 2000; *Hier-Majumder*, 2008). In

this model, the velocities of the average assemblage are decreased by melt formed either by fluid reaction products of Fe liquid with silicate mantle or by partial melting of Fe-rich mantle. The hypothesis is consistent with the correlation between ULVZs and hot spots (*Williams et al.*, 1998) and the broad agreement with P-to-S velocity reductions determined from core-reflected phases. Early dynamical calculations question the ability to produce a dense and non-percolating melt phase in the deep Earth (*Hernlund and Tackley*, 2007). However, the stirring of ULVZs by the larger-scale convective motions of the mantle can potentially maintain a partially molten region (*Hernlund and Jellinek*, 2010). Partial melt may also be trapped within ULVZs because of textural changes (e.g., *Rost et al.*, 2005, 2006), but theoretical and experimental justifications are incomplete, particularly at the temperatures and pressures of the CMB region.

Iron enrichment of solid phases, specifically the increase in Fe/(Fe+Mg) ratio, can simultaneously increase density and reduce compressional and shear velocity (e.g., *Karato and Karki*, 2001). This partly inspired the notion of solid, iron-rich ULVZs, such as a metal-bearing layer (*Knittle and Jeanloz*, 1991; *Manga and Jeanloz*, 1996), subducted banded iron formations (*Dobson and Brodholt*, 2005), or iron-enriched post-perovskite (*Mao et al.*, 2006; *Stackhouse and Brodholt*, 2008). Iron-rich systems are typically denser than the surrounding mantle, which is required to explain the locations of ULVZs at the base of the mantle.

Recent results show that the sound velocities of a solid iron-enriched (Mg,Fe)O at CMB pressures are low enough, such that only a volumetrically small amount ($\sim$ 10–

20%) mixed with coexisting silicates are needed to explain ULVZs (*Wicks et al.*, 2010). We are motivated to generate a numerical convection model of a thin, iron-enriched (Mg,Fe)O-containing layer interacting with the lowermost thermal boundary layer. Mantle convection thickens (thins) a dense layer beneath upwellings (downwellings) and controls its spatial distribution (*Davies and Gurnis*, 1986). A persistent stable layer has a density contrast of a few percent (e.g., *Garnero and McNamara*, 2008) and may convect internally (*Hansen and Yuen*, 1988). We explore whether these characteristics are manifested in this iron-enriched (Mg,Fe)O-containing layer. We determine the steady-state morphology of such a layer and develop an integrated and self-consistent ULVZ model which uses constraints from geodynamics and mineral physics and is consistent with seismic data.

3.3 Numerical models

3.3.1 Equations and solution methods

We apply the Boussinesq approximation to model thermochemical convection using CitcomS (*Zhong et al.*, 2000; *Tan et al.*, 2007) because the pressure range of our domain is small and energy dissipation is negligible with a greatly reduced thermal expansion coefficient at high pressure. The equation for the conservation of mass for an incompressible fluid is:

$$\nabla \cdot \mathbf{u} = 0 \tag{3.1}$$

where $\mathbf{u}$ is velocity. The non-dimensional momentum equation is:

$$-\nabla P + \nabla \cdot (\eta \underline{\dot{\epsilon}}) = (RbC - RaT)\hat{\mathbf{r}} \tag{3.2}$$

where P is the dynamic pressure, η is the viscosity, $\underline{\dot{\epsilon}}$ is the deviatoric strain rate, Ra is the thermal Rayleigh number, T is temperature (non-dimensionally ranging from 0 to 1), Rb is the chemical Rayleigh number, and $\hat{\mathbf{r}}$ is the radial unit vector. Composition, C, ranging from 0 to 1, encompasses two chemical components. The first component ($C = 0$) is ambient mantle, the second ($C = 1$) is a two-phase mix containing iron-enriched (Mg,Fe)O that constitutes the distinct chemistry of the ULVZ. We equivalently refer to the latter component as the chemical, or (Mg,Fe)O-containing, component.

The Rayleigh numbers are defined as:

$$Ra = \frac{\rho \alpha \Delta T D^3 g}{\eta_0 \kappa} \tag{3.3}$$

$$Rb = \frac{\Delta \rho_{ch} D^3 g}{\eta_0 \kappa} \tag{3.4}$$

where the parameters and their values are provided in Table 3.1. A useful non-dimensional parameter is the buoyancy number, B, which describes the chemical density anomaly normalized by the maximum thermal density anomaly, or equivalently the ratio of chemical-to-thermal buoyancy:

$$B = \frac{Rb}{Ra} = \frac{\Delta \rho_{ch}}{\rho \alpha \Delta T}. \tag{3.5}$$

Table 3.1: Model parameters

Parameter	Symbol	Value	Units
Density	ρ	5500	kg m^{-3}
Thermal expansion coefficient	α	10^{-5}	K^{-1}
Temperature drop	ΔT	1500	K
Mantle depth	D	2890	km
Gravity	g	10.3	m s^{-2}
Thermal diffusivity	κ	10^{-6}	m^{2}s^{-1}
Reference viscosity	η_0	10^{22}	Pa s
Viscosity exponent	q	3	-
Thermal Rayleigh number	Ra	2×10^6	-
Thermal boundary layer initial thickness	d_t	66	km
Buoyancy number	B	0.5, 0.75, 1, 1.25, 2, 4, 6	-
Chemical density	$\Delta\rho_{ch}$	$B\rho\alpha\Delta T$	kg m^{-3}
Chemical Rayleigh number	Rb	BRa	-
Chemical layer initial thickness	d_{ch}	2, 4, 8, 16, 24, 32	km

The quantity of heat-producing elements in the lower mantle and the dynamic implications for small-scale structures such as ULVZs remain uncertain. For simplicity, we solve the non-dimensional energy equation for temperature without an internal heat source:

$$\frac{\partial T}{\partial t} + (\mathbf{u} \cdot \nabla)T = \nabla^2 T \tag{3.6}$$

where t is time.

The equation for chemical advection is:

$$\frac{\partial C}{\partial t} + (\mathbf{u} \cdot \nabla)C = 0. \tag{3.7}$$

We represent the ULVZ component by a set of tracer particles (initially about 100/cell) that are advected using a predictor-corrector scheme (*McNamara and Zhong*, 2004). The volume fraction of ULVZ material is proportional to the absolute local concen-

tration of tracers with a truncation applied to prevent unphysically large values (see *Tackley and King*, 2003, the truncated absolute method). In comparison to the ratio method (*Tackley and King*, 2003), this technique provides greater computational speed because fewer total tracers are required. Although the number of tracers per cell is greater for the absolute method to achieve the same resolution, a large volume fraction of ambient material in our models is devoid of tracers. By contrast, the ratio method requires tracers to fill the space of the entire domain.

3.3.2 Domain and rheology

We solve for the flow within a small region near the CMB in a cylindrical geometry. Our domain (513×145 nodes) spans approximately 23° with a height of 488 kilometers above the CMB. The radial resolution is 2 km in the lowermost 256 km of the domain. Above 256 km the grid spacing increases incrementally by 2 km to a maximum of 20 km.

Non-dimensional viscosity (normalized by η_0, see Table 3.1) follows a linearized Arrhenius law; recalling that T is non-dimensional temperature:

$$\eta(T) = \exp(-\ln(10^q)T) \tag{3.8}$$

where q specifies the order of magnitude of viscosity variation within the domain (see Table 3.1) and is largely restricted by numerical considerations. The stability of the lower thermal boundary layer is strongly dependent on q (e.g., *Yuen and Peltier*, 1980; *Loper and Eltayeb*, 1986). The background viscosity modulates the critical size

that an instability must attain before a diapir can detach from the thermal boundary layer (e.g., *Olson et al.*, 1987). Therefore, the reference viscosity η_0 (see Table 3.1) is representative of the unperturbed ambient mantle beyond the influence of the thermal boundary layer.

3.3.3 Boundary and initial conditions

The comparatively large lateral extent of the domain limits the sensitivity of the solution to the insulating sidewalls. The bottom boundary (CMB) is isothermal and free slip. We apply two different top boundary conditions. An isothermal and free-slip condition (impermeable) excessively constrains flow and retards upwellings. In contrast, a boundary prescribed by zero normal stress, zero horizontal velocities, and zero heat flux (permeable) (e.g., *Tan et al.*, 2002) lessens resistance so that instability growth accelerates. The impermeable and permeable conditions effectively bound the characteristic dynamic timescales that we expect for an evolving thin boundary at the base of a thick domain (*Olson et al.*, 1987).

Ambient deep mantle is prescribed at zero (non-dimensional) temperature, and the isothermal lower boundary is set to unity. The temperature scaling is given in Table 3.1. We apply a half-space cooling model with an age of 25 Myr to generate a lower thermal boundary layer with a thickness of $\approx$ 66 km. We place a thin layer of the chemical component at the base within the thermal boundary layer. Both the buoyancy number (B) and initial thickness (d_{ch}) are free parameters (see Table 3.1). We explore cases where d_{ch} ranges from 32 km to 2 km, which is between 2 and 33

times smaller than the initial thermal thickness. This is reasonable given the expected thickness (5–40 km) of ULVZs.

We allow the chemical layer to be swept into one coherent structure by applying a half-sinusoidal perturbation to the temperature field (initially of non-dimensional magnitude of 0.05) both radially and laterally. This permits the outcome of the different numerical experiments to be compared more readily. The size of our domain is carefully specified to focus on individual ULVZ structures and is not designed (nor suitable) to analyze the spatial distribution of many piles. Physically, our chosen initial perturbation is akin to an upwelling on the CMB caused by the (symmetric) downwelling of ambient material on either side.

3.4 Results

3.4.1 Transient period

We refer to the initial stage of the model evolution as the transient period. Although we are primarily concerned with the long-term stability and morphology of ULVZs, during this time we make several observations. We overview the evolution of four extreme cases (all impermeable), given by the following parameter values: ($B = 0.5, d_{ch} = 16$ km), ($B = 4, d_{ch} = 16$ km), ($B = 0.5, d_{ch} = 8$ km), and ($B = 4, d_{ch} = 8$ km).

For ($B = 0.5, d_{ch} = 16$ km) (Fig. 3.1), the thermal boundary layer develops two dominant instabilities within the chemical layer (Fig. 3.1A) that are ultimately over-

whelmed by the imposed long-wavelength perturbation (Fig. 3.1B). During this period, the chemical layer develops significant relief caused by the developing plumes, until the plumes merge and a large volume fraction of the layer is expelled from the CMB region (Fig. 3.1C). The buoyancy of the plume generates viscous stresses that support the relief of the remaining chemical material anchored at the CMB. Stresses reduce as the plume ascends away from the lower boundary and the convection approaches a steady state, causing a marginal reduction in relief.

The evolution for the case with the same buoyancy number, but a thinner layer ($B = 0.5, d_{ch} = 8$ km) is similar, but the dynamic timescale is reduced by several tens of million years. This occurs for all cases with a thinner layer, because less thermal buoyancy (less thickening of the boundary layer) is necessary to overcome the intrinsic density increase of the chemical layer.

For the cases with a large chemical density anomaly, ($B = 4, d_{ch} = 16$ km) and ($B = 4, d_{ch} = 8$ km), a single plume forms that marginally deflects the layer upward as it leaves the CMB region. The influence of the buoyant plume is lessened as it approaches the top of the domain, which causes the layer to flatten slightly. The large chemical density anomaly prevents substantial topography from forming on the interface.

3.4.2 Steady state

After the initial transient period, the low effective Rayleigh number ensures that almost all models reach a steady state, defined by < 1 km fluctuations (standard

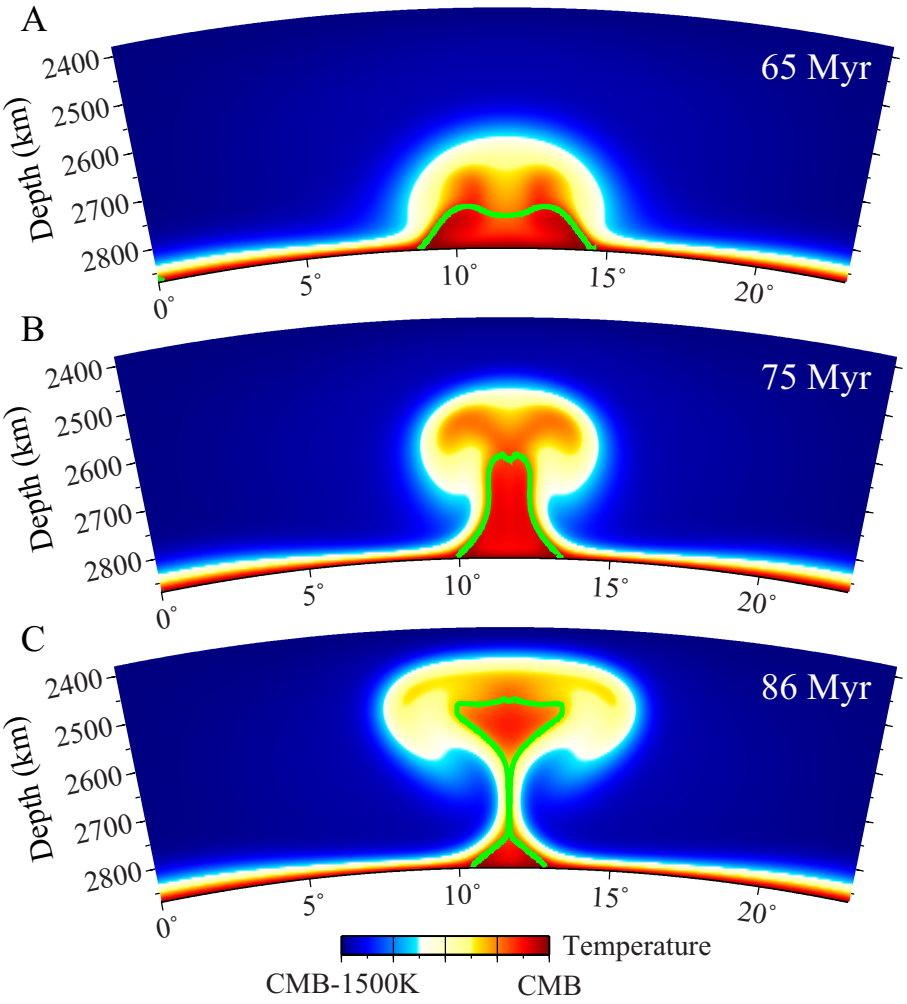

Figure 3.1: Representative behavior during the transient period for a model with a low chemical density anomaly and hence entrainment ($B = 0.5$, $d_{ch} = 16$ km, impermeable domain). The ULVZ component is contained within the area outlined in green and the CMB.

deviation) in structure height. We can thus determine several time-independent characteristics. We record the layer dimensions for the impermeable cases during a steady-state time window defined after the plume reaches the top of the domain but before the downwellings exert sufficient stress to further deform the chemical layer. The permeable cases are unaffected by return flow because material is allowed to escape from the domain.

Five impermeable cases are time-dependent because of an oscillatory flow driven by a pulsating plume that marginally raises and flattens the chemical structure. We compute the standard deviation of the maximum height (km), h_{sd}, during a stationary time window: ($B = 0.5, d_{ch} = 2$ km): $h_{sd} = 5.8$ km, ($B = 0.5, d_{ch} = 4$ km): $h_{sd} = 2.6$ km, ($B = 0.75, d_{ch} = 2$ km): $h_{sd} = 1.9$ km, ($B = 0.75, d_{ch} = 4$ km): $h_{sd} = 1.1$ km and ($B = 1, d_{ch} = 2$ km): $h_{sd} = 1.5$ km. These models are characterized by a low buoyancy number and low initial layer thickness such that the buoyancy of the chemical layer is insufficient to stabilize the flow. We time-average these cases to deduce the stationary steady-state behavior.

Fig. 3.2 depicts all of our parameter space. The relief is defined as the difference between the maximum and minimum height of the structures above the CMB over the lengthscale of the domain ($\sim$ 1400 km) at steady-state. This metric becomes less appropriate for cases where the ULVZ spreads over a distance greater than 1400 km, thus creating a ubiquitous layer with a much reduced relief even though a potentially voluminous layer exists. Although this may not occur within a larger model domain, a thick continuous layer does not satisfy the small-scale localized nature of the ULVZs.

The two largest initial chemical layer thicknesses, $d_{ch} = 32$ km and $d_{ch} = 24$ km, generally produce thick ubiquitous layers, or structures with reliefs that are too large to reconcile with seismic observations (i.e., $\gtrsim 100$ km). We therefore do not discuss these results further.

A certain volume of residual material is necessary to generate structural reliefs within the seismic estimates of 5–40 km. In these models, this can be achieved by either entraining a large amount of material from a thicker chemical layer e.g., ($B = 0.5, d_{ch} = 16$ km), or by starting with less material, e.g., ($B = 0.75, d_{ch} = 4$ km).

We plot the steady-state morphologies for the impermeable and permeable cases in Figs. 3.3, 3.4, and 3.5. Although the dynamic timescales are affected by the top boundary condition, the long-term evolution of the structures is comparable. Models with low B exhibit triangular morphologies and these shapes progressively flatten as B is increased, with the upper interface becoming more rounded. The morphologies are relatively insensitive to d_{ch}, although for reduced d_{ch} the structures exhibit slightly flatter tops (e.g., Fig. 3.3)

Entrainment modulates the quantity of material available to form the structures for $B \lesssim 0.75$. For $d_{ch} \geq 8$ km a large volume fraction of the chemical layer is entrained when $B = 0.5$, which explains the substantially reduced size of the triangular ULVZs. This effect is accentuated for the impermeable cases because of increased viscous stresses. Entrainment is most effective at early model time because viscosities and density differences are comparable (e.g., *Sleep*, 1988). For this reason, the thinnest initial layer is less affected because it is deeply embedded in the hottest,

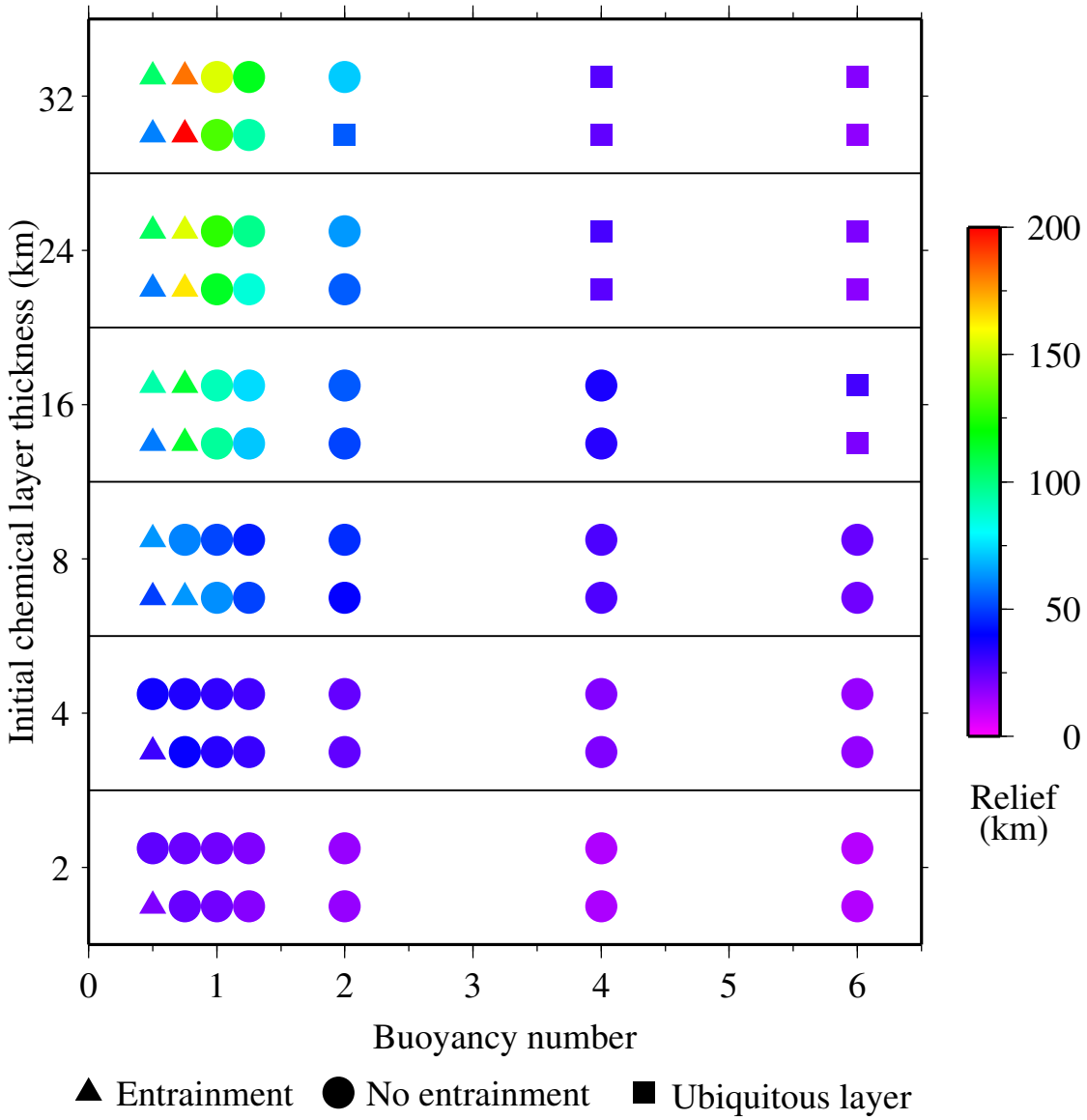

Figure 3.2: Relief of the structures at steady state. For each initial chemical layer thickness, datapoints corresponding to the impermeable cases are located above the points for the permeable cases. "Ubiquitous layer" refers to cases where the chemical layer occupies the full lateral extent of the domain.

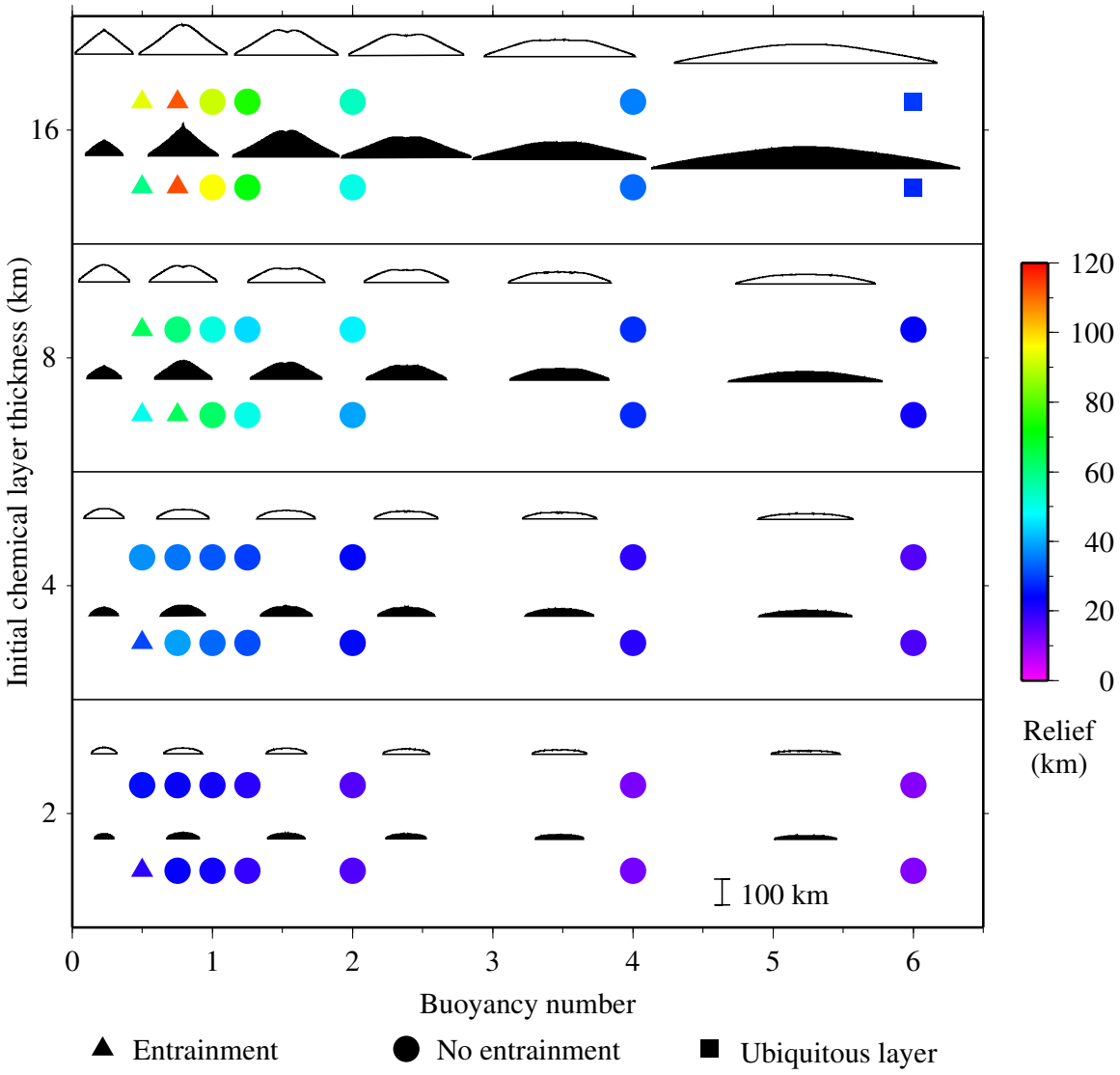

Figure 3.3: Relief of the structures at steady state. The morphologies for $B = 0.5$ to $B = 4$, plotted to scale, are shown in successive order from left to right above their corresponding datapoints. For $B = 6$ the morphologies are omitted because of space consideration but are comparable to $B = 4$. Permeable cases: black outline, impermeable cases: black fill. Note color scale is different in Fig. 3.2.

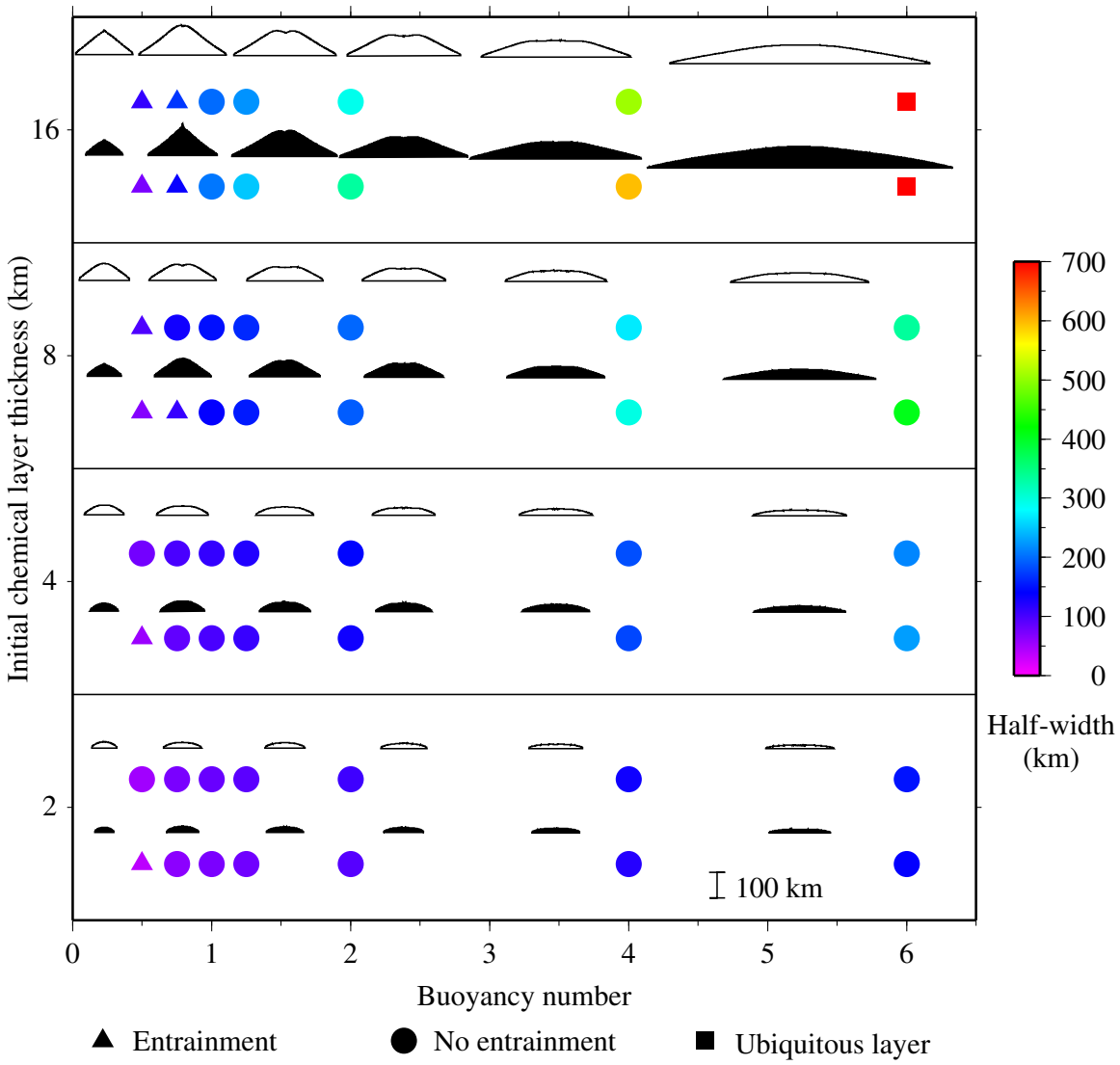

Figure 3.4: Half-width of the structures at steady state. See Fig. 3.3 caption for legend.

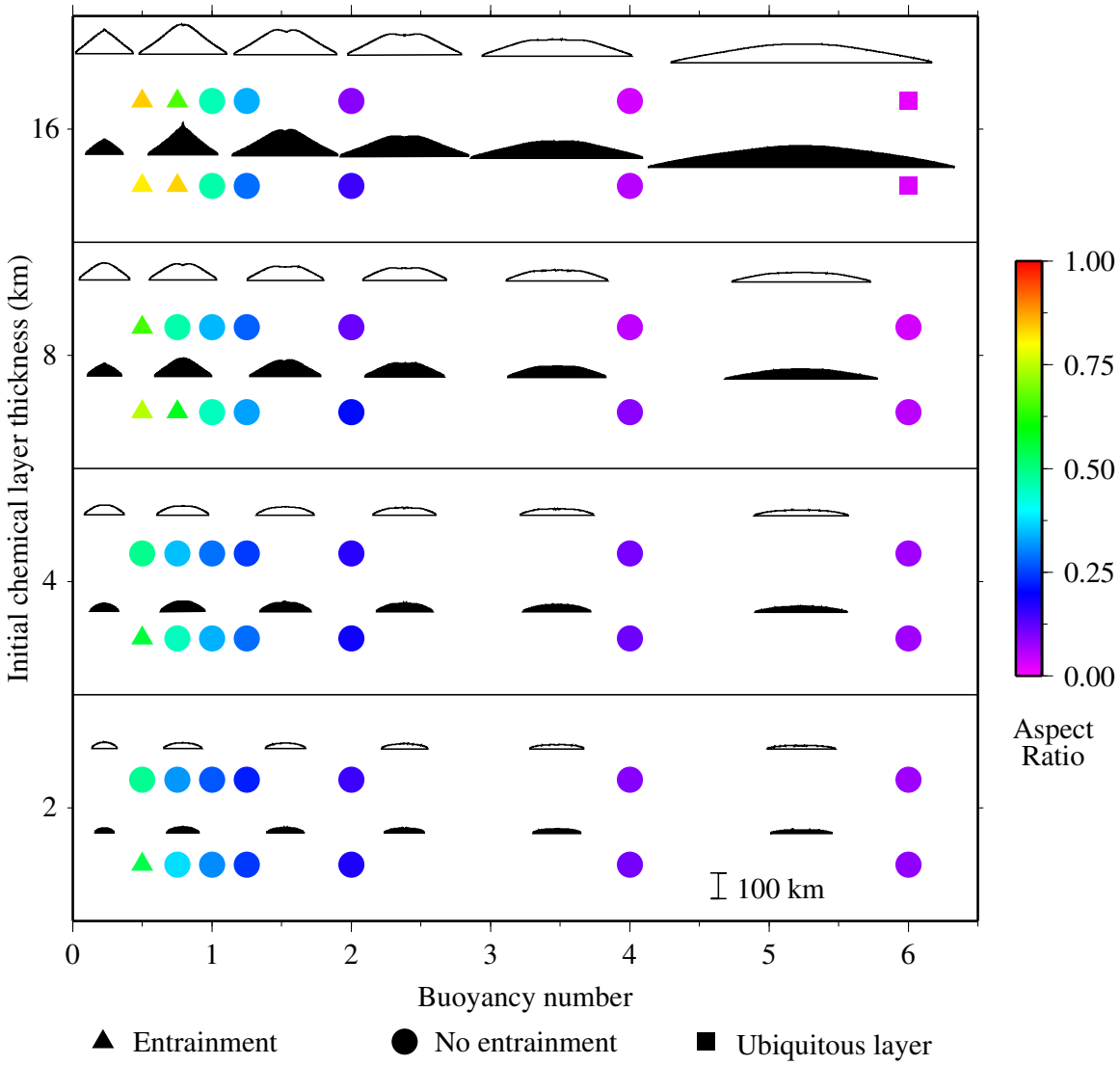

Figure 3.5: Aspect ratio (relief/half-width) of the structures at steady state. See Fig. 3.3 caption for legend.

least viscous part of the domain. *Lin and van Keken* (2006) describe the entrainment as end-member regimes, which can conveniently be applied to our models. In their regime I, the plume head is formed by ambient material above the CMB, and no chemically distinct material is entrained. This occurs for $B \gtrsim 0.75$ in our models. $B \lesssim 0.75$ is characteristic of their regime III, particularly for $d_{ch} \geq 8$ km, because the dense component predominantly accumulates at the base of the plume with some entrainment by the plume head. In addition to this complex entrainment behavior, relief varies most greatly around $B = 1$ because of the comparable thermal and chemical buoyancy (Fig. 3.3).

The half-widths of the structures vary in proportion to B (Fig. 3.4). Since d_{ch} limits the total volume of material available to form the ULVZ, the half-width also varies in proportion to d_{ch}. For $B \gtrsim 0.75$ the permeable cases produce structures that are slightly less flattened than the impermeable cases, with a subsequent reduction in half-width. The largest variations for both half-widths and relief occur for the thickest initial layer, $d_{ch} = 16$ km. In Fig. 3.5 we show that the aspect ratio (relief/half-width) of the structures is strongly dependent on B and only marginally dependent on d_{ch}.

3.5 Discussion

PKP precursors provide evidence for scatterers of varying lengthscales at the CMB (*Cleary and Haddon*, 1972). Our simulations generate structures of various shapes and sizes (e.g., Fig 3.3) which are comparable to the small-scale and large-scale features used to model broadband data (*Wen and Helmberger*, 1998b). This suggests

that solid-state ULVZs are strong candidates for the origin of the scatterers, particularly if dynamic processes sweep together several ULVZs of differing lengthscales. Many of our dynamic structures also have concave-down upper surfaces that are akin to the 2-D Gaussian shapes used to model seismic data (e.g., *Wen and Helmberger*, 1998b,a). A curved surface generates long-period PKP precursors by wide-angle reflection (*Wen and Helmberger*, 1998b), reduces the amplitudes (relative to a 1-D model) of SKS-SPdKS phases, and produces strong precursors to ScP and ScS (*Wen and Helmberger*, 1998a). The sharp tops of ULVZs inferred seismically (e.g., *Rost et al.*, 2005) motivated our *a priori* choice to define a pre-existing sharp boundary separating the chemical component from ambient mantle (e.g., Fig 3.6). If the iron-rich (Mg,Fe)O-containing component is formed through a diffusive process, for example by reactions with the core, the interface is not as sharp (e.g., *Kellogg and King*, 1993).

Countercirculation is observed in all models, and two cases are shown in Fig. 3.6. Viscous coupling is energetically favorable because it minimizes viscous shear at the material interface (e.g., *Richter and McKenzie*, 1981). Similarly, in a series of laboratory tank experiments, *Jellinek and Manga* (2002) observe a preference for material to rise along the sloping interface between a low-viscosity chemical layer and ambient material.

In Fig. 3.6A the ULVZ has sufficient thickness to greatly influence the thermal structure in the lowermost 90 km, and the two-layer convective regime is clearly revealed by Profile II in Fig. 3.6C. Isotherms are deflected to lower pressure about

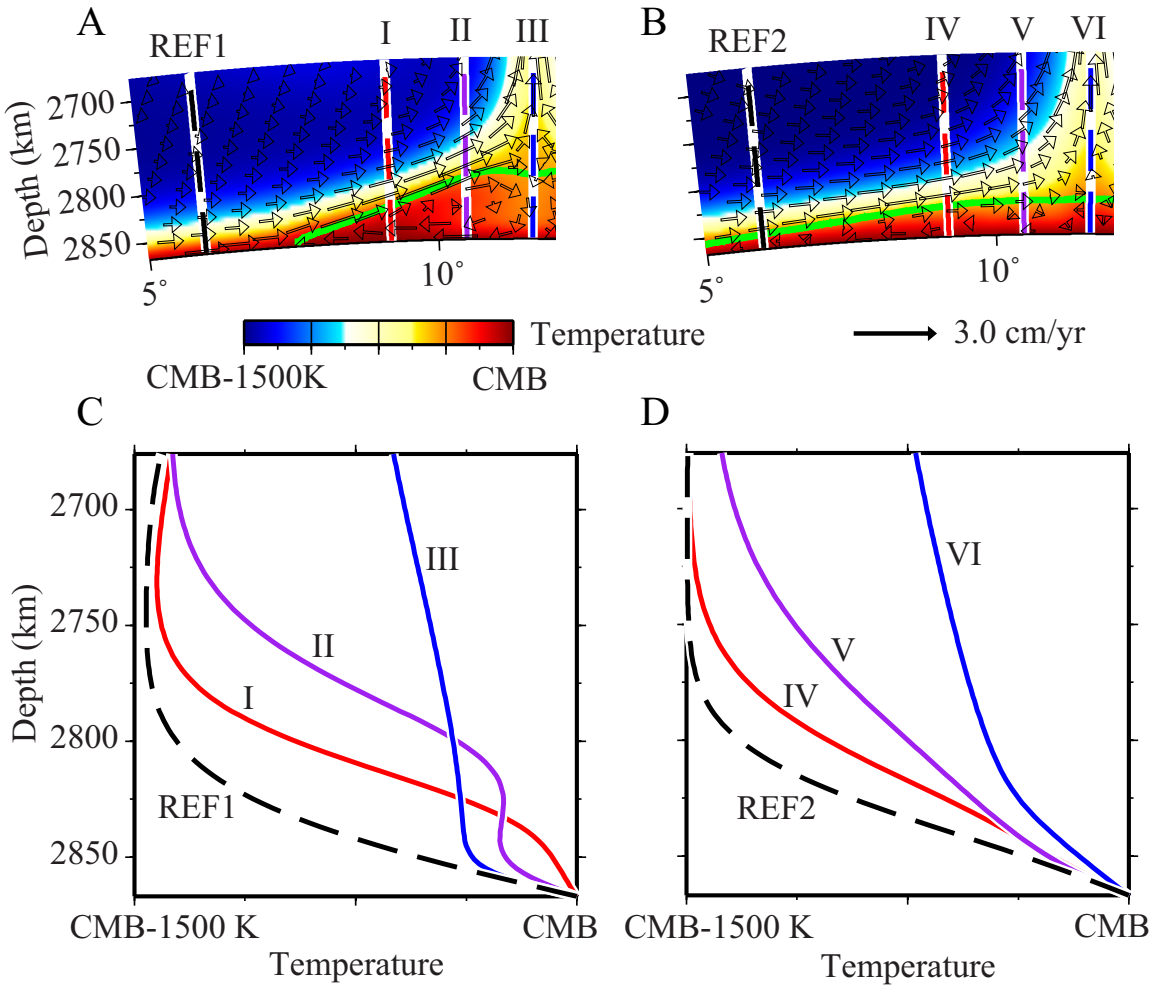

Figure 3.6: Steady-state behavior of a thin (Mg,Fe)O-containing layer. (A) Counter-circulation driven by viscous coupling ($B = 1.25$, $d_{ch} = 16$ km, impermeable domain). The ULVZ component is contained within the area outlined in green and the CMB. (C) Temperature profiles: reference REF1, upwelling I, center II, and downwelling III. (B) Sluggish convection ($B = 4$, $d_{ch} = 16$ km, permeable domain). (D) Temperature profiles (REF2, IV, V, VI) are at the same locations as in (C).

the central upwelling, which will determine the stable phase assemblages and melt generation zones. Our solid-state model does not require partial melt to account for the dynamic or wavespeed character of ULVZs, but neither is it explicitly excluded. In this regard, partial melt may explain local variations in ULVZ structure, for example beneath the Philippine-Kalimantan region (*Idehara et al.*, 2007).

For $B \gtrsim 2$, the amplitude of the steady-state perturbation of the chemical layer is much reduced, approximately 35 km in Fig. 3.6B. The velocity arrows indicate that this flow is generally sluggish with a recirculation of material accommodated by a low viscosity channel at the very base of the domain. Conduction is clearly the dominant heat-transfer mechanism (Fig. 3.6D) and the extreme outcome for this regime is a ULVZ that is subcritical to convection. In this case the ULVZ would act like a "hot plate" at the base of the mantle and simply offset the thermal boundary layer to marginally lower pressure.

Youngs and Houseman (2009) determine that half-width $\propto B^{0.38}$ and height $\propto B^{-0.39}$ based on calculations in a 3-D Cartesian geometry using an isoviscous fluid. In our models, however, we have a temperature-dependent viscosity that introduces a non-linearity which increases the complexity of the convection and questions the applicability of simple scaling relations that involve B. Given this caveat, we find that the exponent of B for half-width ranges between 0.76 and 0.37, and for the height ranges between -0.72 and -0.34.

We now consider the uncertainties in our geodynamic modeling and their implications. The Rayleigh number affects the morphology of a chemical layer and its

topography scales approximately in proportion to $Ra^{-1/3}$ (*Tackley*, 1998). We assume a thermal conductivity of around 6.6 W/m-K (e.g., *de Koker*, 2010) but larger values (around 28 W/m-K) have been reported (*Hofmeister*, 2008). The scaling relation thus predicts that the topography of the chemical layer could be 1.6 times larger than our model predicts. Similarly, an upper bound for lower mantle viscosity is two orders of magnitude larger than our reference value (e.g., *Ammann et al.*, 2010), which by itself could increase relief by a factor of 4.6. Both high thermal conductivity and lower mantle viscosity could collectively elevate the topography by 7.5 times, but mid-range estimates predict a more modest increase of a factor of 1.6.

Appropriate activation enthalpies for the deep Earth may induce an order of magnitude viscosity variation (q in Eq. 3.8) greater than 3. For example, assuming a CMB temperature of 3700 K, a low enthalpy of 500 kJ/mol (*Yamazaki and Karato*, 2001) results in $q \sim 4$, and a higher estimate of 792 kJ/mol (*Ammann et al.*, 2009) leads to $q \sim 7$. When $q \gtrsim 3$, instabilities are initially confined to the boundary layer (*Christensen*, 1984). Further increasing q reduces the onset time to instability, decreases the scale of flow, and intensifies the time dependence (*Olson et al.*, 1987). This eventually leads to a broad-scale well-mixed upwelling with low viscosity (e.g., *Christensen*, 1984; *Thompson and Tackley*, 1998). Our models do not generate this type of instability because of the reduced viscosity contrast ($q = 3$) and the imposed long-wavelength thermal perturbation. We would expect such a plume to modify the quantity of residual material at the CMB, although this regime may not be applicable to ULVZs that are only around 2 orders of magnitude weaker than the ambient

material (*Hier-Majumder and Revenaugh*, 2010).

To associate aggregate chemical density anomalies to P-wave velocity (V_P) and S-wave velocity (V_S) of the ULVZs we use a Voigt-Reuss-Hill (VRH) mixing model (see *Watt et al.*, 1976). We estimate ULVZ properties as a mixture of a silicate component and a dense oxide, and density anomalies are generated by varying the fraction of oxide in the solution. In our first mixing model we assume a disequilibrium assemblage to avoid unnecessary speculation on lowermost mantle mineralogy, and focus on the combination of properties rather than specific stable coexisting phases. The composition and properties of the silicate component are not well constrained in a chemically distinct ULVZ, so we use PREM as the model for its density and velocity. The dense oxide is assumed to be $(Mg_{0.16}Fe_{0.84})O$ magnesiowüstite (Mw), as this is the only composition for which extremely low sound velocities have been measured at appropriate pressures (*Wicks et al.*, 2010). We refer to this model as "Mw + PREM". Calculations are made at 121 GPa, the highest pressure reached in the experimental study, and our model is extrapolated to a high- (4700 K) and low-temperature (2700 K) estimate of the CMB. The temperature derivatives of velocity used are $\partial V_P/\partial T = -4.64 \times 10^{-4}$ (km/s) K^{-1} and $\partial V_S/\partial T = -3.85 \times 10^{-4}$ (km/s) K^{-1}, measured on MgO using a multi-anvil apparatus up to 24 GPa and 1650 K (*Kono et al.*, 2010). The measured thermal expansion of FeO at 93 GPa, $\alpha = 0.54 \times 10^{-5}$ K^{-1} (*Seagle et al.*, 2008), is used to estimate the temperature-dependent density of $(Mg_{0.16}Fe_{0.84})O$. Under these assumptions, our VRH mixing model produces a range of V_P and V_S for a given chemical density anomaly (Fig. 3.7A, B).

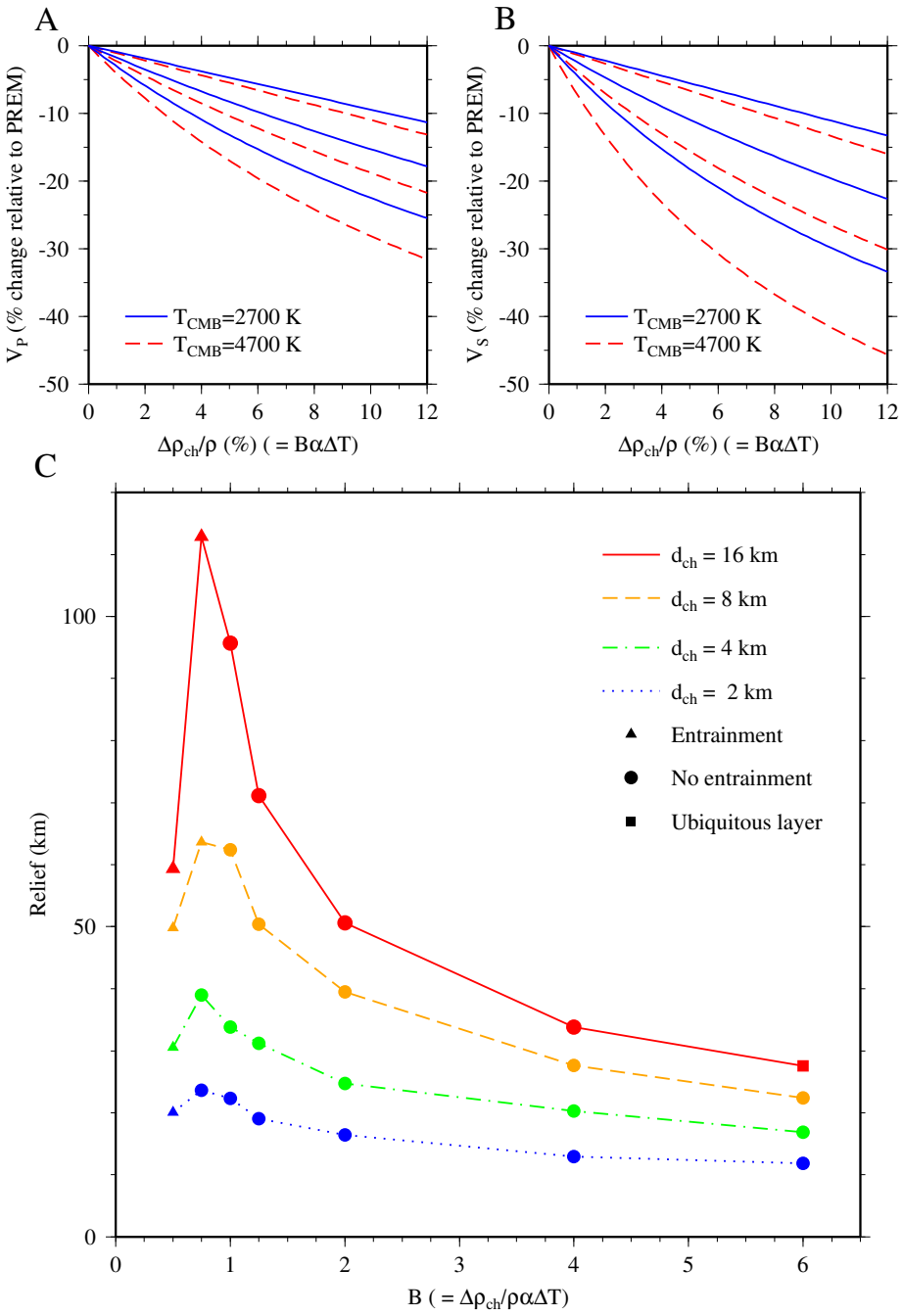

Figure 3.7: (A and B). Voigt-Reuss-Hill (VRH) wavespeed determinations at two end-member CMB temperature estimates for the "PREM + Mw" mixing model. Voigt (upper), Reuss (lower), Hill (arithmetic average). See text for model details. (C) Relief of structures for the impermeable cases

We also construct a second mixing model to consider the effects of Fe-partitioning between magnesium silicate perovskite (Pv) and Mw ("Mw + Pv"). Estimates for the Fe-partitioning between these phases approaching CMB conditions varies between $K_D^{\mathrm{Pv/Mw}} \approx 0.42$ for pyrolitic composition (*Murakami et al.*, 2005) and $K_D^{\mathrm{Pv/Mw}} \approx 0.07$ for an Al-free system (e.g., *Sakai et al.*, 2009; *Auzende et al.*, 2008). Trends indicate that $K_D^{\mathrm{Pv/Mw}}$ is likely lower at higher pressures and Fe-content, but it is not possible to reliably extrapolate from present datasets. This mixing model necessitates a small $K_D^{\mathrm{Pv/Mw}}$ to produce an equilibrium phase assemblage with a bulk density comparable to PREM and thus density anomalies (equivalently B) that are contained within the range of this study. Assuming $(Mg_{0.16}Fe_{0.84})O$ as the oxide phase and with $K_D^{\mathrm{Pv/Mw}} = 0.07$ predicts a coexisting Pv of composition $(Mg_{0.72}Fe_{0.28})SiO_3$. Such high Fe contents may be unstable in both Mw (*Dubrovinsky et al.*, 2000) and Pv (*Mao et al.*, 2005), but other experimental results indicate otherwise (*Tateno et al.*, 2007; *Lin et al.*, 2003). Possible coexistence of post-perovskite in the presence of Al and Fe adds further complication (*Andrault et al.*, 2010), so we extrapolate assuming a high CMB temperature estimate ($T_{CMB} = 4700$ K) to promote Pv as the stable silicate phase. Although the presence of Al throughout the lower mantle may alter the partitioning behavior (e.g., *Irifune*, 1994) and select thermoelastic properties (e.g., *Jackson et al.*, 2005), we focus on an Al-free system to simplify the results. The composition and properties of Pv are determined from a finite strain model (*Li and Zhang*, 2005) where effects of Fe are neglected except for a correction to the density. In exploratory models we perturbed the bulk and shear moduli due to Fe-content (*Kiefer et al.*, 2002) but

discovered this had marginal impact. We select an adiabat foot temperature for Pv that reaches 4700 K at 121 GPa and extrapolate the dense oxide to high temperature using the same procedure as previously described.

The chemical density anomalies of the mixing models can be directly associated with the buoyancy numbers used in the geodynamic calculations (Fig. 3.7C). Assuming a high (1500 K) and low (500 K) estimate for the temperature drop at the CMB, we can therefore predict a relationship between the wavespeed reduction and relief (thickness) of ULVZs. Our geodynamic models assume $\Delta T = 1500$ K (see Table 3.1), so we introduce an inconsistency by mapping the data using a reduced $\Delta T = 500$ K, but the Rayleigh number is small (a factor 2-3 difference) and does not alter the dynamics significantly. Exploring the implications of a high- and low-temperature drop at the CMB adds to the predictive capabilities of our synthesized model. For visual clarity we now plot only the Hill bound, and compare to seismic data (Figs. 3.8 and 3.9). For example, in Fig. 3.8B, the "Mw + Pv" model at 4700 K ($\Delta T = 500$ K) with relief of 95.7 km produces a V_P velocity reduction of $\sim 5\%$ with ~ 4 vol. % of Mw. In the same model, $\sim 9\%$ Mw produces a V_P reduction of $\sim 9\%$, resulting in a relief of 27.5 km.

A negative correlation between ULVZ thickness and wavespeed reduction is expected given the inherent trade-off in modeling seismic data. This is more evident with V_P (Fig. 3.8A) than V_S (Fig. 3.9A). However, this difference may be due to sampling biases. To discern V_P at the base of the mantle the original seismic studies utilize long-period data which is more sensitive to long wavelength structure. In

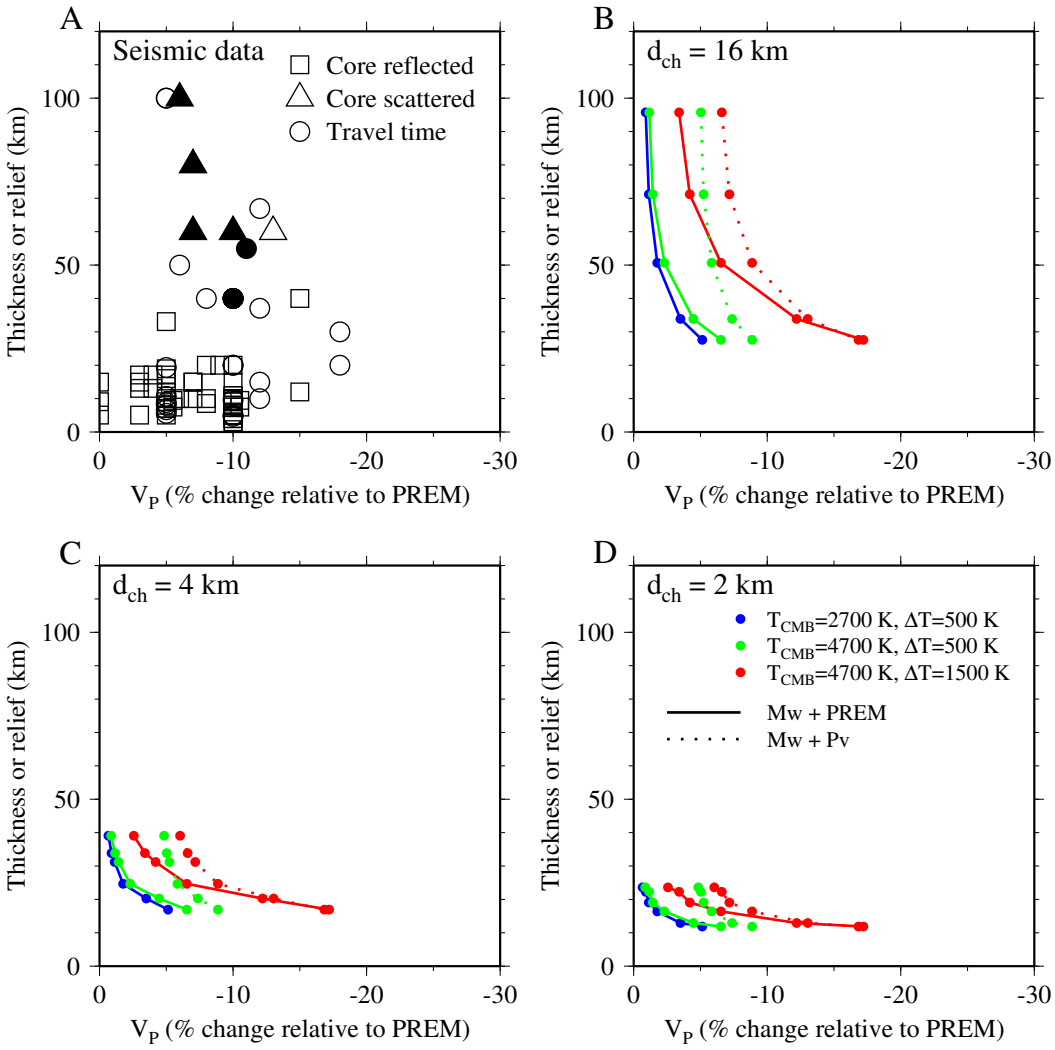

Figure 3.8: (A) Summary of seismically inferred ULVZ thicknesses and P-wave velocity reductions found globally. Following the nomenclature of *Thorne and Garnero* (2004): □ Precursors to core reflected phases (*Mori and Helmberger*, 1995; *Kohler et al.*, 1997; *Garnero and Vidale*, 1999; *Reasoner and Revenaugh*, 2000; *Havens and Revenaugh*, 2001; *Rost and Revenaugh*, 2003; *Rost et al.*, 2005, 2006; *Hutko et al.*, 2009; *Rost et al.*, 2010b), △ scattered core phases (*Vidale and Hedlin*, 1998; *Wen and Helmberger*, 1998b; *Ni and Helmberger*, 2001a; *Niu and Wen*, 2001), ◯ travel time and waveform anomalies (*Garnero et al.*, 1993b; *Garnero and Helmberger*, 1995, 1996; *Helmberger et al.*, 1996, 1998; *Wen and Helmberger*, 1998a; *Helmberger et al.*, 2000; *Simmons and Grand*, 2002; *Luo et al.*, 2001; *Ni and Helmberger*, 2001b; *Wen*, 2001; *Rondenay and Fischer*, 2003; *Thorne and Garnero*, 2004). Filled symbols denote 2-D studies. (B, C, and D) Models using the Hill bound, for various d_{ch}, temperature at the CMB (T_{CMB}), and temperature drop (ΔT). Solid lines are the "Mw + PREM" model and dotted lines are the "Mw + Pv" model.

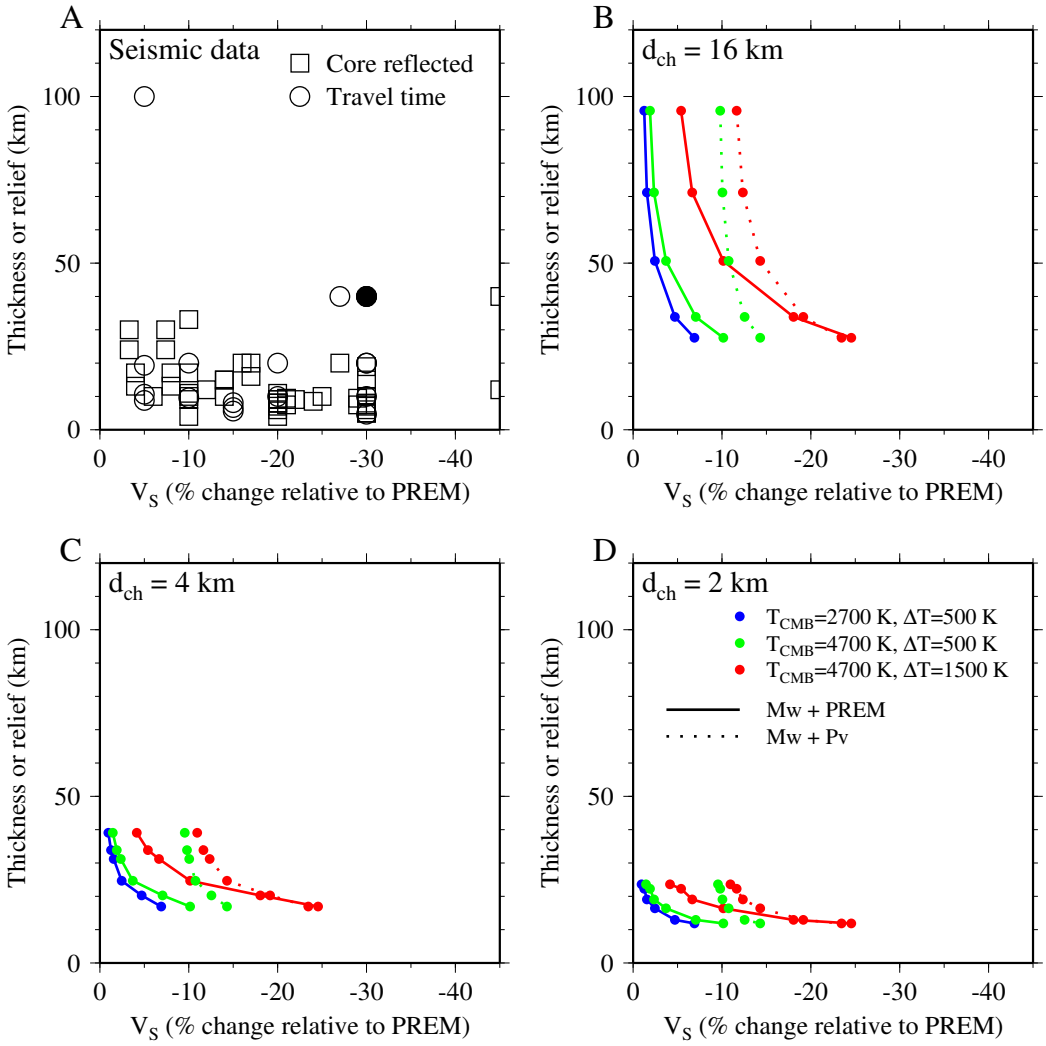

Figure 3.9: (A) Seismically inferred ULVZ thicknesses and S-wave velocity reductions found globally. Following the nomenclature of *Thorne and Garnero* (2004): □ Precursors to core reflected phases (*Kohler et al.*, 1997; *Garnero and Vidale*, 1999; *Reasoner and Revenaugh*, 2000; *Havens and Revenaugh*, 2001; *Rost and Revenaugh*, 2003; *Rost et al.*, 2005, 2006; *Avants et al.*, 2006; *Hutko et al.*, 2009; *Rost et al.*, 2010b), ◯ travel time and waveform anomalies (*Garnero and Helmberger*, 1995; *Helmberger et al.*, 1998; *Wen and Helmberger*, 1998a; *Helmberger et al.*, 2000; *Simmons and Grand*, 2002; *Ni and Helmberger*, 2001b; *Rondenay and Fischer*, 2003; *Thorne and Garnero*, 2004; *Zhang et al.*, 2009). Filled symbols denote 2-D studies. (B, C, and D) Models using the Hill bound, for various d_{ch}, temperature at the CMB (T_{CMB}), and temperature drop (ΔT). Solid lines are the "Mw + PREM" model and dotted lines are the "Mw + Pv" model.

contrast, shorter-period reflected phases are commonly used to determine V_S structure, and hence thin ULVZs are often detected. For both wavespeeds, a cluster of datapoints populate a broad range of wavespeed reductions for the thinnest ULVZs, implying substantial local variations.

The modeled V_P and V_S can reproduce the seismic observations for a reasonable range of expected temperatures and temperature drops in the CMB region. 2-D studies are denoted by filled symbols in Figs. 3.8A and 3.9A. As previously noted, the seismic data exhibits a broad scatter. Localized variations in ULVZ structure and material properties, caused by temperature or chemistry, may explain this spread. However, it is noteworthy that our synthesized model, which combines empirically determined wavespeeds with geodynamic simulations, is capable of explaining the current observations.

The PREM mixing model ("Mw + PREM") intrinsically overestimates the density and wavespeeds of the silicate component in the cases we explore here, because we do not explicitly model the silicate at high temperatures (Figs. 3.8 and 3.9). This model therefore underestimates wavespeed reductions and can be considered a lower bound. The Fe-partitioning model ("Mw + Pv") provides insight into the importance of both Fe-content and temperature in modulating the physical properties and seismic characteristics of ULVZs. Since both Mw and Pv have high Fe contents the compositional density of the assemblage is high relative to PREM and is therefore likely to form a flat layer. Higher temperatures, however, reduce total density whilst further reducing wavespeeds. At $T_{CMB} = 4700$ K the density of the silicate is sufficiently reduced

that a large volume fraction of Mw (also of reduced density) is incorporated into the assemblage to obtain PREM-like densities. This allows large wavespeed reductions for relatively small density anomalies.

There are multiple avenues for future work. Limited constraints on the chemistry and properties of the ULVZ phases under appropriate conditions introduce uncertainties into our VRH mixing model to predict expected V_P, V_S, and density anomalies. A better constraint on the temperature and phase relations in D″, coupled with sound velocity measurements of these phases at CMB conditions, would help to constrain the composition. Our geodynamic simulations assume *a priori* that there is an availability of FeO-enriched material at the base of the mantle to form ULVZs. It would therefore be useful to unravel the mechanism for creating an FeO-enriched layer to constrain its likely volume and iron content. Furthermore, our results are sensitive to the initial thickness (proxy for volume) of this layer.

3.6 Summary and conclusions

We explore the geodynamic implications of a solid iron-enriched (Mg,Fe)O layer for the origin of ULVZs. Our numerical simulations produce ULVZs with a sharp and concave-down seismic top, appropriate horizontal and vertical lengthscales, and an intrinsic density increase. Models with similar features can explain the scattering origin of PKP precursors (*Wen and Helmberger*, 1998b). The morphology and aspect ratio (relief/half-width) of the structures are strongly dependent on the buoyancy number B (or equivalently, the chemical density anomaly) and the relief (thickness)

is proportional to the initial volume of ULVZ material. Complexities in the thermal and chemical structure can promote regional variation in ULVZ character.

Wicks et al. (2010) have recently demonstrated that addition of small amounts of iron-enriched (Mg,Fe)O mixed with silicates may explain the observed reductions in wavespeeds for ULVZs. We combine our geodynamic results with a Voigt-Reuss-Hill mixing model and compare with seismic data. For reasonable estimates of the CMB temperature and temperature drop, our synthesized model satisfies ULVZ wavespeed reductions and thicknesses inferred seismically, thus lending support to a solid-state origin for many ULVZs.

Chapter 4

Enhanced convection and fast plumes in the lower mantle induced by the spin transition in ferropericlase

Originally published in:

Bower, D. J., M. Gurnis, J. M. Jackson, and W. Sturhahn (2009), Enhanced convection and fast plumes in the lower mantle induced by the spin transition in ferropericlase, *Geophys. Res. Lett.*, *36*, L10306, doi:10.1029/2009GL037706.

4.1 Abstract

Using a numerical model we explore the consequences of the intrinsic density change ($\Delta\rho/\rho \approx$ 2–4%) caused by the Fe^{2+} spin transition in ferropericlase on the style and vigor of mantle convection. The effective Clapeyron slope of the transition from high to low spin is strongly positive in pressure-temperature space and the transition broadens with high temperature. This introduces a net spin-state driving density difference for both upwellings and downwellings. In 2-D cylindrical geometry, spin-buoyancy dominantly enhances the positive thermal buoyancy of plumes. Although

the additional buoyancy does not fundamentally alter large-scale dynamics, the Nusselt number increases by 5–10%, and vertical velocities increase by 10–40% in the lower mantle. Advective heat transport is more effective and temperatures in the core-mantle boundary region are reduced by up to 12%. Our findings are relevant to the stability of lowermost mantle structures.

4.2 Introduction

A high-spin (four unpaired d electrons) to low-spin (no unpaired d electrons) electronic transition of divalent iron occurs in ferropericlase (Fp), a major lower mantle constituent, at around 50 GPa and 300 K (e.g., *Badro et al.* (2003); *Lin and Tsuchiya* (2008); *Lin et al.* (2007)). The transformation softens the elastic moduli over the transition pressure range (*Lin et al.*, 2006; *Crowhurst et al.*, 2008). *Auzende et al.* (2008) showed that the partition coefficient of iron between Fp and (Fe,Mg)SiO_3 perovskite (Pv) increases, although other experiments have shown little to no effect (*Sinmyo et al.*, 2008). These results have implications for mantle dynamics and seismic interpretation.

Theoretical (*Hofmeister*, 1999) and experimental (*Badro et al.*, 2003, 2004) studies partly motivate geodynamic simulations incorporating increases in radiative thermal conductivity and viscosity (*Matyska and Yuen*, 2005, 2006; *Naliboff and Kellogg*, 2006). However, contradictory high (*Hofmeister*, 2008; *Keppler et al.*, 2008) and low (*Goncharov et al.*, 2008) radiative conductivities need to be reconciled. Arguably, the most well-defined effect of the spin transition in pyrolite-like Fp is a 2–4% density

increase from the high to low spin state at 300 K (*Sturhahn et al.*, 2005; *Lin and Tsuchiya*, 2008; *Fei et al.*, 2007), yet the influence on mantle flow has yet to be determined. The continuous nature of the spin transition along a lower mantle geotherm (*Sturhahn et al.*, 2005; *Tsuchiya et al.*, 2006) has presumably discouraged such studies. Downwellings and upwellings may generate substantial temperature anomalies in the mantle, so that convective flow may be modified by buoyancy forces arising through the spin-state of the material.

4.3 Numerical models

4.3.1 Spin buoyancy formulation

We modify version 3.0 of the finite element code CitcomS (*Zhong et al.*, 2000; *Tan et al.*, 2007) to solve the equations for the conservation of mass, momentum, and energy for incompressible flow. We incorporate a spin-buoyancy body force similiar to a phase function formulation (*Richter*, 1973; *Christensen and Yuen*, 1985). We found that the spin function as determined from a theoretical temperature- and pressure-dependent spin-state model cannot be accurately represented analytically. We therefore pre-compute the spin-state model as a function of temperature for each pressure defined by the radial meshing. Stored as a look-up table, the code accesses and interpolates the data at each time step to determine the spin-state function. The additional body force term is equal to the spin-state function multiplied by a spin Rayleigh number. Since latent heat is a non-Boussinesq effect (*Christensen and Yuen*,

1985), the entropy changes associated with the spin transition are not included in the energy equation. In previous studies, latent heat has been found to be of secondary importance in mantle phase transitions (*Olson and Yuen*, 1982).

We select the $(Mg_{83}Fe_{17})O$ spin-state model (*Sturhahn et al.*, 2005), except that the model is translated by -10 GPa in accordance with recent experimental results showing that the transition at 300 K occurs at about 50 GPa (see *Lin and Tsuchiya* (2008) for a review). We non-dimensionalize by a surface temperature, $T_0 = 300$ K, temperature drop, $\Delta T = 2700$ K, and a pressure scale of 40 MPa/km. For this particular model, the high-low spin density contrast is reported to be 2.3%, consistent with high-pressure x-ray diffraction studies (*Lin and Tsuchiya*, 2008).

4.3.2 Model setup

We develop a suite of models with the Boussinesq approximation within a 2-D section (1 radian). The mesh size is 257 x 129 nodes with refinement in the radial direction within the boundary layers. Isothermal and free-slip boundary conditions are imposed at the top and bottom boundaries and the two sidewalls have a zero heat flux boundary condition.

Viscosity is computed by a temperature-dependent linearized Arrhenius law, $\eta(T) = \eta_0 \exp(A(0.5 - T))$, where $\eta_0 = 1$ for the upper mantle, 10 for the transition zone, and 30 for the lithosphere and lower mantle. The reference value is 10^{21} Pa·s at $T = 0.5$. The activation energy, A, and thermal and spin Rayleigh number, Ra are free parameters (Table 4.1). Ra spans a range to contrast vigourous upper mantle

convection with sluggish lower mantle convection. To ensure mobile-lid convection, we use low activation energies so that the viscosity contrast is less than four orders of magnitude. The phase changes within the mantle are not included, so that the effect of the Fe^{2+} spin transition is isolated. Internal heat sources are not considered.

4.3.3 Procedure

After integrating from a conductive temperature profile for 100,000 time steps (dimensionally several Ga) the system has a reached statistical steady state, as evident through small oscillations of the top and bottom Nusselt numbers (Nu) and the laterally averaged temperature profile. Two models are then initialized from the final state: The first with the spin transition, and the second without. Both are integrated for a further 100,000 time steps. In addition to observing the pattern of convection, we apply three measures to determine the influence of the spin transition. At steady state, we compare time-averaged top and bottom Nu's and depth profiles for the horizontally averaged temperature (reference geotherm) and RMS vertical velocity. We only report the top Nu because for most cases the Nu's differ by only a fraction of a percent (Table 4.1).

4.4 Results

The spin-state model reveals a strongly positive effective Clapeyron slope (Fig. 4.1d). Relative to the reference geotherm, this generates buoyancy by transforming cold (warm) material to the more- (less-) dense phase at a lower (higher) pressure. The

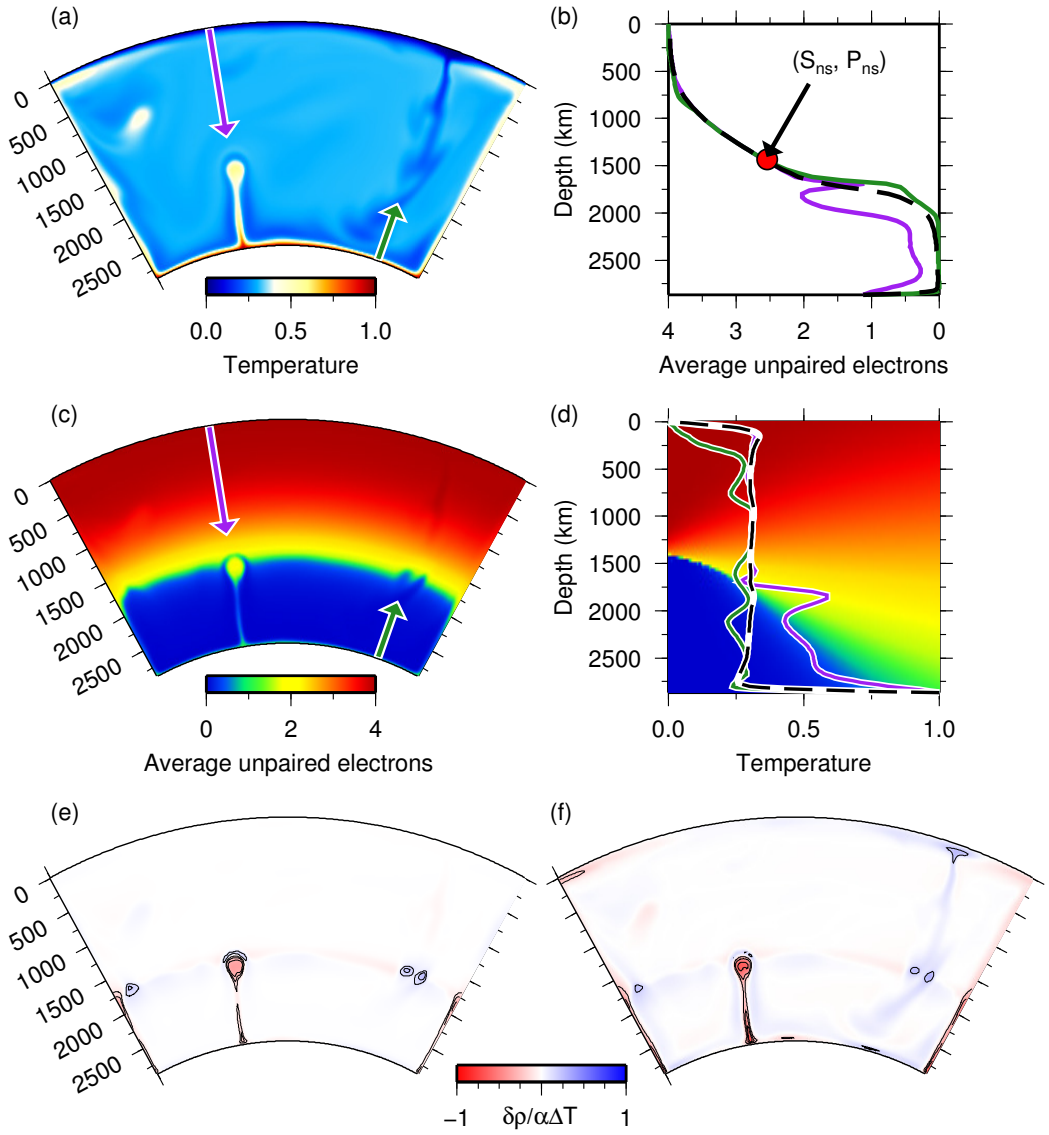

Figure 4.1: Snapshot from Case 13 at quasi-steady state. (a) Non-dimensional temperature. The purple and green lines delineate the location of representative warm and cold geotherms respectively, referred to in subsequent panels. (b) Unpaired electrons (spin-state) for representative warm (purple) and cold (green) geotherms. Red dot is (S_{ns},P_{ns}) for the spin-state model (see text). Black dashed line is the reference (horizontally averaged) spin-state. (c) Unpaired electrons with geotherm locations. (d) Geotherms with *Sturhahn et al.* (2005) spin-state model. Black dashed line is the reference geotherm. (e) Spin density anomaly, scaled by $1/\alpha\Delta T$, relative to the horizontally averaged profile. Contour interval is 0.1. (f) Total density anomaly, scaled by $1/\alpha\Delta T$, relative to the horizontally averaged profile. Contour interval is 0.2.

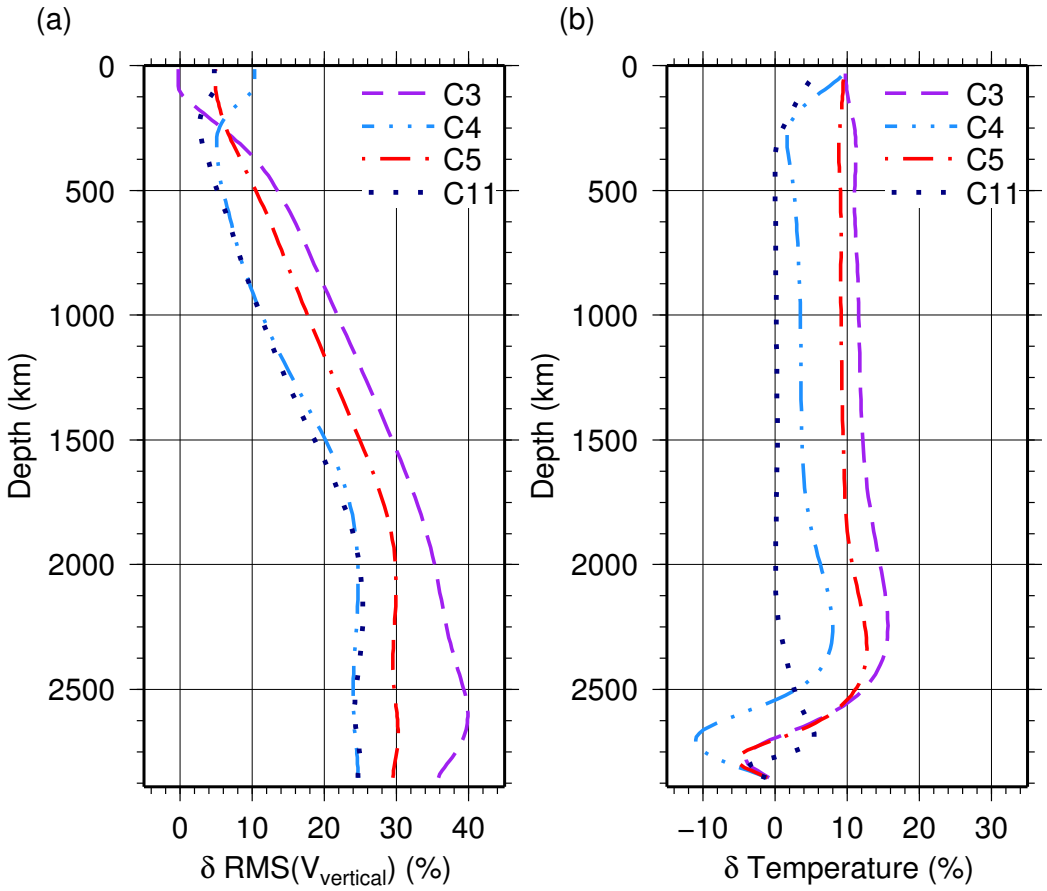

Figure 4.2: Fractional change (horizontally averaged) caused by the spin transition (%) for representative cases at quasi-steady state. (a) RMS vertical velocity. (b) Temperature

temperature broadening envelope causes cold (warm) material to transform within a tight (broad) pressure range. This introduces a neutral spin-buoyancy pressure (P_{ns}) at which the spin-state (S_{ns}), biased toward high-spin, is independent of temperature (Fig. 4.1b). This arises through the approximately temperature-independent spin contour at P_{ns}, and explains the common intersection point for the representative geotherms.

Table 4.1: Input and output characteristics of the models. Ra is the Rayleigh number, A is the activation energy, and regime indicates the style of convection. Nu is the Nusselt number and Vz is the vertical velocity at 2500 km depth. "n" and "s" subscripts denote models without and with the spin transition, respectively. A standard deviation is given for the time-dependent cases. ΔNu and ΔVz are the change in the Nusselt number and vertical velocity due to the spin transition.

Case	Input		Output						
	Ra	A	Regime	Nu_n	Nu_s	ΔNu(%)	Vz_n	Vz_s	ΔVz (%)
1	5×10^6	0	Steady	11.40	12.47	9.4	338.0	419.3	24.1
2	5×10^6	4	Steady	9.52	10.43	9.5	256.3	334.8	30.6
3	5×10^6	6	Steady	8.79	9.64	9.7	240.1	334.7	39.4
4	1×10^7	0	Steady	11.51	12.65	9.9	404.6	501.7	24.0
5	1×10^7	4	Steady	11.56	12.66	9.5	384.2	498.3	29.7
6	1×10^7	6	Steady	10.54	11.57	9.9	358.4	496.3	38.5
7	5×10^7	0	Steady	19.47	21.15	8.6	1178.5	1436.2	21.9
8	5×10^7	4	Time-dependent	18.11±0.11	19.10±0.22	5.5	959.2±15.2	1195.7±59.3	24.7
9	5×10^7	6	Time-dependent	13.10±0.61	14.13±0.62	7.9	569.4±116.9	737.7±204.9	29.6
10	1×10^8	0	Time-dependent	24.39±0.03	26.13±0.43	7.1	1702.5±2.4	2091.6±88.4	22.9
11	1×10^8	4	Time-dependent	21.37±0.49	22.67±0.41	6.1	1373.1±84.0	1707.4±115.3	24.0
12	1×10^8	6	Time-dependent	16.56±0.64	17.37±1.26	4.9	864.4±200.4	1061.2±223.1	22.8
13	5×10^8	4	Time-dependent	30.55±2.35	31.80±2.33	4.1	2981.8±639.9	3276.3±683.8	9.9

The spin transition increases vertical velocities throughout the mantle (Fig. 4.2a) with 10-40% increases in the lowermost mantle, tapering to near zero at the surface. Temperatures in the interior of the mantle are raised by up to 12%, except for the region above the core-mantle boundary (CMB) where they are reduced by an average of 5% (Fig. 4.2b). For both of these profiles, the percentage increase is inversely proportional to Ra and scales with A. The Nusselt number increases between 4 and 10% (Table 4.1) and scales inversely with Ra.

High temperatures within the lower thermal boundary layer (Figs. 4.1a and 4.1d) cause instabilities to develop with a bias toward high spin-state (Fig. 4.1c). At depth, these upwellings have both positive thermal and spin buoyancy that generates higher advective velocities (Fig. 4.2a). This increases the rate of heat removal, consistent with the reduced temperatures above the CMB in our models (Fig. 4.2b). Driving spin-state density differences in upwellings are distributed over a broad pressure range (Fig. 4.1e). As material passes through P_{ns}, the spin-buoyancy changes from working with thermal buoyancy to mildly opposing it (Fig. 4.1b). Thermal forcing continues to drive upward advection (Fig. 4.1f), albeit at a reduced velocity. Downwellings are less affected by the spin transition as the net change in buoyancy about P_{ns} is negligible because of smaller temperature differences between cold and ambient material than for warm, particularly at high pressure (Fig. 4.1d). This is controlled, in part, by the cylindrical geometry, rheological law, and pure basal heating. Driving spin-state density differences within downwellings are constrained within a comparatively tight pressure range (Fig. 4.1e). Positive spin-state buoyancy at pressures less

than P_{ns} slightly retards downward advection, but at greater pressures spin-buoyancy mildly enhances downward motion. Therefore, both upwellings and downwellings are impeded by spin-buoyancy at pressures less than P_{ns} and are enhanced at pressures greater than P_{ns}. The asymmetry ($S_{ns} < 2$) of the spin-state model ensures that a net force exists in both cases.

4.5 Discussion and conclusions

The dominant effect of buoyancy caused by the spin transition is comparable to a strongly exothermic phase change, similar to a discrete phase change (*Christensen and Yuen*, 1985). However, the nature of the Fe^{2+} spin transition generates buoyancy over a broader pressure range for upwellings than for downwellings. Spin-forcing depends strongly on temperature contrasts, with our models predicting increased plume velocities and heat transfer, and marginally reduced temperatures above the CMB. The temperature-broadening of the transition precludes significant perturbation to the bulk Earth 1-D velocity profile (*Masters*, 2008). Seismic detection will require a focus on cold slabs where the transition occurs abruptly with the potential for a seismic discontinuity. A detailed mapping of localized structures to observed seismic velocities requires more accurate knowledge of the high P-T wave speeds in candidate phase assemblages.

The spin transition, in addition to the Pv-pPv phase change, is a destabilizing mechanism in the lowermost mantle that will further work against the stability of high-density (*McNamara and Zhong*, 2005) or high-bulk modulus (*Tan and Gurnis*,

2005) structures. Furthermore, it provides additional buoyancy to small-scale hot plumes, such as those that possibly emanate from the edges of large, low-velocity structures (*Sun et al.*, 2009a). Transient systems with non-Newtonian rheology and 3-D geometry may behave differently. Additionally, iron concentration in Fp affects the transition pressure (e.g., *Fei et al.*, 2007), and iron-enriched upwellings and depleted downwellings may have different spin-state models.

Chapter 5

Lower mantle structure from paleogeographically constrained dynamic Earth models

To be submitted as:

Bower, D. J., M. Gurnis, and M. Seton (2012), Lower mantle structure from paleogeographically constrained dynamic Earth models, *Geochem. Geophy. Geosy.*

5.1 Abstract

Seismic tomography reveals two large, low-shear velocity provinces (LLSVPs) beneath Africa and the Pacific Ocean. These structures may have existed for several 100 Myrs and are likely compositionally distinct based on observed seismic, geodynamic, and mineral physics characteristics. We investigate the dynamics of the LLSVPs through the use of evolutionary models of thermochemical structures from 250 Ma to present day. We use a 3-D spherical convection model in which the anomalous structures have a high bulk modulus, consistent with seismic interpretation. A new progressive assimilation method incorporates constraints from paleogeography using a refined plate history model (with 1 Myr time spacing) to guide the thermal structure of

the lithosphere and steer the therml evolution of slabs in the uppermost mantle. The thermochemical structures deform and migrate along the core-mantle boundary (CMB), either by coupling to plate motions or in response to slab stresses. The models produce a ridge-like anomaly beneath Africa and a rounded pile beneath the Pacific Ocean. However, slabs from the Tethys Ocean push the African structure further to the southwest than inferred from tomography. Dense and viscous slabs can severely compromise the stability of high bulk modulus structures at the CMB.

5.2 Introduction

Seismic tomography (Fig. 5.1a,b) reveals two large, low-shear velocity provinces (LLSVPs) at the base of the mantle beneath Africa and the Pacific Ocean with approximately a degree-two pattern. These structures contain 1.5–2.4 vol. % and ~ 2 mass % of the mantle and occupy almost 20% surface area of the core-mantle boundary (CMB) (e.g., *Hernlund and Houser*, 2008; *Burke et al.*, 2008). A thermochemical origin is necessary to explain anti-correlated shear wave and bulk sound velocity anomalies (*Su and Dziewonski*, 1997; *Masters et al.*, 2000), putative anti-correlated shear wave and density anomalies (*Ishii and Tromp*, 1999, 2004), multipathing for waves sampling its steep edges (*Ni et al.*, 2002), and geological inferences of stability over 200–300 Myr (*Burke and Torsvik*, 2004). Waveform modeling identifies the finer-scale structure and refines the geographical extent of the LLSVPs. This technique is particularly useful to address ambiguity in tomography models by resolving the vertical extent of the structures and the wavespeed reduction and thickness of the

basal layer.

Ritsema et al. (1998) present compelling evidence for a large mid-mantle structure beneath Africa by satisfying travel-time data for S, ScS, and SKS, along a corridor from the Drake passage to the Hindu Kush. The African LLSVP rises 1500 km above the CMB with an S wavespeed reduction of 3%. This is also supported by the first arrival cross over of SKS to S from South American events to world-wide standard seismographic network (WWSSN) stations in Africa (*Ni et al.*, 1999). These early studies identify strong shear velocity gradients at the edges and top of the structure. *Ni et al.* (2002) attribute SKS waveform complexity to in-plane (2-D) multipathing and use the travel-time delays to determine a boundary width of less than 50 km. They further suggest the eastern edge of the bulk of the anomaly is tilted toward the northeast, in agreement with some tomography models (*Ritsema et al.*, 1999) (Fig. 5.1c). Alternatively, *Wang and Wen* (2007a) use more data from events northeast of the anomaly to argue that this flank tilts to the center and the basal layer extends farther northeast.

The thickness and velocity reduction of the basal layer at the CMB beneath the African structure remains contentious. Beneath the eastern part of the South Atlantic, *Wen et al.* (2001) propose a 300-km-thick anomaly with much lower S wavespeeds linearly decreasing from -2% at the top to about -10% at the base (also see *Wen*, 2002). P and S core reflected phases support this interpretation (*Simmons and Grand*, 2002). *Wen* (2001) extend this feature beneath the Indian Ocean by modeling several corridors of data and ascribe travel-time delays to variations in layer

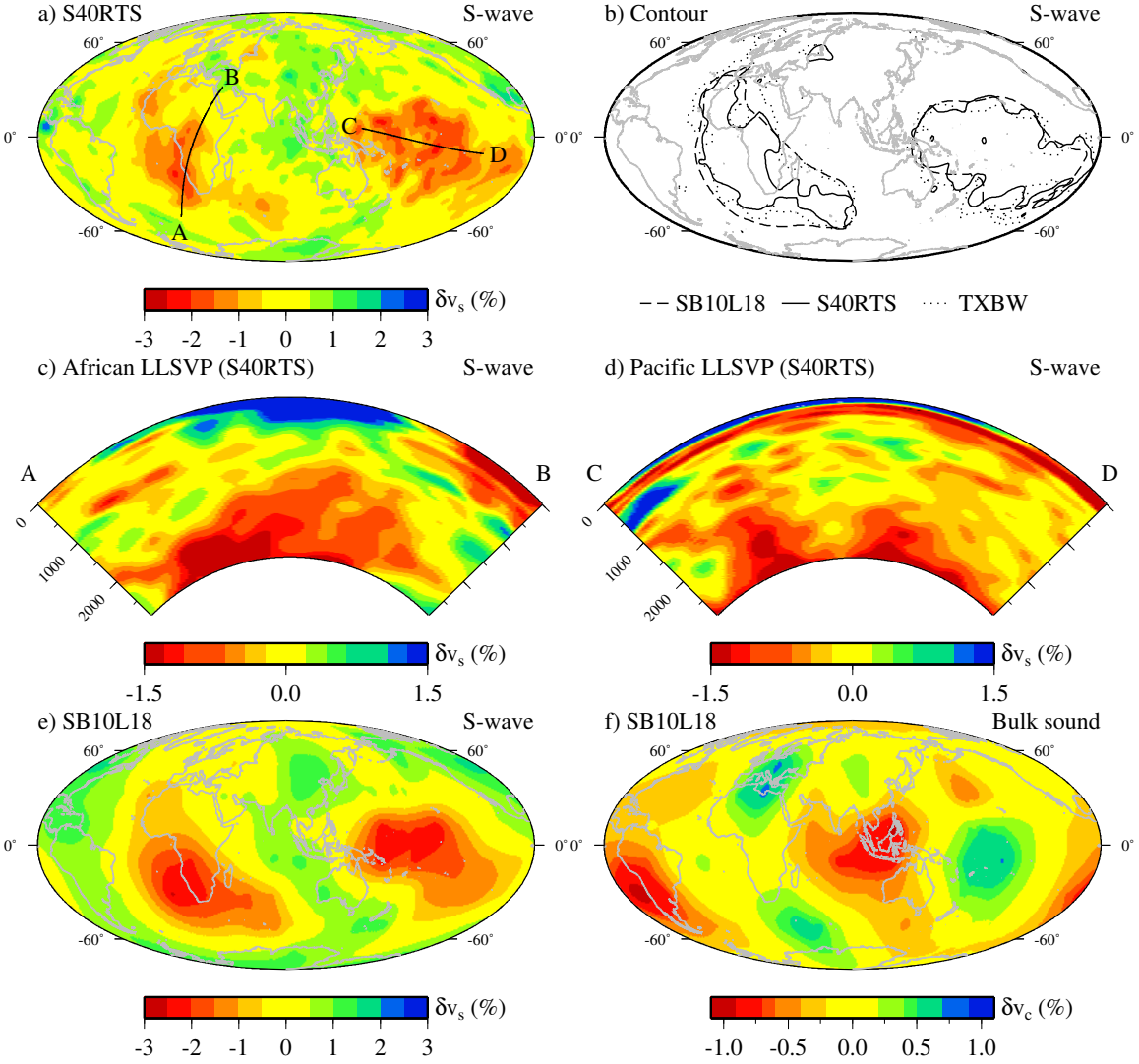

Figure 5.1: Seismic tomography data for the LLSVPs. (a, e) Shear velocity tomography models at 2800 km depth. (a) S40RTS (*Ritsema et al.*, 2011), (e) SB10L18 (*Masters et al.*, 2000). (b) -0.6% shear velocity contours from several S-wave tomography models (SB10L18, S40RTS, TXBW (*Grand*, 2002)) at 2800 km depth show that they are consistent. (c, d) Cross section through the African and Pacific LLSVPs, respectively. The color scale is saturated to highlight mid-mantle structure. Location of cross sections are marked on (a). (f) Bulk sound speed from SB10L18 (*Masters et al.*, 2000) at 2800 km depth. Note approximate anticorrelation with shear velocity in (e).

thickness. However, others favor a moderate basal layer with -3% S wavespeed (e.g., *Ni and Helmberger*, 2003b,c). This later model attributes some of the travel-time delays to the mid-mantle structure, particularly for SKS paths, and thus the basal wavespeed reduction is less. The geographical footprint on the CMB is the same regardless of the vertical extent of the anomaly (e.g., *Wang and Wen*, 2004).

Ni and Helmberger (2003a) model the 3-D geometry of the African LLSVP as a ridge-like structure approximately 1200 km high and 1000 km wide that extends 7000 km along the CMB from Africa to the Indian Ocean. By contrast, the more extreme basal layer model is compatible with a limited and localized mid-mantle extension (e.g., *Wen*, 2006). Definitive confirmation of either model is limited by sparse data coverage for azimuths other than the Drake Passage to Hindu Kush corridor (*Helmberger and Ni*, 2005). 3-D multipathing along strike of the African structure (*Ni et al.*, 2005; *To et al.*, 2005) or extreme wavespeed reductions in the basal layer can both explain delayed S-wave postcursors. New seismic tools are being developed to address such ambiguities by helping to distinguish between in-plane (2-D) multipathing caused by horizontal structure and out-of-plane (3-D) multipathing due to vertical structure (*Sun et al.*, 2009b).

The African structure also exhibits small-scale features. Ultralow-velocity zones (ULVZs) are detected at the edges of the LLSVP, with one extending at least 800 km along the eastern boundary beneath central Africa (*Helmberger et al.*, 2000; *Ni and Helmberger*, 2001a). Another is located between Madagscar and Africa (*Wen*, 2000) and a third beneath Tristan (*Ni and Helmberger*, 2001b). Shear wave anisotropy

has been interpreted as revealing complex flow occuring at the edges (*Wang and Wen*, 2007b) suggesting strong interactions between the LLSVP and ambient mantle. Recently, *Sun et al.* (2010) provide waveform evidence for a small plume with a diameter less than 150 km emanating from the top of the structure beneath southern Africa.

The Pacific LLSVP is less well imaged than its African counterpart because of source receiver geometry and its location beneath the vast Pacific Ocean. *He and Wen* (2009) construct a comprehensive model along a great arc from East Eurasia to South America using S, Sd, ScS, SKS, and SKKS phase. Their model divides the LLSVP into a western and eastern province separated by a $\sim$ 700 km gap that occurs beneath the Fiji Islands. The western province rises 740 km above the CMB and is 1050 km wide at the base, with edges conjectured to be steeper than the African structure. The eastern section is 340–650 km high and 1800 km wide. This overall geometry is also evident in tomography (e.g., Fig. 5.1d). Each province resembles a trapezoid with a lateral dimension that increases with depth with an S wavespeed reduction of 3% and 5% in the interior and basal portions, respectively (*He and Wen*, 2009). Another cross section from Fiji-Tonga to California uses multibounce S and ScS phases to overcome the lack of stations in the ocean basin (*Liu et al.*, 2011). These authors report an overall average height of 600 km with an average anomalous S velocity of -2% and make note of its geometric complexity in comparison to the apparently more simple African LLSVP.

Sharp edges are identified at the margins of the Pacific structure to the south

(*To et al.*, 2005), east (e.g., *Liu et al.*, 2011), and west (*Takeuchi et al.*, 2008). The northeast boundary abuts a ULVZ or a slow basal layer which is overlain by a high-velocity region ($\sim$ 120 km thickness) that extends further to the northeast (*He et al.*, 2006; *He and Wen*, 2009). Numerous ULVZs are detected at the southwest margin (see *Thorne and Garnero*, 2004) and a few are situated beneath the LLSVP (e.g., *Liu et al.*, 2011).

Geodynamic calculations have attempted to reproduce the long-wavelength morphology of the LLSVPs; a linear ridge-like feature beneath Africa and a rounded pile beneath the Pacific Ocean. Early 3-D Cartesian thermochemical convection studies with temperature-dependent viscosity only produce ubiquitous ridge-like features (*Tackley*, 1998, 2002). Spherical geometry alone is unable to produce rounded piles without assigning a higher intrinsic viscosity to the LLSVPs, and ridges and piles do not coexist (*McNamara and Zhong*, 2004).

Plate motion history can control the location and morphology of the LLSVPs as shown in models (*McNamara and Zhong*, 2005) that use a global tectonic reconstruction since 119 Ma (*Lithgow-Bertelloni and Richards*, 1998). *Zhang et al.* (2010) recently extended this model by constructing a few, conjectural plate stages back to 450 Ma to further investigate LLSVP mobility and stability using incompressible models with a high-density basal layer. They argue that prior to Pangea formation the African mantle was dominated by downwellings from convergence between Laurussia and Gondwana. The downwellings pushed the chemically distinct material south of Gondwana and into the Pacific hemisphere, forming a single pile. Subsequent

circum-Pangea subduction, particularly on the southeast side of the supercontinent, split the chemical pile into two, forming the African LLSVP. This suggests the Pacific structure has existed since the Early Paleozoic whereas the bulk of the African structure formed at 230 Ma, about 100 Myr after the assembly of Pangea. *Zhong et al.* (2007) show that this implies an interaction of degree-one mantle convection and the supercontinent cycle.

The reconstructed eruption sites of large igneous provinces (LIPs) (since 300 Ma) (*Burke and Torsvik*, 2004; *Burke et al.*, 2008), major hotspots (*Burke et al.*, 2008), and kimberlites (since 320 Ma) (*Torsvik et al.*, 2010) correlate with the edges of the African and Pacific LLSVPs. *Burke et al.* (2008) therefore propose that the boundaries of the LLSVPs at the CMB are 'Plume Generation Zones' (PGZs). This hypothesis suggests that the African and Pacific structures have been independent and stable since before 300 Ma and may be insensitive to plate motions, contrary to the models of *Zhang et al.* (2010). Furthermore, the existence of older LIPs (since 2.5 Ga) suggest LLSVPs earlier in Earth history, although they are not necessarily derived from the same structures that exist today (*Burke et al.*, 2008).

A chemically distinct component with a high bulk modulus (high-K) generates structures that satisfy geodynamic and seismic constraints on the LLSVPs (*Tan and Gurnis*, 2005, 2007; *Sun et al.*, 2007). Recent calculations in a spherical geometry reveal the propensity for stronger plumes to develop at the edges of such domes compared to their tops, providing a potential dynamic model for the PGZs (*Tan et al.*, 2011). Since high-K structures rely on a balance between thermal and compositional

buoyancy the net density anomaly (relative to ambient mantle) is often small. While this facilitates domes with high relief and sharp, steep boundaries, it may render the structures passive to the circulation induced by plate motions. Subduction zone geometry influences the location of the domes and therefore it may be problematic to maintain the spatial stability of high-K structures for several hundred million years (*Tan et al.*, 2011).

In this study we investigate the stability and morphology of LLSVPs with high-K in a mantle constrained by the tectonic evolution of the lithosphere from 250 Ma to the present. Our models incorporate several advances: (1) a new global tectonic reconstruction (*Seton et al.*, 2012) with continuously closing plate polygons (*Gurnis et al.*, 2012a) that has much finer spatial and temporal resolution while being consistent with the details of global geology; (2) constraints on the thermal evolution of the lithosphere through the assimilation of reconstructed seafloor ages; (3) steering the evolution of slabs in the uppermost mantle using the new tectonic reconstruction and a thermal slab model through progressive data assimilation.

5.3 Numerical models

5.3.1 Governing equations

We apply the extended Boussinesq and Boussinesq approximation (hereafter EX and BO, respectively) (*Ita and King*, 1994) to model thermochemical convection using finite element models. The finite element problem is solved with CitcomS (*Zhong et al.*,

2000, 2008) which is modified to incorporate a depth-dependent chemical density anomaly (e.g., *Tan and Gurnis*, 2007) to simulate the effect of a high bulk modulus material. The equation for the conservation of mass is:

$$\nabla \cdot \mathbf{u} = 0 \tag{5.1}$$

where $\mathbf{u}$ is velocity. The non-dimensional momentum equation is:

$$-\nabla P + \nabla \cdot \underline{\tau} = (\Gamma^{-1}\overline{\Delta\rho_{ch}}C - \bar{\alpha}T)Ra\bar{g}\hat{\mathbf{r}} \tag{5.2}$$

where P is dynamic pressure, $\underline{\tau}$ deviatoric stress tensor, α coefficient of thermal expansion, T temperature, $\Delta\rho_{ch}$ chemical density, C concentration of compositionally distinct material, Ra thermal Rayleigh number, g gravity, and $\hat{\mathbf{r}}$ radial unit vector. Overbars denote radially dependent input parameters and "0" subscripts denote dimensional reference values (Table 5.1). Maximum thermal density anomaly $\Gamma = \rho_0\alpha_0\Delta T$, where ρ_0 is density and ΔT is the temperature drop across the mantle.

The Grüneisen parameter (γ) is used *a priori* to construct the depth-dependent chemical density ($\overline{\Delta\rho_{ch}}$) by integrating the self-compression equations for two chemistries with different bulk moduli and zero-pressure density (see *Tan and Gurnis*, 2007, for details). We report the chemical density anomaly at the CMB ($\delta\rho_{ch}$) and the bulk modulus anomaly (δ K) (Table 5.2). The usual definition of the buoyancy number, B is recovered for depth-independent chemical density anomaly, $B = \Gamma^{-1}\overline{\Delta\rho_{ch}}$.

Table 5.1: Generic model parameters

Parameter	Symbol	Value	Units	Non-dim Value
Rayleigh number (Eq. 5.3)	Ra	-	-	1.83×10^8
Dissipation number	Di	-	-	1.74
Density	ρ_0	3930	kg m^{-3}	1
Thermal expansion coefficient	α_0	3×10^{-5}	K^{-1}	1
Earth radius	R_0	6371	km	1
Gravity	g_0	10	m s^{-2}	1
Thermal diffusivity	κ_0	10^{-6}	m^2 s^{-1}	1
Heat capacity	c_{p0}	1100	J kg^{-1} K^{-1}	1
Temperature drop	ΔT	3000	K	1
Reference viscosity	η_0	5×10^{21}	Pa s	1
Activation energy (Eq 5.7)	E	172	kJ mol^{-1}	6.908
Surface temperature	T_S	300	K	0.1
Heating rate	H	3.2×10^{-8}	W m^{-3}	100
Grüneisen parameter	γ	-	-	2.3

The Rayleigh number is defined as:

$$Ra = \frac{\rho_0 \alpha_0 \Delta T {R_0}^3 g_0}{\eta_0 \kappa_0} \tag{5.3}$$

where R_0 is Earth radius, η_0 viscosity, and κ_0 thermal diffusivity (Table 5.1). This definition uses the Earth radius rather than mantle thickness and is thus about an order of magnitude larger than the normal definition.

The energy equation (non-dimensional) is:

$$\bar{c_p}\frac{\partial T}{\partial t} = -\bar{c_p}\mathbf{u}\cdot\nabla T + \nabla\cdot(\bar{c_p}\bar{\kappa}\nabla T) - Di(T+T_S)\bar{\alpha}\bar{g}u_r + \frac{Di}{Ra}\underline{\tau} : \underline{\dot{\epsilon}} + H \tag{5.4}$$

where c_p is heat capacity, $Di = \alpha_0 g_0 R_0 / c_{p0}$ is dissipation number, T_S is surface temperature, $\underline{\dot{\epsilon}}$ is strain rate tensor, and H is internal heating rate (Table 5.1).

The usual definition for the Boussinesq approximation ignores depth-dependent

material properties and heating terms involving Di. However, since high-K structures necessitate pressure-dependent parameters, our BO models only neglect the additional heating terms ($Di = 0$).

The equation for chemical advection is:

$$\frac{\partial C}{\partial t} + (\mathbf{u} \cdot \nabla)C = 0. \tag{5.5}$$

We advect tracers representing the chemical components using a predictor-corrector scheme (*McNamara and Zhong*, 2004) and determine composition using the ratio method (*Tackley and King*, 2003).

5.3.2 Model setup

The full sphere is constructed of 12 caps, each with 128×128×64 elements, giving a total of $\sim$ 12.6 million elements. Radial mesh refinement provides the highest resolution of 18 km in the boundary layers and a minimum resolution 90 km in the mid-mantle.

High-K domes can form for a range of thermal expansion profiles that decrease with pressure from the surface to the CMB (see *Tan and Gurnis* (2007), Fig. 3). Conversely, the behaviour of thermal slabs is extremely sensitive to this reduction. Too large of a decrease will invariably hinder and potentially stall downgoing slabs, particularly when coupled with a stiff lower mantle (*Hansen et al.*, 1991, 1993). To facilitate interaction between the domes and slabs we therefore opt for a simple parameterization to decrease the thermal expansion coefficient with pressure by a factor

m_α across the mantle:

$$\bar{\alpha} = \frac{1}{2}\left(\frac{r_o - r}{r_o - r_i} + m_\alpha \frac{r - r_i}{r_o - r_i}\right) \tag{5.6}$$

where $r_o = 1$ is the (non-dimensional) outer radius of the sphere and $r_i = 0.55$ is the inner radius. Varying m_α allows us to compare slab descent rates in the lower mantle with estimates using geological tomography correlations (*van der Meer et al.*, 2010). Note that our definition of m_α is different from that used by *Tan and Gurnis* (2007). Our formulation sets the thermal expansion coefficient at the CMB to eliminate a trade-off with the magnitude of the chemical density profile. The thermal expansion at the surface is a factor of m_α larger. Therefore, advective heat transport is enhanced for models with a larger m_α because the effective Rayleigh number is greater, particularly in the uppermost mantle.

Our CMB thermal expansion coefficient is dimensionally 1.5×10^{-5} K^{-1}, which compares favorably with $MgSiO_3$ perovskite at 88 GPa and 3500 K (*Oganov et al.*, 2001; *Marton and Cohen*, 2002) and is slightly larger than bulk mantle estimates of approximately 1×10^{-5} K^{-1} (*Stacey*, 1977; *Hama and Suito*, 2001). We define the reference thermal expansion coefficient $\alpha_0 = 3 \times 10^{-5}$ K^{-1} (*Stacey*, 1977), which is also comparable with perovskite at ambient conditions (*Katsura et al.*, 2009).

We adopt a purely diffusion creep constitutive relation which is likely to be appropriate for the lower mantle (*Karato and Li*, 1992). Dislocation creep and yielding are critical for the motion of plates and slabs (*Billen and Hirth*, 2007; *Stadler et al.*, 2010). However, because of assimilated plate kinematics and slab structure in the upper mantle (see next section) we effectively remove the need to include these com-

plexities. Viscosity (non-dimensional) is composition dependent:

$$\eta(T, r) = \eta_0(r)(1 + \eta_C C) \exp[E(0.5 - T)] \tag{5.7}$$

where $\eta_0(r)$ is a radially dependent prefactor, η_C is intrinsic compositional viscosity prefactor, and E is non-dimensional activation energy. $\eta_0(r) = 1$ for the lithosphere (0–100 km depth) and $\eta_0(r) = 1/30$ for the upper mantle (100–670 km depth). For the lower mantle $\eta_0(r)$ increases linearly from 2.0 at 670 km depth to 6.8 at the CMB (*Zhang et al.*, 2010). This pressure-induced viscosity increase offsets the decrease caused by the adiabatic temperature gradient. $E = 6.908$ generates 10^3 viscosity variation due to temperature (Table 5.2).

We apply a free slip and isothermal ($T = 1$) boundary condition at the CMB and a kinematic and isothermal ($T = 0$) boundary condition at the top surface. The upper thermal boundary layer is characterized by large velocity gradients and high viscosity due to the temperature-dependent rheology and the imposed 30× step increase from the upper mantle. In the EX framework viscous dissipation produces intense localized heating at plate boundaries. This produces large gradients in strain rate and viscosity which can cause numerical difficulties. Furthermore, a range of deformation mechanisms operate in the lithosphere that cannot be simply modeled by diffusion creep. We therefore set the dissipation number, Di to zero for depths less than 325 km.

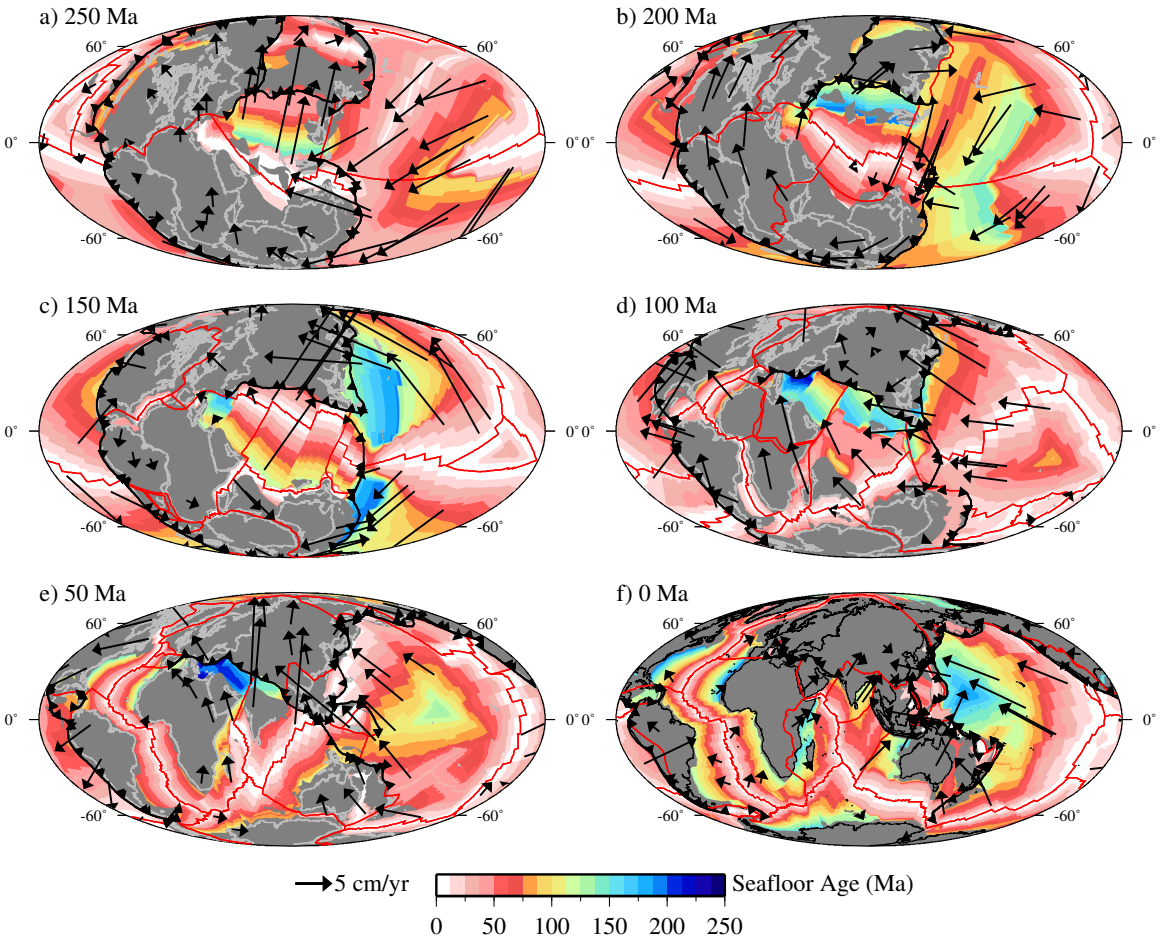

Figure 5.2: Snapshots of the plate tectonic reconstruction (*Seton et al.*, 2012) (a) 250 Ma, (b) 200 Ma, (c) 150 Ma, (d) 100 Ma, (e) 50 Ma, (f) present day. Ridges and transform faults are represented by red lines and subduction zones are represented by black lines with sawteeth indicating polarity. Non-oceanic regions are dark grey and reconstructed continents with present-day shorelines are shown in light grey (except black for the present day).

5.3.3 Data assimilation

We use progressive assimilation of a thermal and kinematic model of surface plate evolution with continuously closing plates at 1 Myr intervals (Fig. 5.2) (*Seton et al.*, 2012). The plate motion model is based on a merged moving Indian/Atlantic hotspot reference frame (*O'Neill et al.*, 2005) for the past 100 Myrs and a true polar wander-corrected reference frame (*Steinberger and Torsvik*, 2008) for older times. The Pacific is anchored to fixed Pacific hotspots prior to 83.5 Ma based on a merged *Wessel et al.* (2006) and *Wessel and Kroenke* (2008) reference frame. The proto-Pacific/Panthalassa evolved from an Izanagi-Farallon-Phoenix triple junction. Importantly, the plate model incorporates the break-up of the Ontong Java-Manihiki-Hikurangi plateaus between 120-86 Ma. The Tethys Ocean is reconstructed largely based on a combination of *Stampfli and Borel* (2002) and *Heine et al.* (2004). GPlates (*Gurnis et al.*, 2012a) exports plate velocities from the digitized plate boundary dataset, providing the kinematic boundary condition on the top surface with linear interpolation between the plate model ages. Therefore, in the convection calculations we do not remove net angular momentum or rigid body rotation.

We create a thermal model for the lithosphere using reconstructed seafloor ages and a half-space cooling model (Fig. 5.3). A thermal age of 200 Ma is assigned to non-oceanic regions. At each time step in the computation, for depths $\leq$ 60 km, the code blends the lithosphere thermal model with the temperature field from the previous time step (see, *Matthews et al.*, 2011, for details). This approach suppresses convective instabilities away from convergent plate margins and dictates the global

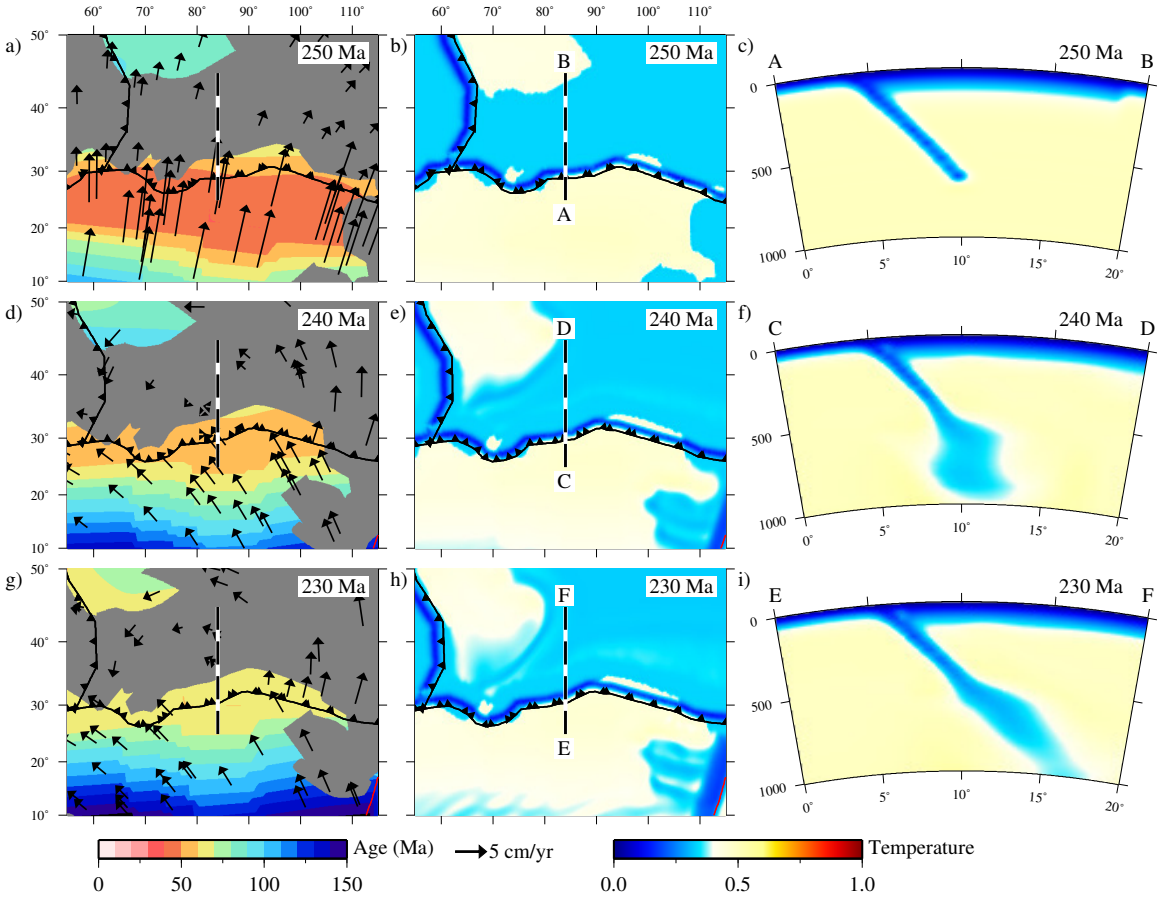

Figure 5.3: Progressive data assimilation example for the convergence of the Paleo-Tethys Ocean and Laurussia (Model EX1). Plate history and age of oceanic lithosphere model (a) 250 Ma, (d) 240 Ma, (g) 230 Ma. Temperature field at 110 km depth (b) 250 Ma, (e) 240 Ma, (h) 230 Ma. Cross section of slab (c) profile A–B, 250 Ma, (f) profile C–D, 240 Ma, (i) profile E–F, 230 Ma. Ridges and transform faults are represented by red lines and subduction zones are represented by black lines with sawteeth indicating polarity. Non-oceanic regions are dark grey.

surface heat flux.

To construct a thermal slab model we use the paleolocation and age of the oceanic lithosphere at convergent plate margins. We then select a slab dip angle (45° for simplicity) and apply a half-space cooling model either side of the slab center line to conserve buoyancy. This thermal structure is assimilated at each time step using a blending stencil. The method ensures that slab buoyancy in the upper mantle is consistent with surface plate evolution and allows our simulations to capture the essential aspects of subduction such as asymmetric geometry and slab roll-back (see, *Gurnis et al.*, 2012b, for details).

5.3.4 Parameter space

The height of high-K domes will adjust according to the height of neutral buoyancy (HNB) as dictated by material properties and temperature contrasts (*Tan and Gurnis*, 2005). To estimate the expected temperature differences we run a preliminary BO model with the same parameters as BO5 (Table 5.2). An internal heating rate $H = 100$ accounts for around 60% of the total heat flux. In the preliminary model, the interior temperature of the domes reaches a steady-state $T \approx 0.83$ (dimensionally ≈ 2800 K) but the ambient material temperature evolves as relatively cold slabs accumulate at the CMB. At 250 Ma (model start time) the ambient material outside of the domes has an average temperature of $T = 0.5$ and cools to $T = 0.43$ at the present day. The assimilation method is not unduly affected by this cooling because the efficient advection of slabs ensures that the uppermost mantle temperature re-

Table 5.2: Model-specific parameters. [a] Lithosphere and slab assimilation. [b] This calculation assumes the domes are 1000 K hotter than ambient material, which is appropriate for the start of the model but evolves as slabs cool the mantle.

Model	Input							Output
	Approx	Ra	Assim[a]	$\delta\rho_{ch}$ (%)	δ K (%)	m_α	η_C	HNB (km)[b]
EX1	EX	1.83×10^8	Y	1.8	6	2	0	700
EX2	EX	1.83×10^8	Y	1.9	9	3	0	700
EX3	EX	1.83×10^8	Y	1.7	4	1	0	700
BO1	BO	1.83×10^8	Y	1.8	6	2	0	700
BO2	BO	1.83×10^8	Y	2.5	6	2	0	-
BO3	BO	1.83×10^8	N	2.5	6	2	0	-
BO4	BO	1.83×10^8	Y	2.5	6	2	100	-
BO5	BO	1.83×10^8	Y	$B = 0.5$		1	0	-
BO6	BO	1.83×10^7	Y	2.5	6	2	0	-

mains close to $T = 0.5$. Rather, the dominant influence of this temperature change is to increase the HNB. Mantle cooling will be less for the EX models because the reduction in the thermal expansion coefficient with pressure will hinder the advection of material and slabs will warm through diffusion. Nethertheless, this basic analysis provides a convenient method to determine the likely evolution of high-K structures without necessitating many expensive computations (Table 5.2).

Tan et al. (2011) generate high-K domes within a spherical geometry free-convection model for density contrasts at the CMB between $\approx$ 1–2%. We anticipate requiring upper values from this range for the domes to remain stable during 250 Myrs of tectonic evolution.

5.3.5 Initial condition

Precalculations without data assimilation reveal that about 700 Myr is required for high-K material to develop into high standing structures from an initial layer at the

CMB. At the start of our models (250 Ma) we therefore choose to prescribe two domes centered on the equator at 0 and 180 degrees longitude (for the African and Pacific structures) with a footprint that together occupies 20% of the CMB surface area (Fig. 5.1b). The domes are essentially located in the present day position of the LLSVPs, with the African structure marginally further north and the Pacific structure displaced slighly west (Fig. 5.4a). For simplicity we define a height of 900 km for the domes and accept that this will adjust to the HNB (Fig. 5.4d). The total volume of both structures is approximately 34.4×10^9 km^3 which is comparable to the volume of a 200-km-thick layer residing at the CMB. This volume is about a factor of 2 larger than estimates from seismic tomography (*Burke et al.*, 2008; *Hernlund and Houser*, 2008), but comparable to other geodynamic studies (*McNamara and Zhong*, 2005; *Zhang et al.*, 2010). Additionally, entrainment reduces the size of the structures during the model run.

Ambient mantle is assigned a non-dimensional temperature $T = 0.5$ and in the interior of the structures $T = 0.8$. This approach effectively assumes that most of the domes existed as two coherent and relatively well-mixed structures prior to the early Mesozoic. Thin thermal boundary layers (≈ 80 km) conduct heat from the CMB and the top of the domes to ambient mantle. The thermal model for the lithosphere and slabs is described in Section 5.3.3. Slabs are initially inserted from the surface to the base of the transition zone (670 km depth).

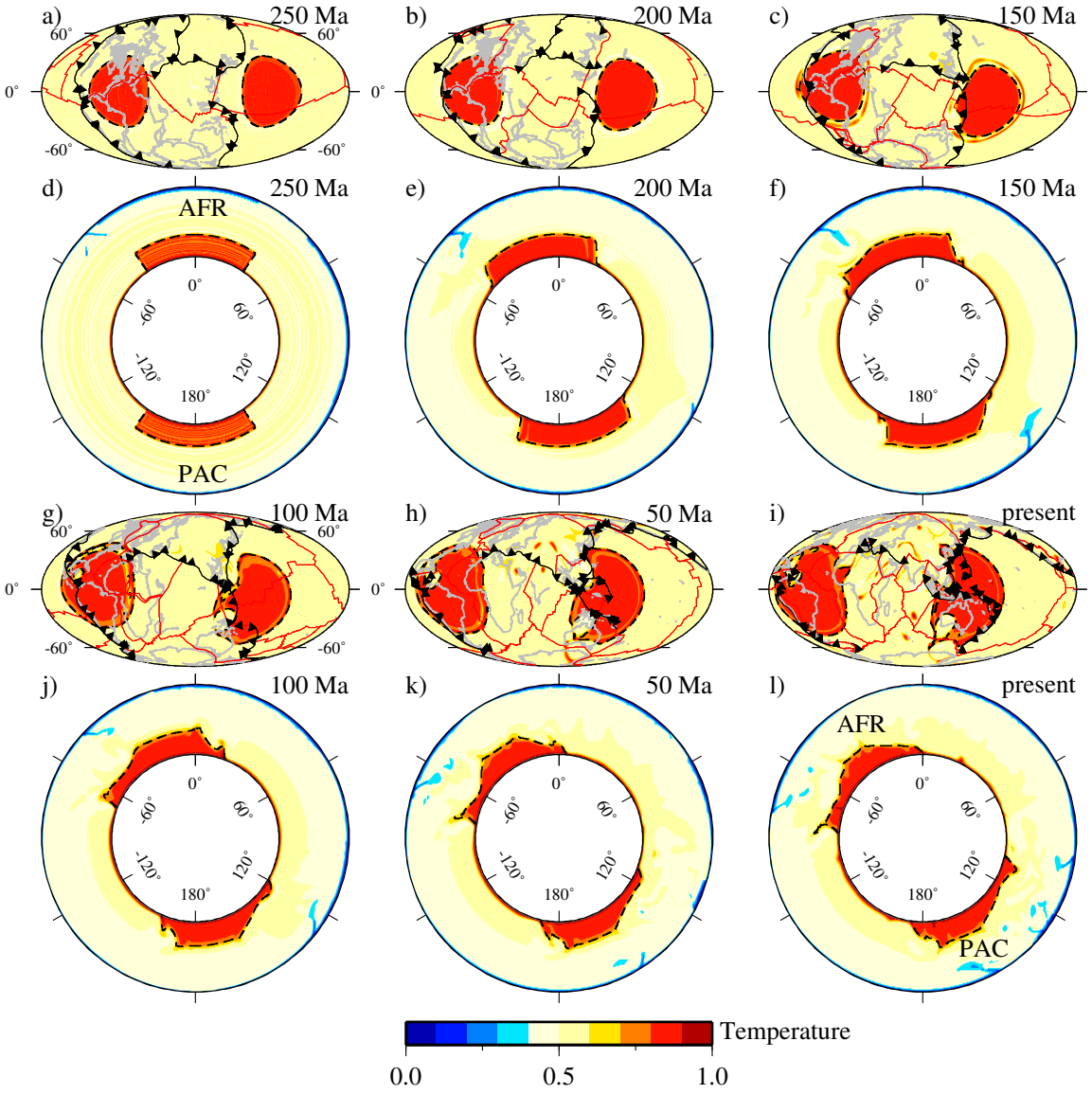

Figure 5.4: EX1 snapshots. (a, b, c, g, h, i) Temperature at 2600 km depth for 250, 200, 150, 100, 50 Ma and present day, respectively. The compositionally distinct material is contoured with black dashed lines. Ridges and transform faults are represented by red lines and subduction zones are represented by black lines with sawteeth indicating polarity. Reconstructed continent outlines are shown in light grey. (d, e, f, j, k, l) Equatorial annuli of temperature (0° is the Prime Meridian) for (a, b, c, g, h, i), respectively. "AFR" and "PAC" identify the domes.

5.4 Results

Fig. 5.4 illustrates the evolution of our reference model (EX1), which also encapsulates the key features of EX2 and EX3 (Table 5.2). During the initial 75 Myrs the African structure is displaced northwards and the Pacific structure southwards (Figs. 5.4a,b,c). The high-K structures retain their steep vertical walls and topography on the interface is negligible. This demonstrates *a posteriori* that the initial thermal and compositional structure for the domes (Fig. 5.4a,d) is dynamically compatible with the parameters of the calculations. Plate motions then shift both structures westward from $\sim$ 175 Ma to present day (Fig. 5.4g,h,i). The final position of the African structure is beneath the Atlantic Ocean and South America, while the Pacific structure is beneath the western Pacific Ocean and Australasia (Fig. 5.4i).

Neither dome experiences significant deformation since the initial prescribed geometry is largely retained. However, subducting slabs generate stresses that deflect the top interface of the domes and can produce extensive topography. For example, slabs originating from Central American subduction depress a western portion of the African structure by several hundred kilometers (Fig. 5.4k,l, at -60°). Circular embayments punctuate the edge of the domes (Fig. 5.5, green arrows). These produce tendrils of chemically distinct material that extend away from the structures and join ridges of thickened boundary layer of ambient material (Fig. 5.5, red arrow). Slabs are generally contained within the upper half of the mantle and do not accumulate at the CMB.

Classical thermal plumes (spheroidal plume head followed by a tail) of ambient

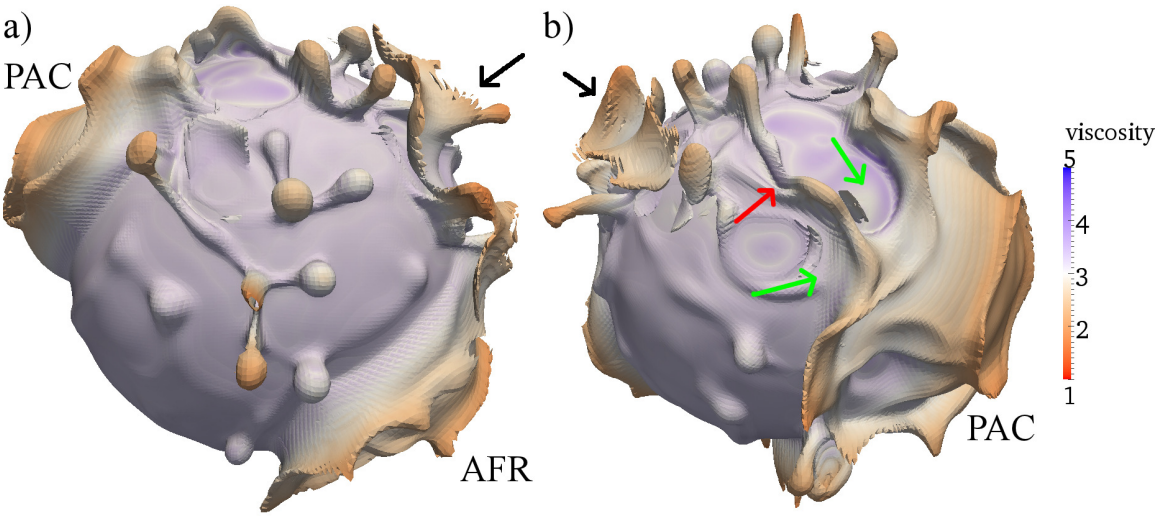

Figure 5.5: Thermal plumes rising from ridges between the domes at present day (EX1). The $T = 0.6$ isosurface is coded by viscosity for depth perception (viscosity is pressure dependent). (a) View from the North Pole. The Pacific (PAC) and African (AFR) structures are the prominent red-capped mesas. The contiguous band of elevated temperature that is disconnected from the CMB is caused by dissipative heating from Tethyan slabs (black arrows). (b) View centered on (90°, 0°) showing the western edge of the Pacific dome, circular embayments (green arrows), and tendrils extending from the domes (red arrow)

material develop from interconnected ridges of thickened boundary layer at the CMB. These are generally located away from the domes (Fig. 5.5) with more upwellings beneath Africa and Eurasia than the Pacific region. The high-K structures develop a perimeter of thickened boundary layer, although the edges are not prefered regions of plume formation.

EX2 and EX3 have different drops in thermal expansion across the mantle (factor of 3 and 1, respectively) and chemical density profiles compared to EX1. With a comparable HNB these models are qualitatively similar to the reference model. The domes in EX2 are marginally flatter with less edge deformation, and plume activity is also reduced. Conversely, the structures in EX3 stand a little higher from the CMB and have steeper sides. In this model, downwellings more significantly deform the domes. For example, Central American slabs produce sufficient stresses to generate a large circular embayment in the north of the African structure. To a lesser extent, displacement of material away from Central America also occurs in EX1 (Fig. 5.4g,h,i).

The Boussinesq equivalent of EX1 (BO1) does not produce stable domes (Fig. 5.6). Slabs are stronger in BO1 because they have more thermal buoyancy, and are therefore cooler and more viscous at all mantle depths because the transit time through the mantle is reduced ($\sim$ 50 Myr). The slabs exert large stresses on the side walls of the domes and can slide beneath the high-K structures, further destabilizing them. Ultimately the domes rise off the CMB (Fig. 5.6f). In BO2, we increase the density contrast at the CMB ($\delta\rho_{ch}$) whilst retaining the same bulk modulus anomaly. In this model, the structures remain stable at the CMB until $\sim$ 70 Ma (Fig. 5.7c,e).

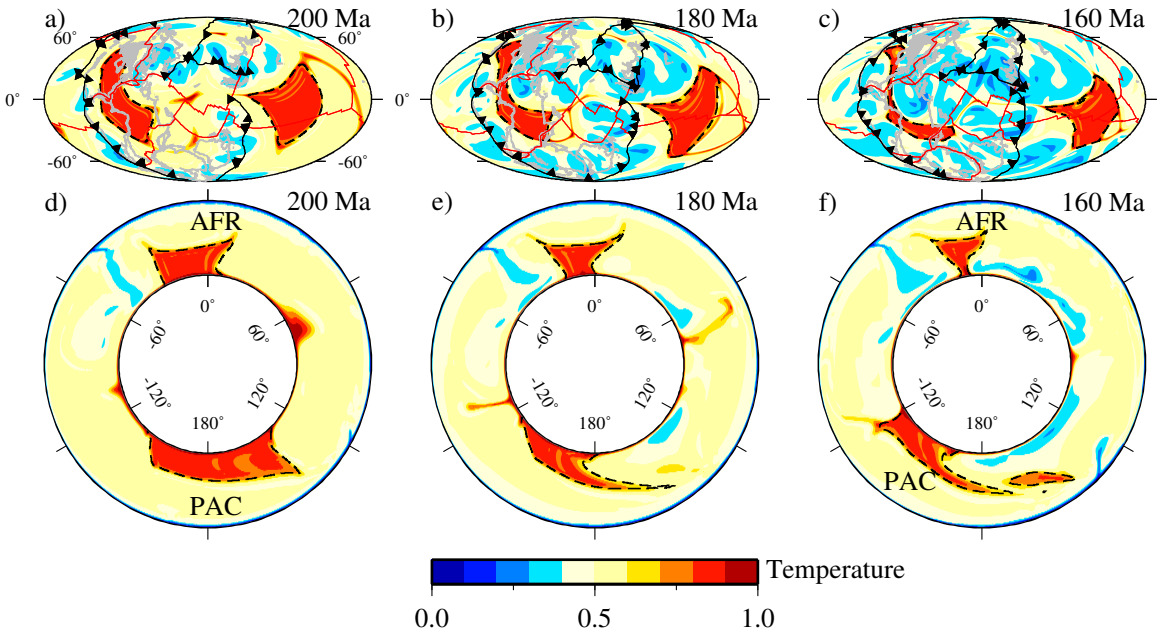

Figure 5.6: BO1 snapshots. (a, b, c) Temperature at 2600 km depth for 200, 180, 160 Ma, respectively. (d, e, f) Equatorial annuli of temperature (0° is the Prime Meridian) for (a, b, c), respectively. For details, see Fig. 5.4 caption.

Additionally, entrainment reduces the size of the domes, particularly the African anomaly.

BO5 does not include a high-K component, but the evolution of the model from 250 to 70 Ma is similar to BO2 (compare Figs. 5.8h,k and Figs. 5.7c,e). In comparison to BO2, BO5 achieves both stable domes and less entrainment (Fig. 5.8), although the domes do not stand as high above the CMB and their edges are less steep. This is particularly evident for the African anomaly. Nevertheless, in these cases the lateral migration of the domes at the CMB is insensitive to the details of the chemically distinct high-K or uniform density material. We therefore expect that BO5 is representative of high-K models with stable domes and minimal entrainment, excluding the vertical extent of the structures.

The domes initially flatten in BO5 because they are more dense than in the previ-

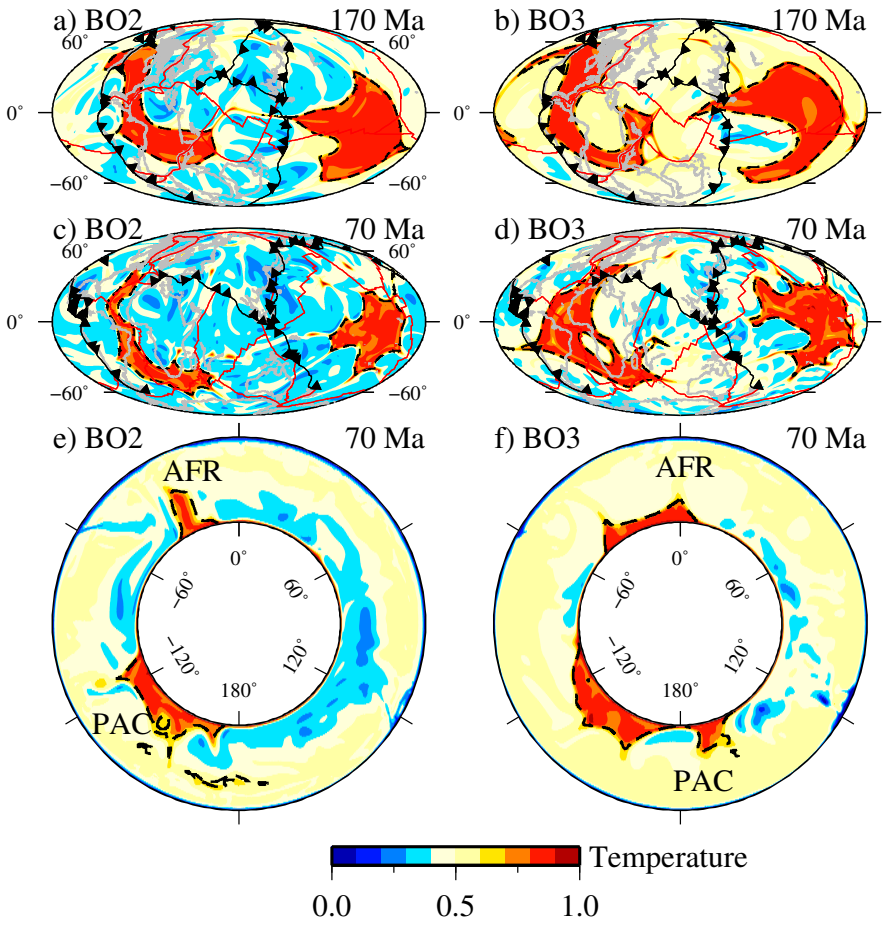

Figure 5.7: BO2 (with assimilation) and BO3 (kinematic only) snapshots. Temperature at 2600 km depth for (a, c) BO2 at 170 and 70 Ma, respectively. (b, d) BO3 at 170 and 70, respectively. (e, f) Equatorial annuli of temperature (0° is the Prime Meridian) for (c, d), respectively. For details, see Fig. 5.4 caption.

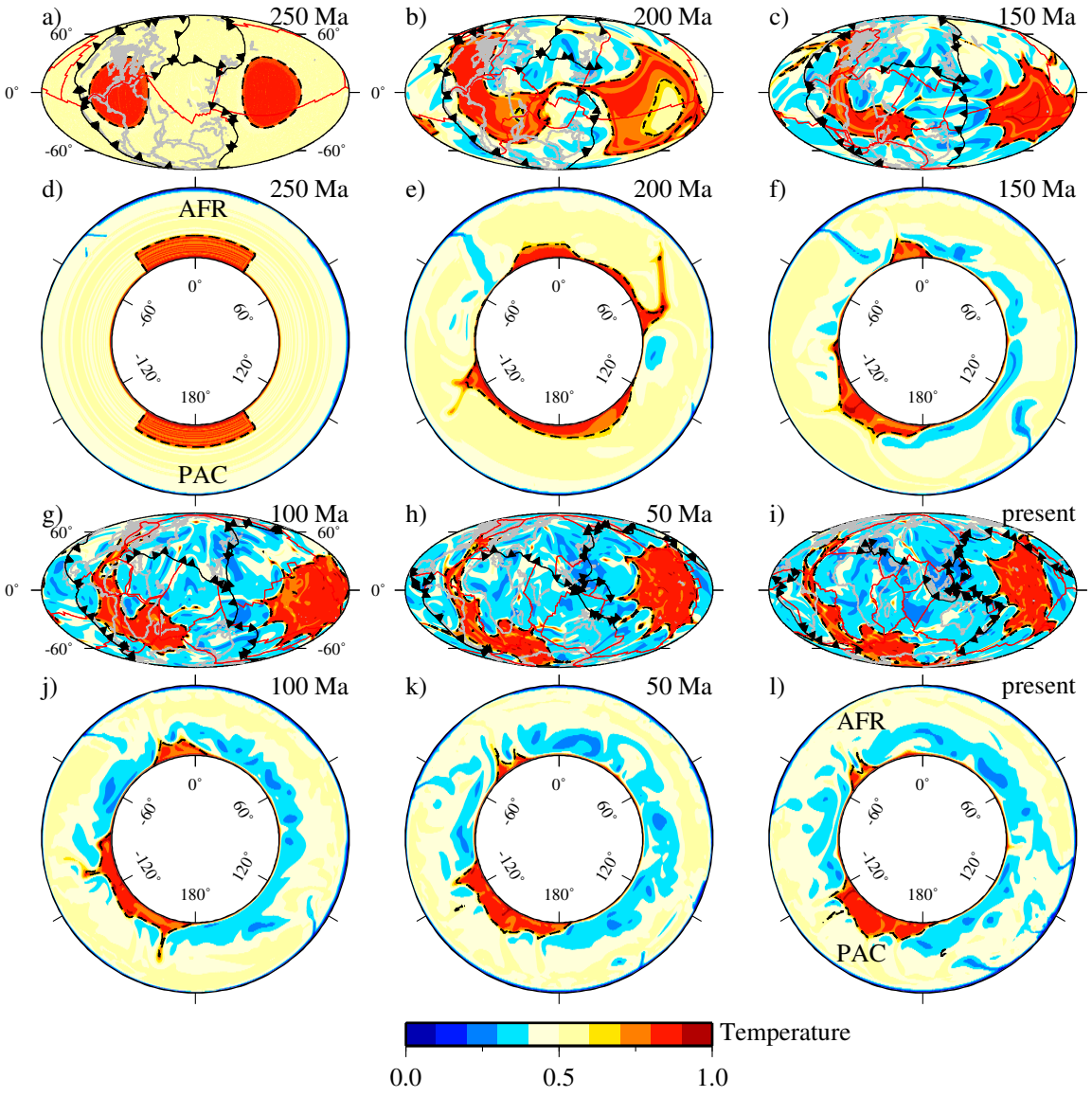

Figure 5.8: BO5 snapshots. (a, b, c, g, h, i) Temperature at 2600 km depth for 250, 200, 150, 100, 50 Ma and present day, respectively. The compositionally distinct material is contoured with black dashes. Ridges and transform faults are represented by red lines and subduction zones are represented by black lines with sawteeth indicating polarity. Reconstructed continent outlines are shown in light grey. (d, e, f, j, k, l) Equatorial annuli of temperature (0° is the Prime Meridian) for (a, b, c, g, h, i), respectively. For details, see Fig. 5.4 caption.

ous high-K models, which increases their CMB footprint throughout the model run. Descending slabs promote thickening of the lower thermal boundary layer and a few short-lived plumes develop at the edges of the domes. The domes deform readily in response to slabs but have sufficient intrinsic density contrast to remain stable at the CMB. They can develop steep edges from boundary tractions caused by slab-induced flow (for example, the eastern edge of the Pacific anomaly, Fig. 5.8l, at -120°). Elsewhere the edges are tapered, such as the western boundary of the Pacific structure (Fig. 5.8l, at 180°).

In BO5, from 250 to 200 Ma, the African and Pacific structures are displaced northwards and southwards, respectively, similar to EX1. Around 200 Ma the Pacific dome is indented by western Pacific slabs that produce two embayments along its boundary (Fig. 5.8b). Slabs from North and South America inhibit the African structure from advancing west while slabs from Africa-Eurasian collision displace material from North Africa (Fig. 5.8c). This elongates the African dome north-south in the northern hemisphere and west-east in the southern hemisphere. The African structure migrates slightly westward as seafloor spreading in the South Atlantic Ocean moves Africa northeastward (Fig. 5.8h). During this time slabs continue to pile up beneath present day Africa (Fig. 5.8i). The Pacific structure is slightly elongated north-south by circum-Pacific slabs from 100 Ma and is centrally located beneath the Pacific Ocean at present (Fig. 5.8i).

Central American slabs slice a small region from the African structure around 230 Ma (small structure to the southwest of the main African anomaly in Fig. 5.8b). This

material migrates southwestward and eventually merges with the Pacific structure at $\sim$ 200 Ma. Additionally, the African dome develops a limb at 200 Ma that extends beneath northwest North America (Fig. 5.8c). This extension merges with the northwest boundary of the Pacific dome around 140 Ma, and slabs eventually detach the limb from the main African structure at 100 Ma.

Geodynamic studies often apply a purely kinematic boundary condition to the top surface of models to produce downwellings at convergent plate margins. However, with this approach it is not clear if the downgoing buoyancy flux is reasonable for the convergence rate and lithospheric buoyancy predicted by geologically consistent plate reconstructions. Therefore, we compare the influence of lithosphere and slab assimiliation (BO2) with a purely kinematic boundary on the top surface (BO3) (Fig. 5.7); all model parameters are otherwise identical. The assimilation method increases slab flux into the lower mantle and the domes have steeper sides and reduced volume.

McNamara and Zhong (2004) demonstrate that an intrinsic viscosity increase in the chemically distinct material can control the style of deformation of the domes. In comparison to BO2, the domes in BO4 have a factor 100 intrinsic viscosity increase. The first downwellings to reach the CMB perturb the lower thermal boundary and generate plumes both at the edges of the domes and away from the structures. From 250 Ma to present, the domes remain as individual coherent structures and do not exchange mass between each other. The topography on the top of the domes is largely unperturbed. At present, the domes are located similarly to BO5 (Fig. 5.8i), except

the African structure is more localized beneath the South Atlantic Ocean and South America and the Pacific structure is rounder.

A reduced Rayleigh number ($Ra = 1.83 \times 10^7$) decreases the sinking rate of slabs because it is equivalent to increasing the background viscosity uniformly (BO6). Convection is more sluggish and its characteristic length-scale larger. From 250 to 150 Ma, the evolution of BO6 is akin to EX1 (Fig. 5.8i) where the domes migrate north and south for the African and Pacific structures, respectively. Around 110 Ma, Central American slabs carve a portion of the African structure which merges with the Pacific dome at $\sim$ 80 Ma. This is similar to the behavior in BO5 although the timescale is increased for the lower Ra model. At present, the African structure is elongated north-south and located beneath the Atlantic Ocean with its eastern margin roughly following the African coastline. The Pacific structure is stretched west-east and located beneath the Pacific Ocean, although preferentially to the west.

5.5 Discussion

The models broadly fall into two classes, depending on whether the domes are predominantly affected by the buoyancy of subducting slabs or by coupling to surface plate motions. The EX models are dominated by coupling to plates and slab buoyancy is weak ("weak-slab models"). In contrast, the BO models are most influenced by downwellings that accumulate at the CMB ("strong-slab models").

At present day the high-K structures are marginally flatter in EX2 and steeper-sided in EX3, relative to EX1. Nevertheless, for the weak-slab models, each dome

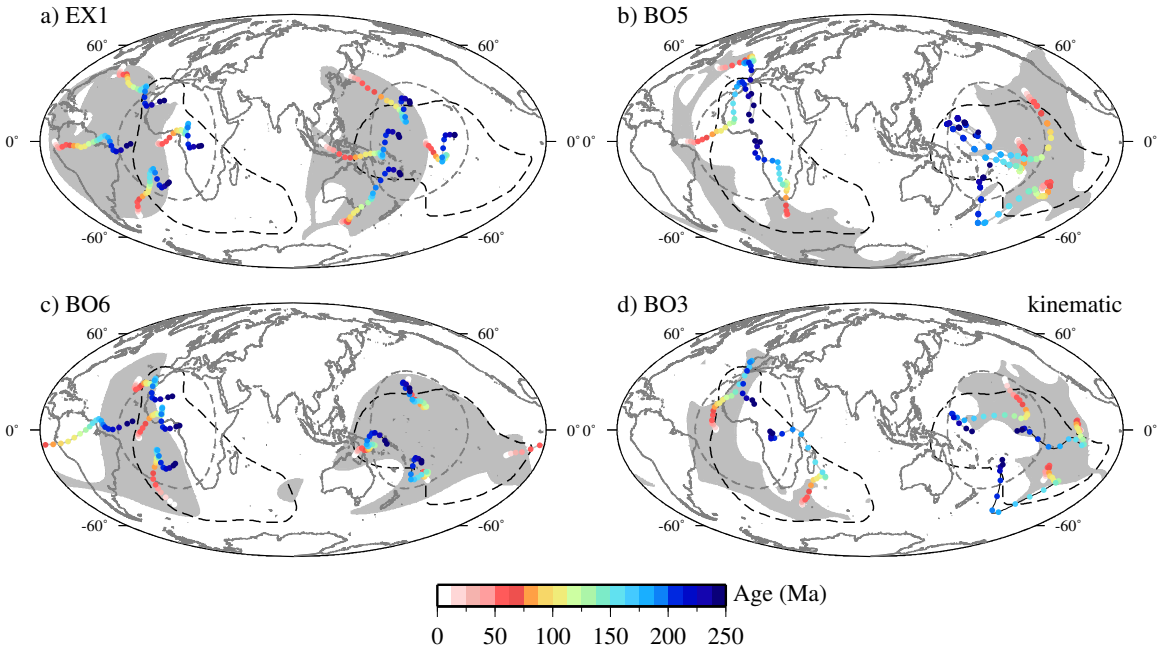

Figure 5.9: Motion and deformation of the domes at 2600 km depth, (a) EX1, (b) BO5, (c) BO6, (d) BO3. The grey-shaded region shows the domes at present day and the dark grey dashes contour the initial position of the domes at 250 Ma. Black dashes delineate the -0.6% S-wave contour from SB10L18 and continent outlines are shown in solid dark grey. Color-coded dots show the movement of the domes from 250 Ma to present day.

follows a similar course as it migrates along the CMB and its present day location is comparable (Fig. 5.9a). From 250 to 150 Ma, the African and Pacific structures move to the north and south, respectively. Dominant motion is then westward from 150 Ma to present day. Both domes are displaced between 35° (Pacific) and 45° (African) west of their initial position at 250 Ma. The Pacific dome lies beneath many of the western Pacific subduction zones, which seems contrary to the hypothesis that chemical layers are displaced away from downwellings (*Davies and Gurnis*, 1986; *McNamara and Zhong*, 2005). However, domes may exist beneath subduction zones if they have only recently initiated. For example, Tonga overlies the edge of the Pacific LLSVP, but is relatively young, having only formed since 45 Ma (*Gurnis et al.*, 2000). A weak slab push force does not overly influence the morphology and location of the structures. Therefore the high-K structures are stable and generally coherent with sharp steep walls, similar to models without slabs (*Tan and Gurnis*, 2005, 2007). However, downwellings can generate significant topography on the domes and locally displace material from some regions of the CMB.

Slabs in the strong-slab models with lithosphere and slab assimilation can propagate to the CMB and deform and displace the domes. From 250 to 200 Ma, the Paleo-Tethys seafloor is relatively old and introduces a large amount of negative buoyancy into the mantle at the trench through slab assimilation. This is compounded by the Tethyan/Mongol-Okhotsk triple junction (trench-trench-trench) (Fig. 5.2), and slabs pile up on the CMB and push material southwestward toward (and ultimately beyond) present day Africa (Fig. 5.9b). This deforms the African structure into an

elongated kidney shape that migrates southwestward after the opening of the South Atlantic Ocean. By contrast, the seafloor is generally younger at the North and South America trenches and the assimilated slabs have less negative buoyancy and a smaller viscosity contrast. Therefore these slabs are weaker and unable to counter the motion of the African dome to the southwest caused by Tethyan slabs. Nevertheless, the ridge-like morphology of the African structure agrees with tomography (Fig. 5.1), waveform modeling (*Ni and Helmberger*, 2003b), and other geodynamic studies (e.g., *McNamara and Zhong*, 2005).

The Pacific structure migrates eastward in the strong slab models, which contrasts with predominant westward motion in the weak-slab models (Fig. 5.9a,b). This is because slabs from the western Pacific subduction zones are dominant in pushing the dome beneath the Pacific Ocean. Tomographic inversions suggest that the basic morphology of this structure is a rounded pile slightly elongated in longitude (Fig. 5.1). Our Pacific dome is generally well located, although slightly extended in the latitudinal direction. This implies that slabs originating from subduction zones in the north and south Pacific (versus the west and east margins) are less dominant in shaping the boundaries of the dome.

A purely kinematic surface boundary condition (BO3) displaces and deforms the domes similarly to models with lithosphere and slab assimilation (Figs. 5.9b,d). In BO3, the African and Pacific structures align more closely with tomography and the Pacific structure is enlongated west–east. However, the vertical extent of the structures varies significantly despite the same high-K parameters (Fig. 5.7). The

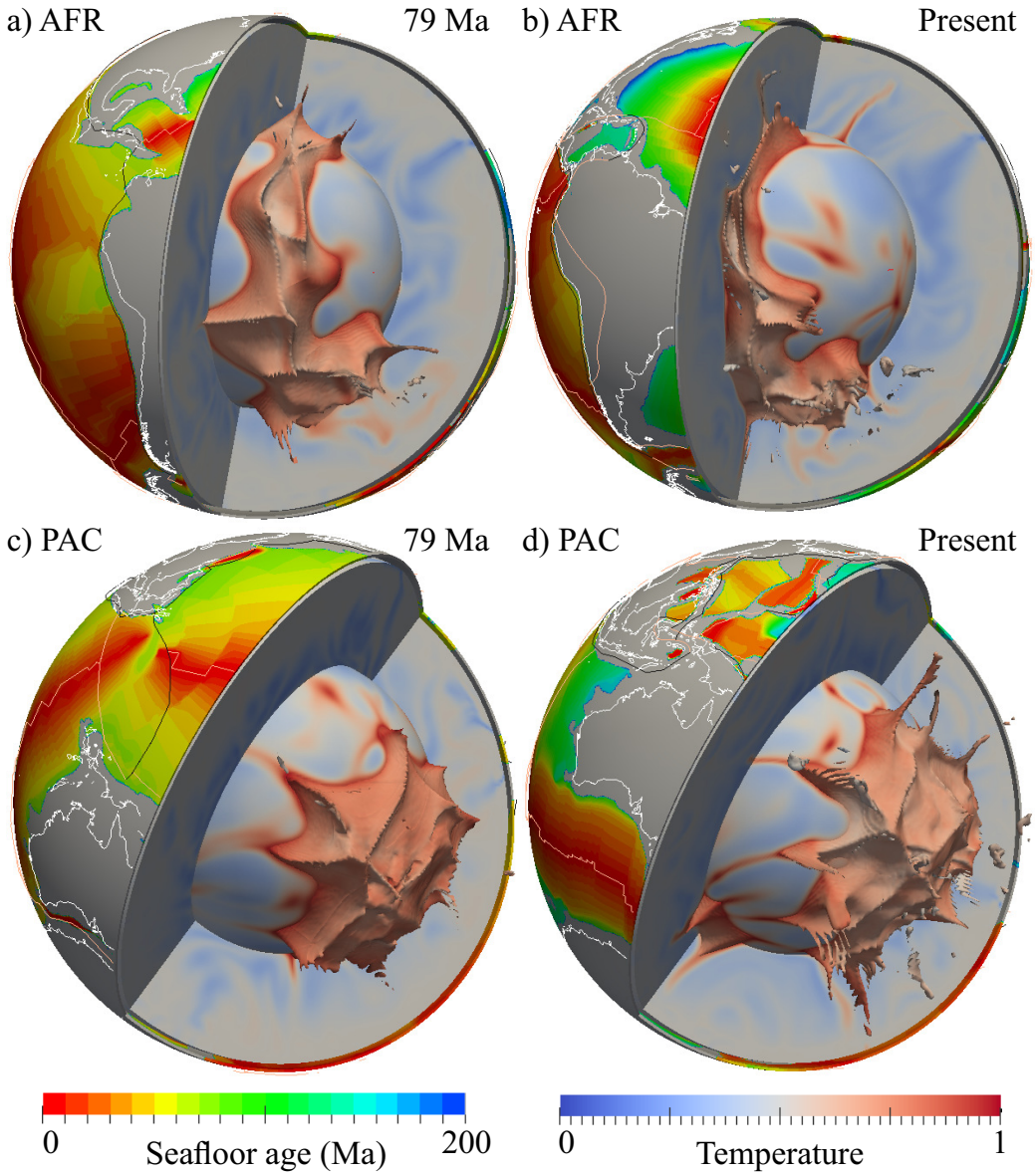

Figure 5.10: 3-D view of the domes in model BO5. African structure at (a) 79 Ma, (b) Present. Pacific structure at (c) 79 Ma, (d) Present. Ridges and transform faults are represented by red lines and subduction zones are represented by black lines. Non-oceanic regions are dark grey and reconstructed continents with present day shorelines are shown in white.

assimilation method increases the down flux into the lower mantle, which has two main effects. First, the stronger slab push steepens the boundaries of the domes. Second, the lower mantle is more efficiently cooled, which raises the HNB of the high-K structures. Therefore, with realistic slab fluxes we expect high-K structures to be less stable than the prediction from models with purely kinematic boundary conditions.

Domes with increased intrinsic viscosity (BO4) do not deform readily in response to slabs, retain a relatively flat top, and become hotter because convection is inhibited (*McNamara and Zhong*, 2004). However, the lateral motion of the structures is not unduly affected because of the free-slip boundary condition at the CMB.

For BO6 ($Ra = 1.83 \times 10^7$), the shape and areal extent of the domes at 2600 km depth correlate fairly well to tomography (Fig. 5.9c). The African structure is displaced too far west although the mismatch is less than for the other models. A sliver of the African dome is carved from the main anomaly by slabs from Central American subduction, which eventually merges with the eastern boundary of the Pacific structure (Fig. 5.9c, leftmost tracer). This demonstrates how mass transfer between the domes (*McNamara et al.*, 2010) may be intimately linked to paleogeography.

The "weak-slab models" arise from the extended-Boussinesq approximation. Adiabatic and viscous heating are often ignored in convection calculations because they are in balance globally (e.g., *Leng and Zhong*, 2008). However, even though some previous studies neglect these terms (*McNamara and Zhong*, 2005; *Zhang et al.*, 2010; *Steinberger and Torsvik*, 2011) they contribute significantly to dissipate the ther-

mal anomaly of slabs in our EX models. It is uncertain how these dissipative terms interact with model parameters and data assimilation.

Steinberger and Torsvik (2011) (hereafter ST11) recently developed a geodynamic model to investigate plume formation at the edges of the domes by prescribing a slab buoyancy flux constrained by global plate reconstructions. BO6 has a comparable Rayleigh number to ST11, yet the location of their domes at the CMB agrees better with seismic tomography. We attribute the difference to two major factors.

First, ST11 apply the plate model to determine the depth-integrated density anomaly of oceanic lithosphere at the trench. This truncates the maximum slab buoyancy to the equivalent of 80 Ma seafloor, whereas our half-space model includes more buoyancy for older slabs. ST11 further reduce slab buoyancy by 21% to account for the subduction of crust and depleted mantle. This means their slab buoyancy is significantly reduced for all subduction zones, and particularly those with subducting plates older than 80 Ma (noteably the Tethyan region at certain ages). The plate model therefore likely mitigates the Tethyan slab push that migrates the African dome in our models to the southwest.

Second, the location of paleosubduction influences the evolution of the domes. The subduction models used in ST11 (*Steinberger and Torsvik*, 2010) and this study (*Seton et al.*, 2012) appear qualitatively similar, but it remains unknown how the evolution of specific regions affects the deep-Earth structure. ST11 also apply a longitudinal shift to subduction zone locations (*van der Meer et al.*, 2010) which improves their dome fit to tomography. Applying a similar rotation to our plate

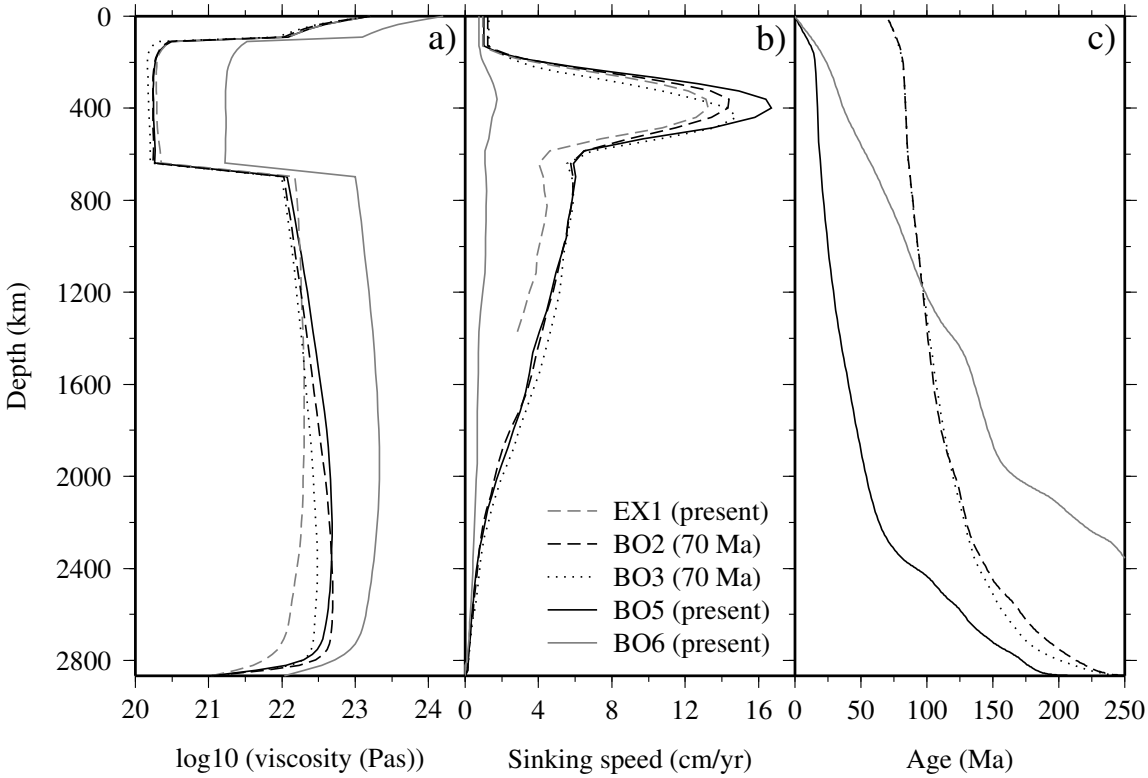

Figure 5.11: Radial profiles for (a) Viscosity, (b) Slab sinking speed, (c) Approximate age of subducted material versus depth, for EX1, BO5, BO6 at present day, and BO5, BO6 at 70 Ma. Sinking speed is determined from positive density anomalies that are greater than 25% of the maximum positive density anomaly at each depth and time (e.g., *Steinberger and Torsvik*, 2010). We set the velocities for depths < 128 km to the value at 128 km depth because they are influenced by data assimilation. The age-depth relation is computed by integrating the time- and depth-dependent slab sinking speed.

history model may enforce the migration of the African dome to the southwest and increase the mismatch.

The slab sinking rate for most of the models here is larger than geological estimates (e.g., 1.2 cm yr^{-1}, *van der Meer et al.*, 2010), except for BO6 (Fig. 5.11c). BO6 has a lower Rayleigh number, which is equivalent to a ubiquitous increase in mantle viscosity (Fig. 5.11a). The Stokes sinking velocity is proportional to the driving density contrast and inversely proportional to the background viscosity. Slabs in EX1

do not retain a strong thermal anomaly for depths > 1400 km because the temperature anomaly is dissipated (Fig. 5.11b). BO2 (with assimilation) and BO3 (purely kinematic) at 70 Ma have approximately the same age-depth relation (Fig. 5.11c), despite the significantly increased lower-mantle slab flux from slab assimilation. This is because cooler material in the lower mantle reduces the driving density contrast for subsequent downwellings. Furthermore, the bulk background viscosity increases through the temperature-dependent rheology, which further reduces the sinking velocity of slabs (Fig. 5.11a). BO3 actually has a marginally faster sinking rate throughout the lower mantle.

We observe plumes forming at the edges of the domes (*Tan et al.*, 2011; *Steinberger and Torsvik*, 2011) from thickened boundary layer pushed toward the structures by slabs. However, plume formation is partly controlled by the maturity (thermal buoyancy available at the CMB) and stability of the lower thermal boundary. Since the most prominant edge-activity occurs during the early stage of the model we relate this largely to the initial condition and the lack of preexisting plume conduits. Furthermore, a 250 Myr integration time is not sufficient for a statistical analysis of plume distribution.

For the high-K structures in the strong-slab models (BO2, BO3, BO4, BO6), the chemical density anomaly is larger than the thermal density anomaly across the whole mantle pressure range. Therefore a HNB does not exist and the high-K material effectively replicates a high-density layer. We consider the density anomaly at the CMB (relative to ambient material) for high-K material, $\Delta\rho_k$, and slab, $\Delta\rho_s$. High-K struc-

tures form when $\Delta\rho_k < 0$, and to ensure they remain stable in the presence of slabs requires $\Delta\rho_k > \Delta\rho_s$. However the latter relation cannot be true because $\Delta\rho_s > 0$. Therefore, slabs will always have a tendancy to sweep beneath high-K structures unless $\Delta\rho_k$ is large and thermal buoyancy no longer dominates at depth. Furthermore, the hot domes have low viscosity and therefore deform readily in response to stresses from stiffer slabs. This further enables slabs to compromise stability by sliding beneath the domes. Higher intrinsic viscosity for the high-K structures can mitigate this effect (BO4).

5.6 Conclusions

We present models that investigate the stability and morphology of high bulk modulus structures in the lower mantle from 250 Ma to present day with constraints from paleogeography. The domes in "weak-slab" models are strongly coupled to plate motions and migrate along the CMB as coherent structures without significant deformation. These structures are displaced 35 to 45 degrees west of their inferred position from seismic tomography. In contrast, the domes in 'strong slab' models deform and migrate along the CMB in response to slab stresses. These models produce a ridge-like anomaly beneath Africa and a rounded pile beneath the Pacific Ocean, similar to previous studies. However, the African structure is displaced too far southwest in comparison to seismic modeling. This is because the progressive assimilation method produces strong Tethyan slabs that deform the African dome into a kidney shape and displace the structure to the southwest beyond present-day Africa.

High-K structures rely on a delicate dynamic balance between thermal and chemical buoyancy; they are almost neutrally buoyant because net density differences are small. Therefore, high-K domes are passive components and the flow is largely imposed by plate motions and slabs. Even "weak slabs" produce notable topography on the surface of the high-K structures and can locally displace material from some downwelling regions (e.g., Central America). "Strong slabs" that are more dense and more viscous than the structures generate stresses that can compromise the stability of the domes at the CMB. Additionally, these slabs can further steepen the edges of high-K structures (or uniform dense layers) and may slide beneath the domes, which can cause the structures to raise off the CMB. Relative to models without slabs, the parameter space for stable high-K structures appears to be reduced.

Finally, our study also outlines a new modeling framework to utilize paleogeography constraints from plate history models to chart the evolution of deep mantle structures. This modeling suggests that the assimilation method increases the slab buoyancy flux relative to models with a purely kinematic boundary condition on the top surface.

Appendix A

Derivation of the mineral physics derivatives

We use the same notation as presented in Chapter 2. Subscripts pv and ppv denote the perovskite (Pv) and post-perovskite (pPv) phase, respectively.

$$\delta vp = \frac{1}{2}\left(\frac{\delta K + 4R_1\delta G/3}{1+4R_1/3} - \delta\rho\right) \tag{A.1}$$

$$\delta vs = \frac{1}{2}(\delta G - \delta\rho). \tag{A.2}$$

For Pv:

$$\delta K_{pv} = \frac{\partial \ln K}{\partial T} dT \tag{A.3}$$

$$\delta G_{pv} = \frac{\partial \ln G}{\partial T} dT \tag{A.4}$$

$$\delta\rho_{pv} = -\bar{\rho}\bar{\alpha}\alpha_0 dT\Delta T \tag{A.5}$$

where dT is a (non-dimensional) temperature perturbation from a reference state.

For pPv:

$$\delta K_{ppv} = \delta K_{pv} + \frac{\partial \ln K}{\partial \Gamma} \tag{A.6}$$

$$\delta G_{ppv} = \delta G_{pv} + \frac{\partial \ln G}{\partial \Gamma} \tag{A.7}$$

$$\delta\rho_{ppv} = \delta\rho_{pv} + \frac{Rb}{Ra}\alpha_0\Delta T \tag{A.8}$$

$$\delta vp_{ppv} = \frac{1}{2}\left(\frac{\delta K_{pv} + 4R_1\delta G_{pv}/3}{1+4R_1/3} - \delta\rho_{pv} + \frac{\frac{\partial \ln K}{\partial \Gamma} + 4R_1\frac{\partial \ln G}{\partial \Gamma}/3}{1+4R_1/3} - \frac{Rb}{Ra}\alpha_0\Delta T\right) \tag{A.9}$$

$$\delta vs_{ppv} = 1/2\left(\delta G_{pv} - \delta\rho_{pv} + \frac{\partial \ln G}{\partial \Gamma} - \frac{Rb}{Ra}\alpha_0\Delta T\right). \tag{A.10}$$

Considering the fractional increase in the S- and P-wave velocities across the Pv-pPv

phase transition:

$$\delta vp_{ppv} = \delta vp_{pv} + \delta vp^{\Gamma} \tag{A.11}$$

$$\delta vs_{ppv} = \delta vs_{pv} + \delta vs^{\Gamma} \tag{A.12}$$

where δvs^{Γ} and δvp^{Γ} are the fractional perturbations to the S- and P-wave velocity, respectively, due to the Pv-pPv phase transition. By substitution:

$$\frac{\partial \ln G}{\partial \Gamma} = 2\delta vs^{\Gamma} + \frac{Rb}{Ra}\alpha_0 \Delta T \tag{A.13}$$

$$\frac{\partial \ln K}{\partial \Gamma} = \left(2\delta vp^{\Gamma} + \frac{Rb}{Ra}\alpha_0 \Delta T\right)(1 + 4R_1/3) - 4R_1/3\frac{\partial \ln G}{\partial \Gamma}. \tag{A.14}$$

Bibliography

Akber-Knutson, S., G. Steinle-Neumann, and P. D. Asimow (2005), Effect of Al on the sharpness of the $MgSiO_3$ perovskite to post-perovskite phase transition, *Geophys. Res. Lett.*, *32*(14), L14,303, doi:10.1029/2005GL023192.

Ammann, M. W., J. P. Brodholt, and D. P. Dobson (2009), DFT study of migration enthalpies in $MgSiO_3$ perovskite, *Phys. Chem. Miner.*, *36*, 151–158, doi: 10.1007/S0029-008-0265-Z.

Ammann, M. W., J. P. Brodholt, J. Wookey, and D. P. Dobson (2010), First-principles constraints on diffusion in lower-mantle minerals and a weak D″ layer, *Nature*, *465*, 462–465, doi:10.1038/nature09052.

Andrault, D., M. Muñoz, N. Bolfan-Casanova, N. Guignot, J.-P. Perrillat, G. Aquilanti, and S. Pascarelli (2010), Experimental evidence for perovskite and post-perovskite coexistence throughout the whole D″ region, *Earth Planet. Sc. Lett.*, *293*(1–2), 90–96, doi:10.1016/j.epsl.2010.02.026.

Auzende, A.-L., J. Badro, F. J. Reyerson, P. K. Weber, S. J. Fallon, A. Addad, J. Siebert, and G. Fiquet (2008), Element partitioning between magnesium silicate

perovskite and ferropericlase: New insights into bulk lower-mantle geochemistry, *Earth Planet. Sc. Lett.*, *269*, 164–174, doi:10.1016/j.epsl.2008.02.001.

Avants, M., T. Lay, and E. J. Garnero (2006), A new probe of ULVZ S-wave velocity structure: Array stacking of ScS waveforms, *Geophys. Res. Lett.*, *33*, L07314, doi: 10.1029/2005GL024989.

Badro, J., G. Fiquet, F. Guyot, J.-P. Rueff, V. V. Struzhkin, G. Vankó, and G. Monaco (2003), Iron partitioning in Earth's mantle: Toward a deep lower mantle discontinuity, *Science*, *300*, 789–791, doi:10.1126/science.1081311.

Badro, J., J.-P. Rueff, G. Vankó, G. Monaco, G. Fiquet, and F. Guyot (2004), Electronic transitions in perovskite: Possible nonconvecting layers in the lower mantle, *Science*, *305*, 383–386, doi:10.1126/science.1098840.

Berryman, J. G. (2000), Seismic velocity decrement ratios for regions of partial melt in the lower mantle, *Geophys. Res. Lett.*, *27*(3), 421–424, doi:10.1029/1999GL008402.

Billen, M. I., and G. Hirth (2007), Rheologic controls on slab dynamics, *Geochem. Geophy. Geosy.*, *8*(8), Q08012, doi:10.1029/2007GC001597.

Burke, K., and T. H. Torsvik (2004), Derivation of large igneous provinces of the past 200 million years from long-term heterogeneities in the deep mantle, *Earth Planet. Sc. Lett.*, *227*(c), 531–538, doi:10.1016/j.epsl.2004.09.015.

Burke, K., B. Steinberger, T. H. Torsvik, and M. A. Smethurst (2008), Plume gener-

ation zones at the margins of large low shear velocity provinces on the coremantle boundary, *Earth Planet. Sc. Lett.*, *265*, 49–60, doi:10.1016/j.epsl.2007.09.042.

Byerlee, J. D. (1978), Friction of rocks, *Pure Appl. Geophys.*, *116*(4–5), 615–626, doi:10.1007/BF00876528.

Catalli, K., S.-H. Shim, and V. Prakapenka (2010), Thickness and Clapeyron slope of the post-perovskite boundary, *Nature*, *463*(7279), 384–384, doi:10.1038/nature08770.

Christensen, U. (1984), Instability of a hot boundary layer and initiation of thermochemical plumes, *Ann. Geophys.*, *2*(3), 311–320.

Christensen, U. R., and D. A. Yuen (1985), Layered convection induced by phase transitions, *J. Geophys. Res.*, *90*(B12), 10,291–10,300, doi:10.1029/JB090iB12p10291.

Cleary, J. R. (1974), The D″ region, *Phys. Earth Planet. In.*, *9*, 13–27, doi:10.1016/0031-9201(74)90076-4.

Cleary, J. R., and R. A. W. Haddon (1972), Seismic wave scattering near the coremantle boundary: A new interpretation of precursors to PKP, *Nature*, *240*, 549–551, doi:10.1038/240549a0.

Crowhurst, J., J. Brown, A. Goncharov, and S. Jacobsen (2008), Elasticity of (Mg,Fe)O through the spin transition of iron in the lower mantle, *Science*, *319*, doi:10.1126/science.1149606.

Davies, G. F. (1999), *Dynamic Earth: plates, plumes, and mantle convection*, Cambridge University Press.

Davies, G. F., and M. Gurnis (1986), Interaction of mantle dregs with convection: lateral heterogeneity at the core-mantle boundary, *Geophys. Res. Lett.*, *13*(13), 1517–1520.

de Koker, N. (2010), Thermal conductivity of MgO periclase at high pressure: Implications for the D″ region, *Earth Planet. Sc. Lett.*, *292*, 392–398, doi: 10.1016/j.epsl.2010.02.011.

Ding, X., and D. V. Helmberger (1997), Modelling D″ structure beneath Central America with broadband seismic data, *Phys. Earth Planet. In.*, *101*, 245–270, doi: 10.1016/S0031-9201(97)00001-0.

Dobson, D. P., and J. P. Brodholt (2005), Subducted banded iron formations as a source of ultralow-velocity zones at the core-mantle boundary, *Nature*, *434*, 371–374, doi:10.1038/nature03385.

Dubrovinsky, L. S., N. A. Dubrovinskaia, S. K. Saxena, H. Annersten, E. Hålenius, H. Harryson, F. Tutti, S. Rekhi, and T. Le Bihan (2000), Stability of ferropericlase in the lower mantle, *Science*, *289*(5478), 430–432, doi:10.1126/science.289.5478.430.

Dziewonski, A., and D. L. Anderson (1981), Preliminary reference Earth model, *Phys. Earth Planet. In.*, *25*(4), 297–356, doi:10.1016/0031-9201(81)90046-7.

Fei, Y., L. Zhang, A. Corgne, H. Watson, A. Riccolleau, Y. Meng, and V. Prakapenka

(2007), Spin transition and equations of state of (Mg,Fe)O solid solutions, *Geophys. Res. Lett.*, *34*, L17307, doi:10.1029/2007GL030712.

Flores, C., and T. Lay (2005), The trouble with seeing double, *Geophys. Res. Lett.*, *32*, L24305, doi:10.1029/2005GL024366.

Garnero, E. J., and D. V. Helmberger (1995), A very slow basal layer underlying large-scale low-velocity anomalies in the lower mantle beneath the Pacific: evidence from core phases, *Phys. Earth Planet. In.*, *91*, 161–176, doi:10.1016/0031-9201(95)03039-Y.

Garnero, E. J., and D. V. Helmberger (1996), Seismic detection of a thin laterally varying boundary layer at the base of the mantle beneath the central-Pacific, *Geophys. Res. Lett.*, *23*(9), 977–980, doi:10.1029/95GL03603.

Garnero, E. J., and D. V. Helmberger (1998), Further structural constraints and uncertainties of a thin laterally varying ultralow-velocity layer at the base of the mantle, *J. Geophys. Res.*, *103*(B6), 12,495–12,509, doi:10.1029/98JB00700.

Garnero, E. J., and A. K. McNamara (2008), Structure and dynamics of Earth's lower mantle, *Science*, *320*, 626–628, doi:10.1126/science.1148028.

Garnero, E. J., and J. E. Vidale (1999), ScP; a probe of ultralow velocity zones at the base of the mantle, *Geophys. Res. Lett.*, *26*(3), 377–380, doi:10.1029/1998GL900319.

Garnero, E. J., D. V. Helmberger, and S. Grand (1993a), Preliminary evidence for a

lower mantle shear wave velocity discontinuity beneath the central Pacific, *Phys. Earth Planet. In.*, *79*, 335–347, doi:10.1016/0031-9201(93)90113-N.

Garnero, E. J., S. P. Grand, and D. V. Helmberger (1993b), Low P-wave velocity at the base of the mantle, *Geophys. Res. Lett.*, *20*(17), 1843–1846, doi:10.1029/93GL02009.

Glatzmaier, G. A., and P. H. Roberts (1995), A three-dimensional convective dynamo solution with rotating and finitely conducting inner core and mantle, *Phys. Earth Planet. In.*, *91*, 63–75, doi:10.1016/0031-9201(95)03049-3.

Goncharov, A. F., B. D. Haugen, V. V. Struzhkin, P. Beck, and S. D. Jacobsen (2008), Radiative conductivity in the Earth's lower mantle, *Nature*, *456*, doi:10.1038/nature07412.

Grand, S. P. (2002), Mantle shear-wave tomography and the fate of subducted slabs, *Phil. Trans. R. Soc. Lond. A*, *360*(1800), 2475–2491, doi:10.1098/rsta.2002.1077.

Gurnis, M., J. Ritsema, H.-J. van Heijst, and S. Zhong (2000), Tonga slab deformation: The influence of a lower mantle upwelling on a slab in a young subduction zone, *Geophys. Res. Lett.*, *27*, 2373–2376, doi:10.1029/2000GL011420.

Gurnis, M., et al. (2012a), Plate tectonic reconstructions with continuously closing plates, *Comput. Geosci.*, *38*, 35–42, doi:10.1016/j.cageo.2011.04.014.

Gurnis, M., D. J. Bower, and N. Flament (2012b), Assimilating lithosphere and slab history in 4-D dynamic Earth models, in preparation.

Hama, J., and K. Suito (2001), Thermoelastic models of minerals and the composition of the Earth's lower mantle, *Phys. Earth Planet. In.*, *125*(1–4), 147–166, doi:10.1016/S0031-9201(01)00248-5.

Hansen, U., and D. A. Yuen (1988), Numerical simulations of thermal-chemical instabilities at the core-mantle boundary, *Nature*, *334*, 237–240, doi:10.1038/334237a0.

Hansen, U., D. A. Yuen, and S. E. Kroening (1991), Effects of depth-dependent thermal expansivity on mantle circulations and lateral thermal anomalies, *Geophys. Res. Lett.*, *18*(7), 1261–1264, doi:10.1029/91GL01288.

Hansen, U., D. Yuen, S. Kroening, and T. Larsen (1993), Dynamical consequences of depth-dependent thermal expansivity and viscosity on mantle circulations and thermal structure, *Phys. Earth Planet. In.*, *77*, 205–223, doi:10.1016/0031-9201(93)90099-U.

Havens, E., and J. Revenaugh (2001), A broadband seismic study of the lowermost mantle beneath Mexico: constraints on ultralow velocity zone elasticity and density, *J. Geophys. Res.*, *106*(B12), 30,809–30,820, doi:10.1029/2000JB000072.

He, Y., and L. Wen (2009), Structural features and shear-velocity structure of the "Pacific Anomaly", *J. Geophys. Res.*, *114*, B02309, doi:10.1029/2008JB005814.

He, Y., L. Wen, and T. Zheng (2006), Geographic boundary and shear wave velocity structure of the "Pacific anomaly" near the core-mantle boundary beneath western Pacific, *Earth Planet. Sc. Lett.*, *244*, 302–314, doi:10.1016/j.epsl.2006.02.007.

Heine, C., R. D. Müller, and C. Gaina (2004), Reconstructing the lost eastern Tethys Ocean basin: Constraints for the convergence history of the SE Asian margin and marine gateways, in *Continent-Ocean Interactions within East Asian Marginal Seas*, *Geophys. Monogr. Ser.*, Vol. 149, edited by P. Clift, P. Wang, W. Kuhnt, and D. Hayes, pp. 37–54, AGU, Washington, D.C., doi:10.1029/GM149.

Helmberger, D., S. Ni, L. Wen, and J. Ritsema (2000), Seismic evidence for ultralow-velocity zones beneath Africa and the eastern Atlantic, *J. Geophys. Res.*, *105*(B10), 23,865–23,878, doi:10.1029/2000JB900143.

Helmberger, D. V., and S. Ni (2005), Seismic modeling constraints on the South African super plume, in *Earth's Deep Mantle: Structure, Composition, Evolution*, *Geophys. Monogr. Ser.*, Vol. 160, edited by R. D. van der Hilst, J. D. Bass, J. Matas, and J. Trampert, pp. 63–81, AGU, Washington, D.C., doi:10.1029/160GM06.

Helmberger, D. V., E. J. Garnero, and X. Ding (1996), Modeling two-dimensional structure at the core-mantle boundary, *J. Geophys. Res.*, *101*(B6), 13,963–13,972, doi:10.1029/96JB00534.

Helmberger, D. V., L. Wen, and X. Ding (1998), Seismic evidence that the source of the Iceland hotspot lies at the core-mantle boundary, *Nature*, *396*, 251–255, doi:10.1038/24357.

Hernlund, J. W., and C. Houser (2008), On the statistical distribution of seismic velocities in Earth's deep mantle, *Earth Planet. Sc. Lett.*, *265*, 423–437, doi: 10.1016/j.epsl.2007.10.042.

Hernlund, J. W., and A. M. Jellinek (2010), Dynamics and structure of a stirred partially molten ultralow-velocity zone, *Earth Planet. Sc. Lett.*, *296*(1–2), 1–8, doi:10.1016/j.epsl.2010.04.027.

Hernlund, J. W., and S. Labrosse (2007), Geophysically consistent values of the perovskite to post-perovskite transition Clapeyron slope, *Geophys. Res. Lett.*, *34*, L05309, doi:10.1029/2006GL028961.

Hernlund, J. W., and P. J. Tackley (2007), Some dynamical consequences of partial melting in Earth's deep mantle, *Phys. Earth Planet. In.*, *162*, 149–163, doi: 10.1016/j.pepi.2007.04.005.

Hernlund, J. W., C. Thomas, and P. J. Tackley (2005), A doubling of the post-perovskite phase boundary and structure of the Earth's lowermost mantle, *Nature*, *434*, 882–886, doi:10.1038/nature03472.

Hier-Majumder, S. (2008), Influence of contiguity on seismic velocities of partially molten aggregates, *J. Geophys. Res.*, *113*, B12205, doi:10.1029/2008JB005662.

Hier-Majumder, S., and J. Revenaugh (2010), Relationship between the viscosity and topography of the ultralow-velocity zone near the core-mantle boundary, *Earth Planet. Sc. Lett.*, *299*(3–4), 382–386, doi:10.1016/j.epsl.2010.09.018.

Hirose, K., R. Sinmyo, N. Sata, and Y. Ohishi (2006), Determination of post-perovskite phase transition boundary in $MgSiO_3$ using Au and MgO pressure standards, *Geophys. Res. Lett.*, *33*(1), L01310, doi:10.1029/2005GL024468.

Hofmeister, A. M. (1999), Mantle values of thermal conductivity and the geotherm from phonon lifetimes, *Science*, *283*, 1699–1706, doi:10.1126/science.283.5408.1699.

Hofmeister, A. M. (2008), Inference of high thermal transport in the lower mantle from laser-flash experiments and the damped harmonic oscillator model, *Phys. Earth Planet. In.*, *170*, 201–206, doi:10.1016/j.pepi.2008.06.034.

Hutko, A. R., T. Lay, E. J. Garnero, and J. Revenaugh (2006), Seismic detection of folded, subducted lithosphere at the core-mantle boundary, *Nature*, *441*, 333–336, doi:10.1038/nature04757.

Hutko, A. R., T. Lay, J. Revenaugh, and E. J. Garnero (2008), Anticorrelated seismic velocity anomalies from post-perovskite in the lowermost mantle, *Science*, *320*, 1070–1074, doi:10.1126/science.1155822.

Hutko, A. R., T. Lay, and J. Revenaugh (2009), Localized double-array stacking analysis of PcP: D″ and ULVZ structure beneath the Cocos Plate, Mexico, Central Pacific and North Pacific, *Phys. Earth Planet. In.*, *173*, 60–74, doi:10.1016/j.pepi.2008.11.003.

Idehara, K., A. Yamada, and D. Zhao (2007), Seismological constraints on the ultralow velocity zones in the lowermost mantle from core-reflected waves, *Phys. Earth Planet. In.*, *165*, 25–46, doi:10.1016/j.pepi.2007.07.005.

Iitaka, T., K. Hirose, K. Kawamura, and M. Murakami (2004), The elasticity of the $MgSiO_3$ post-perovskite phase in the Earth's lowermost mantle, *Nature*, *430*(6998), 442–445, doi:10.1038/nature02702.

Irifune, T. (1994), Absence of an aluminous phase in the upper part of the Earth's lower mantle, *Nature*, *370*, 131–133, doi:10.1038/370131a0.

Ishii, M., and J. Tromp (1999), Normal-mode and free-air gravity constraints on lateral variations in velocity and density of Earth's mantle, *Science*, *285*, 1231–1236, doi:10.1126/science.285.5431.1231.

Ishii, M., and J. Tromp (2004), Constraining large-scale mantle heterogeneity using mantle and inner-core sensitive normal modes, *Phys. Earth Planet. In.*, *146*(1–2), 113–124, doi:10.1016/j.pepi.2003.06.012.

Ita, J., and S. D. King (1994), Sensitivity of convection with an endothermic phase change to the form of the governing equations, initial conditions, boundary conditions, and equation of state, *J. Geophys. Res.*, *99*(B8), 15,919–15,938, doi:10.1029/94JB00852.

Jackson, J. M., J. Zhang, J. Shu, S. V. Sinogeikin, and J. D. Bass (2005), High-pressure sound velocities and elasticity of aluminous $MgSiO_3$ perovskite to 45 GPa: Implications for lateral heterogeneity in Earth's lower mantle, *Geophys. Res. Lett.*, *32*, L21305, doi:10.1029/2005GL023522.

Jarvis, G. T., and D. P. McKenzie (1980), Convection in a compressible fluid with infinite Prandtl number, *J. Fluid Mech.*, *96*(3), 515–583, doi:10.1017/S002211208000225X.

Jellinek, A. M., and M. Manga (2002), The influence of a chemical boundary layer

on the fixity, spacing and lifetime of mantle plumes, *Nature*, *418*, 760–763, doi: 10.1038/nature00979.

Karato, S., and B. B. Karki (2001), Origin of lateral variation of seismic wave velocities and density in the deep mantle, *J. Geophys. Res.*, *106*(B10), 21,771–21,783.

Karato, S.-I., and P. Li (1992), Diffusion creep in perovskite: Implications for the rheology of the lower mantle, *Science*, *255*(5049), 1238–1240, doi: 10.1126/science.255.5049.1238.

Katsura, T., et al. (2009), P-V-T relations of the $MgSiO_3$ perovskite determined by in situ X-ray diffraction using a large-volume high-pressure apparatus, *Geophys. Res. Lett.*, *36*(1), L01305, doi:10.1029/2008GL035658.

Kellogg, L. H., and S. D. King (1993), Effect of mantle plumes on the growth of D$''$ by reaction between the core and mantle, *Geophys. Res. Lett.*, *20*(5), 379–382, doi:10.1029/93GL00045.

Kennett, B. L. N., and E. R. Engdahl (1991), Traveltimes for global earthquake location and phase identification, *Geophys. J. Int.*, *105*, 429–465, doi:10.1111/j.1365-246X.1991.tb06724.x.

Keppler, H., L. S. Dubrovinsky, O. Narygina, and I. Kantor (2008), Optical absorption and radiative thermal conductivity of silicate perovskite to 125 gigapascals, *Science*, *322*, 1529–1532, doi:10.1126/science.1164609.

Kiefer, B., L. Stixrude, and R. M. Wentzcovitch (2002), Elasticity of

(Mg,Fe)SiO_3–perovskite at high pressures, *Geophys. Res. Lett.*, *29*(11), 1539, doi: 10.1029/2002GL014683.

Kito, T., S. Rost, C. Thomas, and E. J. Garnero (2007), New insights into the P- and S-wave velocity structure of the D″ discontinuity beneath the Cocos Plate, *Geophys. J. Int.*, *169*(2), 631–645, doi:10.1111/j.1365-246X.2007.03350.x.

Knittle, E., and R. Jeanloz (1991), Earth's core-mantle boundary: Results of experiments at high pressures and temperatures, *Science*, *251*(5000), 1438–1443, doi: 10.1126/science.251.5000.1438.

Kohler, M. D., J. E. Vidale, and P. M. Davis (1997), Complex scattering within D″ observed on the very dense Los Angeles Region Seismic Experiment passive array, *Geophys. Res. Lett.*, *24*(15), 1855–1858, doi:10.1029/97GL01823.

Kono, Y., T. Irifune, Y. Higo, T. Inoue, and A. Barnhoorn (2010), P–V–T relation of MgO derived by simultaneous elastic wave velocity and in situ x-ray measurements: A new pressure scale for the mantle transition region, *Phys. Earth Planet. In.*, *183*(1–2), 196–211, doi:10.1016/j.pepi.2010.03.010.

Lay, T., and D. V. Helmberger (1983), A lower mantle S-wave triplication and the shear velocity structure of D″, *Geophys. J. Roy. Astr. S.*, *75*(3), 799–837, doi: 10.1111/j.1365-246X.1983.tb05010.x.

Lay, T., E. J. Garnero, and S. A. Russell (2004), Lateral variation of the D″ discontinuity beneath the Cocos Plate, *Geophys. Res. Lett.*, *31*, L15612, doi: 10.1029/2004GL020300.

Lay, T., J. Hernlund, E. J. Garnero, and M. S. Thorne (2006), A post-perovskite lens and D″ heat flux beneath the Central Pacific, *Science*, *314*(5803), 1272–1276, doi:10.1126/science.1133280.

Lay, T., J. Hernlund, and B. A. Buffett (2008), Core-mantle boundary heat flow, *Nat. Geosci.*, *1*, doi:10.1038/ngeo.2007.44.

Leng, W., and S. Zhong (2008), Viscous heating, adiabatic heating and energetic consistency in compressible mantle convection, *Geophys. J. Int.*, *173*, 693–702, doi:10.1111/j.1365-246X.2008.03745.x.

Li, B., and J. Zhang (2005), Pressure and temperature dependence of elastic wave velocity of $MgSiO_3$ perovskite and the composition of the lower mantle, *Phys. Earth Planet. In.*, *151*, 143–154, doi:10.1016/j.pepi.2005.02.004.

Lin, J.-F., and T. Tsuchiya (2008), Spin transition of iron in the Earth's lower mantle, *Phys. Earth Planet. In.*, *170*, 248–259, doi:10.1016/j.pepi.2008.01.005.

Lin, J.-F., D. L. Heinz, H.-K. Mao, R. J. Hemley, J. M. Devine, J. Li, and G. Shen (2003), Stability of magnesiowüstite in Earth's lower mantle, *P. Natl. Acad. Sci. USA*, *100*(8), 4405–4408, doi:10.1073/pnas.252782399.

Lin, J.-F., S. D. Jacobsen, W. Sturhahn, J. M. Jackson, J. Zhao, and C.-S. Yoo (2006), Sound velocities of ferropericlase in the Earth's lower mantle, *Geophys. Res. Lett.*, *33*, L22304, doi:10.1029/2006GL028099.

Lin, J.-F., G. Vankó, S. D. Jacobsen, V. Iota, V. V. Struzhkin, V. B. Prakapenka,

A. Kuznetsov, and C.-S. Yoo (2007), Spin transition zone in Earth's lower mantle, *Science*, *317*, 1740–1743, doi:10.1126/science.1144997.

Lin, S.-C., and P. E. van Keken (2006), Dynamics of thermochemical plumes: 1. plume formation and entrainment of a dense layer, *Geochem. Geophy. Geosy.*, *7*(2), Q02006, doi:10.1029/2005GC001071.

Lithgow-Bertelloni, C., and M. Richards (1998), Dynamics of Cenozoic and Mesozoic plate motions, *Rev. Geophys.*, *36*, 27–78, doi:10.1029/97RG02282.

Liu, L., Y. Tan, D. Sun, M. Chen, and D. Helmberger (2011), Trans-Pacific whole mantle structure, *J. Geophys. Res.*, *116*(B4), B04306, doi:10.1029/2010JB007907.

Loper, D. E., and I. A. Eltayeb (1986), On the stability of the D″ layer, *Geophys. Astro. Fluid*, *36*(3), 229–255, doi:10.1080/03091928608210086.

Luo, S.-N., S. Ni, and D. V. Helmberger (2001), Evidence for a sharp lateral variation of velocity at the core-mantle boundary from multipathed PKPab, *Earth Planet. Sc. Lett.*, *189*(3–4), 155–164, doi:10.1016.S00012-821X(01)00364-8.

Manga, M., and R. Jeanloz (1996), Implications of a metal-bearing chemical boundary layer in D″ for mantle dynamics, *Geophys. Res. Lett.*, *23*(22), 3091–3094, doi: 10.1029/96GL03021.

Mao, W. L., G. Shen, V. B. Prakapenka, Y. Meng, A. J. Campbell, D. L. Heinz, J. Shu, R. J. Hemley, and H.-k. Mao (2004), Ferromagnesian postperovskite silicates

in the D″ layer of the Earth, *P. Natl. Acad. Sci. USA*, *101*(45), 15,867–15,869, doi: 10.1073/pnas.0407135101.

Mao, W. L., et al. (2005), Iron-rich silicates in the Earth's D″ layer, *P. Natl. Acad. Sci. USA*, *102*(28), 9751–9753, doi:10.1073/pnas.0503737102.

Mao, W. L., H.-K. Mao, W. Sturhahn, J. Zhao, V. B. Prakapenka, Y. Meng, J. Shu, Y. Fei, and R. J. Hemley (2006), Iron-rich post-perovskite and the origin of ultralow-velocity zones, *Science*, *312*, 564–565, doi:10.1126/science.1123442.

Marton, F. C., and R. E. Cohen (2002), Constraints on lower mantle composition from molecular dynamics simulations of $MgSiO_3$ perovskite, *Phys. Earth Planet. In.*, *134*(3–4), 239–252, doi:10.1016/S0031-9201(02)00189-9.

Masters, G. (2008), On the possible (1D) seismological signature of the spin crossover in ferropericlase, *Eos Trans. AGU*, *89*(53), Fall Meet. Suppl., Abstract MR23A-04.

Masters, G., G. Laske, H. Bolton, and A. Dziewonski (2000), The relative behaviour of shear velocity, bulk sound speed, and compressional velocity in the mantle: Implications for chemical and thermal structure, in *Earth's Deep Interior: Mineral Physics and Tomography From the Atomic to the Global Scale*, *Geophys. Monogr. Ser.*, Vol. 117, edited by S. Karato, A. M. Forte, R. C. Liebermann, G. Masters, and L. Stixude, pp. 63–87, AGU, Washington, D.C., doi:10.1029/GM117.

Matthews, K. J., A. J. Hale, M. Gurnis, R. D. Müller, and L. DiCaprio (2011), Dynamic subsidence of Eastern Australia during the Cretaceous, *Gondwana Res.*, *19*, 372–383, doi:10.1016/j.gr.2010.06.006.

Matyska, C., and D. A. Yuen (2005), The importance of radiative heat transfer on superplumes in the lower mantle with the new post-perovskite phase change, *Earth Planet. Sc. Lett.*, *234*, 71–81, doi:10.1016/j.epsl.2004.10.040.

Matyska, C., and D. A. Yuen (2006), Lower mantle dynamics with the post-perovskite phase change, radiative thermal conductivity, temperature- and depth-dependent viscosity, *Phys. Earth Planet. In.*, *154*, 196–207, doi:10.1016/j.pepi.2005.10.001.

McNamara, A. K., and S. Zhong (2004), Thermochemical structures within a spherical mantle: Superplumes or piles?, *J. Geophys. Res.*, *109*, B07402, doi: 10.1029/2003JB002847.

McNamara, A. K., and S. Zhong (2005), Thermochemical structures beneath Africa and the Pacific Ocean, *Nature*, *437*, doi:10.1038/nature04066.

McNamara, A. K., E. J. Garnero, and S. Rost (2010), Tracking deep mantle reservoirs with ultra-low velocity zones, *Earth Planet. Sc. Lett.*, *299*(1–2), 1–9, doi: 10.1016/j.epsl.2010.07.042.

Monnereau, M., and D. A. Yuen (2007), Topology of the postperovskite phase transition and mantle dynamics, *P. Natl. Acad. Sci. USA*, *104*(22), 9156–9161, doi: 10.1073/pnas.0608480104.

Moresi, L., and V. Solomatov (1998), Mantle convection with a brittle lithosphere: thoughts on the global tectonic styles of the Earth and Venus, *Geophys. J. Int.*, *133*, 669–682, doi:10.1046/j.1365-246X.1998.00521.x.

Mori, J., and D. V. Helmberger (1995), Localized boundary layer below the Mid-Pacific velocity anomaly identified from a PcP precursor, *J. Geophys. Res.*, *100*(B10), 20,359–20,365, doi:10.1029/95JB02243.

Mosenfelder, J. L., P. D. Asimow, D. J. Frost, D. C. Rubie, and T. J. Ahrens (2009), The $MgSiO_3$ system at high pressure: Thermodynamic properties of perovskite, postperovskite, and melt from global inversion of shock and static compression data, *J. Geophys. Res.*, *114*, B01203, doi:10.1029/2008JB005900.

Murakami, M., K. Hirose, K. Kawamura, N. Sata, and Y. Ohishi (2004), Post-perovskite phase transition in $MgSiO_3$, *Science*, *304*(5672), 855–858, doi: 10.1126/science.1095932.

Murakami, M., K. Hirose, N. Sata, and Y. Ohishi (2005), Post-perovskite phase transition and mineral chemistry in the pyrolitic lowermost mantle, *Geophys. Res. Lett.*, *32*, L03304, doi:10.1029/2004GL021956.

Murakami, M., S. V. Sinogeikin, J. D. Bass, N. Sata, Y. Ohishi, and K. Hirose (2007), Sound velocity of $MgSiO_3$ post-perovskite phase: a constraint on the D″ discontinuity, *Earth Planet. Sc. Lett.*, *259*, 18–23, doi:10.1016/j.epsl.2007.04.015.

Nakagawa, T., and P. J. Tackley (2004), Effects of a perovskite-post perovskite phase change near core-mantle boundary in compressible mantle convection, *Geophys. Res. Lett.*, *31*, L16611, doi:10.1029/2004gl020648.

Naliboff, J. B., and L. H. Kellogg (2006), Dynamic effects of a step-wise increase in

thermal conductivity and viscosity in the lowermost mantle, *Geophys. Res. Lett.*, *33*, L12S09, doi:10.1029/2006GL025717.

Ni, S., and D. V. Helmberger (2001a), Probing an ultra-low velocity zone at the core mantle boundary with P and S waves, *Geophys. Res. Lett.*, *28*(12), 2345–2348, doi:10.1029/2000GL012766.

Ni, S., and D. V. Helmberger (2001b), Horizontal transition from fast to slow structures at the core-mantle boundary; South Atlantic, *Earth Planet. Sc. Lett.*, *187*(3–4), 301–310, doi:10.1016/S0012-821X(01)00273-4.

Ni, S., and D. V. Helmberger (2003a), Seismological constraints on the South African superplume; could be the oldest distinct structure on Earth, *Earth Planet. Sc. Lett.*, *206*, 119–131, doi:10.1016/S0012-821X(02)01072-5.

Ni, S., and D. V. Helmberger (2003b), Ridge-like lower mantle structure beneath South Africa, *J. Geophys. Res.*, *108*(B2), 2094, doi:10.1029/2001JB001545.

Ni, S., and D. V. Helmberger (2003c), Further constraints on the African superplume structure, *Phys. Earth Planet. In.*, *140*, 243–251, doi:10.1016/j.pepi.2003.07.011.

Ni, S., X. Ding, D. V. Helmberger, and M. Gurnis (1999), Low-velocity structure beneath Africa from forward modeling, *Earth Planet. Sc. Lett.*, *170*(4), 497–507, doi:10.1016/S0012-821X(99)00121-1.

Ni, S., X. Ding, and D. V. Helmberger (2000), Constructing synthetics from deep

Earth tomographic models, *Geophys. J. Int.*, *140*, 71–82, doi:10.1046/j.1365-246x.2000.00982.x.

Ni, S., E. Tan, M. Gurnis, and D. V. Helmberger (2002), Sharp sides to the African superplume, *Science*, *296*, 1850–1852, doi:10.1126/science.1070698.

Ni, S., D. V. Helmberger, and J. Tromp (2005), Three-dimensional structure of the African superplume from waveform modelling, *Geophys. J. Int.*, *161*, 283–294, doi: 10.1111/j.1365-246X.2005.02508.x.

Niu, F., and L. Wen (2001), Strong seismic scatterers near the core-mantle boundary west of Mexico, *Geophys. Res. Lett.*, *28*(18), 3557–3560, doi: 10.1029/2001GL013270.

Oganov, A. R., and S. Ono (2004), Theoretical and experimental evidence for a post-perovskite phase of $MgSiO_3$ in Earth's D″ layer, *Nature*, *430*, 445–448, doi: 10.1038/nature02701.

Oganov, A. R., J. P. Brodholt, and G. D. Price (2001), The elastic constants of $MgSiO_3$ perovskite at pressures and temperatures of the Earth's mantle, *Nature*, *411*, 934–937, doi:10.1038/35082048.

Olson, P., and D. A. Yuen (1982), Thermochemical plumes and mantle phase transitions, *J. Geophys. Res.*, *87*(B5), 3993–4002, doi:10.1029/JB087iB05p03993.

Olson, P., G. Schubert, and C. Anderson (1987), Plume formation in the D″-layer and the roughness of the core-mantle boundary, *Nature*, *327*, 409–413.

O'Neill, C., R. D. Müller, and B. Steinberger (2005), On the uncertainties in hot spot reconstructions and the significance of moving hot spot reference frames, *Geochem. Geophy. Geosy.*, *6*, Q04003, doi:10.1029/2004GC000784.

Reasoner, C., and J. Revenaugh (2000), ScP constraints on ultralow-velocity zone density and gradient thickness beneath the Pacific, *J. Geophys. Res.*, *105*(B12), 28,173–28,182, doi:10.1029/2000JB900331.

Ren, Y., E. Stutzmann, R. D. van der Hilst, and J. Besse (2007), Understanding seismic heterogeneities in the lower mantle beneath the Americas from seismic tomography and plate tectonic history, *J. Geophys. Res.*, *112*, B01302, doi:10.1029/2005JB004154.

Revenaugh, J., and R. Meyer (1997), Seismic evidence of partial melt within a possibly ubiquitous low-velocity layer at the base of the mantle, *Science*, *277*(5326), 670–673, doi:10.1126/science.277.5326.670.

Richards, M. A., and D. C. Engebretson (1992), Large-scale mantle convection and the history of subduction, *Nature*, *355*, 437–440, doi:10.1038/355437a0.

Richter, F. (1973), Finite amplitude convection through a phase boundary, *Geophys. J. Roy. Astr. S.*, *35*, 265–276, doi:10.1111/j.1365-246X.1973.tb02427.x.

Richter, F. M., and D. P. McKenzie (1981), On some consequences and possible causes of layered mantle convection, *J. Geophys. Res.*, *86*(B7), 6133–6142, doi:10.1029/JB086iB07p06133.

Ringwood, A. E. (1991), Phase transformations and their bearing on the constitution and dynamics of the mantle, *Geochim. Cosmochim. Ac.*, *55*(8), 2083–2110, doi: 10.1016/0016-7037(91)90090-R.

Ritsema, J., S. Ni, D. V. Helmberger, and H. P. Crotwell (1998), Evidence for strong shear velocity reductions and velocity gradients in the lower mantle beneath Africa, *Geophys. Res. Lett.*, *25*(23), 4245–4248, doi:10.1029/1998GL900127.

Ritsema, J., H. J. van Heijst, and J. H. Woodhouse (1999), Complex shear wave velocity structure imaged beneath Africa and Iceland, *Science*, *286*, 1925–1928, doi:10.1126/science.286.5446.1925.

Ritsema, J., A. Deuss, H. J. van Heijst, and J. H. Woodhouse (2011), S40RTS: a degree-40 shear-velocity model for the mantle from new Rayleigh wave dispersion, teleseismic traveltime and normal-mode splitting function measurements, *Geophys. J. Int.*, *184*(3), 1223–1236, doi:10.1111/j.1365-246X.2010.04884.x.

Rondenay, S., and K. M. Fischer (2003), Constraints on localized core-mantle boundary structure from multichannel, broadband SKS coda analysis, *J. Geophys. Res.*, *108*(B11), 2537, doi:10.1029/2003JB002518.

Rost, S., and J. Revenaugh (2003), Small-scale ultralow-velocity zone structure imaged by ScP, *J. Geophys. Res.*, *108*(B1), 2056, doi:10.1029/2001JB001627.

Rost, S., E. J. Garnero, Q. Williams, and M. Manga (2005), Seismological constraints on a possible plume root at the core-mantle boundary, *Nature*, *435*, 666–669, doi: 10.1038/nature03620.

Rost, S., E. J. Garnero, and Q. Williams (2006), Fine-scale ultralow-velocity zone structure from high-frequency seismic array data, *J. Geophys. Res.*, *111*, doi: 10.1029/2005JB004088.

Rost, S., E. J. Garnero, M. S. Thorne, and A. R. Hutko (2010a), On the absence of an ultralow-velocity zone in the North Pacific, *J. Geophys. Res.*, *115*, B04312, doi:10.1029/2009JB006420.

Rost, S., E. J. Garnero, and W. Stefan (2010b), Thin and intermittent ultralow-velocity zones, *J. Geophys. Res.*, *115*, B06312, doi:10.1029/2009JB006981.

Sakai, T., et al. (2009), Fe–Mg partitioning between perovskite and ferropericlase in the lower mantle, *Am. Mineral.*, *94*, 921–925, doi:10.2138/am.2009.3123.

Schubert, G., D. A. Yuen, and D. L. Turcotte (1975), Role of phase transitions in a dynamic mantle, *Geophys. J. Roy. Astr. S.*, *42*, 705–735, doi:10.1111/j.1365-246X.1975.tb05888.x.

Seagle, C. T., D. L. Heinz, A. J. Campbell, V. B. Prakapenka, and S. T. Wanless (2008), Melting and thermal expansion in the Fe-FeO system at high pressure, *Earth Planet. Sc. Lett.*, *265*(3–4), 655–665, doi:10.1016/j.epsl.2007.11.004.

Seton, M., et al. (2012), Global continental and ocean basin reconstructions since 200 Ma, *Earth-Sc. Rev.*, doi:10.1016/j.earscirev.2012.03.002, (in press).

Shim, S.-H. (2008), The postperovskite transition, *Ann. Rev. Earth Pl. Sc.*, *36*, 569–599, doi:10.1146/annurev.earth.36.031207.124309.

Sidorin, I., and M. Gurnis (1998), Geodynamically consistent seismic velocity predictions at the base of the mantle, in *The Core-Mantle Boundary Region*, *Geodyn. Ser.*, Vol. 28, edited by M. Gurnis, M. Wysession, E. Knittle, and B. A. Buffett, pp. 209–230, AGU, Washington, D.C.

Sidorin, I., M. Gurnis, D. V. Helmberger, and X. Ding (1998), Interpreting D″ seismic structure using synthetic waveforms computed from dynamic models, *Earth Planet. Sc. Lett.*, *163*, 31–41, doi:10.1016/S0012-821X(98)00172-1.

Sidorin, I., M. Gurnis, and D. V. Helmberger (1999a), Dynamics of a phase change at the base of the mantle consistent with seismological observations, *J. Geophys. Res.*, *104*(B7), 15,005–15,023, doi:10.1029/1999JB900065.

Sidorin, I., M. Gurnis, and D. V. Helmberger (1999b), Evidence for a ubiquitous seismic discontinuity at the base of the mantle, *Science*, *286*, 1326–1331, doi: 10.1126/science.286.5443.1326.

Simmons, N. A., and S. P. Grand (2002), Partial melting in the deepest mantle, *Geophys. Res. Lett.*, *29*(11), 1552, doi:10.1029/2001GL013716.

Sinmyo, R., K. Hirose, D. Nishio-Hamane, Y. Seto, K. Fujino, N. Sata, and Y. Ohishi (2008), Partitioning of iron between perovskite/postperovskite and ferropericlase in the lower mantle, *J. Geophys. Res.*, *113*, B11204, doi:10.1029/2008JB005730.

Sleep, N. H. (1988), Gradual entrainment of a chemical layer at the base of the mantle by overlying convection, *Geophys. J. Int.*, *95*, 437–447, doi:10.1111/j.1365-246X.1988.tb06695.x.

Solheim, L. P., and W. R. Peltier (1990), Heat transfer and the onset of chaos in a spherical, axisymmetric, anelastic models of whole mantle convection, *Geophys. Astro. Fluid*, *53*(4), 205–255.

Stacey, F. D. (1977), A thermal model of the Earth, *Phys. Earth Planet. In.*, *15*(4), 341–348, doi:10.1016/0031-9201(77)90096-6.

Stackhouse, S., and J. P. Brodholt (2008), Elastic properties of the post-perovskite phase of Fe_2O_3 and implications for ultra-low velocity zones, *Phys. Earth Planet. In.*, *170*, 260–266, doi:10.1016/j.pepi.2008.07.010.

Stackhouse, S., J. P. Brodholt, J. Wookey, J.-M. Kendall, and G. D. Price (2005), The effect of temperature on the seismic anisotropy of the perovskite and post-perovskite polymorphs of $MgSiO_3$, *Earth Planet. Sc. Lett.*, *230*(1–2), 1–10, doi: 10.1016/j.epsl.2004.11.021.

Stadler, G., M. Gurnis, C. Burstedde, L. C. Wilcox, L. Alisic, and O. Ghattas (2010), The dynamics of plate tectonics and mantle flow: from local to global scales, *Science*, *329*, 1033–1038, doi:10.1126/science.1191223.

Stampfli, G., and G. Borel (2002), A plate tectonic model for the Paleozoic and Mesozoic constrained by dynamic plate boundaries and restored synthetic oceanic isochrons, *Earth Planet. Sc. Lett.*, *196*(1–2), 17–33, doi:10.1016/S0012-821X(01)00588-X.

Steinbach, V., and D. A. Yuen (1994), Effects of depth-dependent properties on the

thermal anomalies produced in flush instabilities from phase transitions, *Phys. Earth Planet. In.*, *86*(1–3), 165–183, doi:10.1016/0031-9201(94)05067-8.

Steinbach, V., U. Hansen, and A. Ebel (1989), Compressible convection in the Earth's mantle: a comparison of different approaches, *Geophys. Res. Lett.*, *16*(7), 633–636.

Steinberger, B., and T. H. Torsvik (2008), Absolute plate motions and true polar wander in the absence of hotspot tracks, *Nature*, *452*(7187), 620–623, doi: 10.1038/nature06824.

Steinberger, B., and T. H. Torsvik (2010), Toward an explanation for the present and past locations of the poles, *Geochem. Geophy. Geosy.*, *11*(6), Q06W06, doi: 10.1029/2009GC002889.

Steinberger, B., and T. H. Torsvik (2011), A geodynamic model of plumes from the margins of Large Low Shear Velocity Provinces, *Geochem. Geophy. Geosy.*, *13*(1), Q01W09, doi:10.1029/2011GC003808.

Sturhahn, W., J. M. Jackson, and J.-F. Lin (2005), The spin state of iron in minerals of Earth's lower mantle, *Geophys. Res. Lett.*, *32*, L12307, doi:10.1029/2005GL022802.

Su, W.-J., and A. M. Dziewonski (1997), Simultaneous inversion for 3-D variations in shear and bulk velocity in the mantle, *Phys. Earth Planet. In.*, *100*(1–4), 35–156, doi:10.1016/S0031-9201(96)03236-0.

Sun, D., and D. Helmberger (2008), Lower mantle tomography and phase change mapping, *J. Geophys. Res.*, *113*, B10305, doi:10.1029/2007JB005289.

Sun, D., T.-R. A. Song, and D. Helmberger (2006), Complexity of D″ in the presence of slab-debris and phase changes, *Geophys. Res. Lett.*, *33*, L12S07, doi: 10.1029/2005GL025384.

Sun, D., E. Tan, D. Helmberger, and M. Gurnis (2007), Seismological support for the metastable superplume model, sharp features, and phase changes within the lower mantle, *P. Natl. Acad. Sci. USA*, *104*(22), 9151–9155, doi: 10.1073/pnas.0608160104.

Sun, D., D. Helmberger, and M. Gurnis (2009a), Chemical piles and deep mantle plumes, in preparation.

Sun, D., D. Helmberger, S. Ni, and D. Bower (2009b), Direct measures of lateral velocity variation in the deep Earth, *J. Geophys. Res.*, *114*, B05303, doi: 10.1029/2008JB005873.

Sun, D., D. Helmberger, and M. Gurnis (2010), A narrow, mid-mantle plume below southern Africa, *Geophys. Res. Lett.*, *37*(9), L09302, doi:10.1029/2009GL042339.

Tackley, P. (2000), Self-consistent generation of tectonic plates in time-dependent, three-dimensional mantle convection simulations 1. pseudoplastic yielding, *Geochem. Geophy. Geosy.*, *1*(1), 1021, doi:10.1029/2000GC000036.

Tackley, P. J. (1998), Three-dimensional simulations of mantle convection with a thermo-chemical basal boundary layer: D″?, in *The Core-Mantle Boundary Region*, *Geodyn. Ser.*, Vol. 28, edited by M. Gurnis, M. Wysession, E. Knittle, and B. A. Buffett, pp. 231–254, AGU, Washington, D.C., doi:10.1029/GD028.

Tackley, P. J. (2002), Strong heterogeneity caused by deep mantle layering, *Geochem. Geophy. Geosy.*, *3*(4), doi:10.1029/2001GC000167.

Tackley, P. J. (2011), Living dead slabs in 3-D: The dynamics of compositionally-stratified slabs entering a "slab-graveyard" above the core-mantle boundary, *Phys. Earth Planet. In.*, *188*(3–4), 150–162, doi:10.1016/j.pepi.2011.04.013.

Tackley, P. J., and S. King (2003), Testing the tracer ratio method for modeling active compositional fields in mantle convection simulations, *Geochem. Geophy. Geosy.*, *4*(4), 8302, doi:10.1029/2001GC000214.

Takeuchi, N., Y. Morita, N. D. Xuyen, and N. Q. Zung (2008), Extent of the low-velocity region in the lowermost mantle beneath the western Pacific detected by the Vietnamese broadband seismograph array, *Geophys. Res. Lett.*, *35*(5), L05307, doi:10.1029/2008GL033197.

Tan, E., and M. Gurnis (2005), Metastable superplumes and mantle compressibility, *Geophys. Res. Lett.*, *32*, L20307, doi:10.1029/2005GL024190.

Tan, E., and M. Gurnis (2007), Compressible thermochemical convection and application to lower mantle structures, *J. Geophys. Res.*, *112*, B06304, doi: 10.1029/2006JB004505.

Tan, E., M. Gurnis, and L. Han (2002), Slabs in the lower mantle and their modulation of plume formation, *Geochem. Geophy. Geosy.*, *3*(11), 1067, doi: 10.1029/2001GC000238.

Tan, E., W. Leng, S. Zhong, and M. Gurnis (2007), Citcoms v3.0 - a compressible thermo-chemical mantle convection code, *Eos Trans. AGU*, *88*(52), Fall Meet. Suppl., Abstract DI14A-01.

Tan, E., W. Leng, S. Zhong, and M. Gurnis (2011), On the location of plumes and lateral movement of thermo-chemical structures with high bulk modulus in the 3-D compressible mantle, *Geochem. Geophy. Geosy.*, *12*(7), Q07005, doi: 10.1029/2011GC003665.

Tateno, S., K. Hirose, N. Sata, and Y. Ohishi (2007), Solubility of FeO in (Mg,Fe)SiO_3 perovskite and the post-perovskite phase transition, *Phys. Earth Planet. In.*, *160*(3-4), 319–325, doi:10.1016/j.pepi.2006.11.010.

Thomas, C., E. J. Garnero, and T. Lay (2004), High-resolution imaging of lowermost mantle structure under the Cocos Plate, *J. Geophys. Res.*, *109*, B08307, doi: 10.1029/2004JB003013.

Thompson, P. F., and P. J. Tackley (1998), Generation of mega-plumes from the core-mantle boundary in a compressible mantle with temperature-dependent viscosity, *Geophys. Res. Lett.*, *25*(11), 1999–2002, doi:10.1029/98GL01228.

Thorne, M. S., and E. J. Garnero (2004), Inferences on ultralow-velocity zone structure from a global analysis of SPdKS waves, *J. Geophys. Res.*, *109*, B08301, doi: 10.1029/2004JB003010.

To, A., B. A. Romanowicz, Y. Capdeville, and N. Takeuchi (2005), 3D effects of sharp

boundaries at the borders of the African and Pacific Superplumes: Observation and modeling, *Earth Planet. Sc. Lett.*, *233*, 137–153, doi:10.1016/j.epsl.2005.01.037.

Torsvik, T. H., K. Burke, B. Steinberger, S. J. Webb, and L. D. Ashwal (2010), Diamonds sampled by plumes from the core-mantle boundary, *Nature*, *466*, doi: 10.1038/nature09216.

Tsuchiya, T., J. Tsuchiya, K. Umemoto, and R. M. Wentzcovitch (2004), Elasticity of post-perovskite $MgSiO_3$, *Geophys. Res. Lett.*, *31*(14), L14603, doi: 10.1029/2004GL020278.

Tsuchiya, T., R. M. Wentzcovitch, C. R. da Silva, and S. de Gironcoli (2006), Spin transition in magnesiowüstite in Earth's lower mantle, *Phys. Rev. Lett.*, *96*, 198501, doi:10.1103/PhysRevLett.96.198501.

van der Meer, D. G., W. Spakman, D. J. J. van Hinsbergen, M. L. Amaru, and T. H. Torsvik (2010), Towards absolute plate motions constrained by lower-mantle slab remnants, *Nat. Geosci.*, *3*, 36–40, doi:10.1038/ngeo708.

Vidale, J. E., and M. A. H. Hedlin (1998), Evidence for partial melt at the core-mantle boundary north of Tonga from the strong scattering of seismic waves, *Nature*, *391*, 682–685, doi:10.1038/35601.

Vincent, A. P., and D. A. Yuen (1988), Thermal attractor in chaotic convection with high-Prandtl-number fluids, *Physical Review A*, *38*(1), 328–334, doi: 10.1103/PhysRevA.38.328.

Wang, Y., and L. Wen (2004), Mapping the geometry and geographic distribution of a very low velocity province at the base of the Earths mantle, *J. Geophys. Res.*, *109*, B10305, doi:10.1029/2003JB002674.

Wang, Y., and L. Wen (2007a), Geometry and P and S velocity structure of the "African Anomaly", *J. Geophys. Res.*, *112*, B05313, doi:10.1029/2006JB004483.

Wang, Y., and L. Wen (2007b), Complex seismic anisotropy at the border of a very low velocity province at the base of the Earths mantle, *J. Geophys. Res.*, *112*, B09305, doi:10.1029/2006JB004719.

Watt, J. P., G. F. Davies, and R. J. O'Connell (1976), The elastic properties of composite materials, *Rev. Geophys.*, *14*(4), 541–563, doi:10.1029/RG014I004P00541.

Wen, L. (2000), Intense seismic scattering near the Earth's core-mantle boundary beneath the Comoros hotspot, *Geophys. Res. Lett.*, *27*(22), 3627–3630, doi:10.1029/2000GL011831.

Wen, L. (2001), Seismic evidence for a rapidly varying compositional anomaly at the base of the Earth's mantle beneath the Indian Ocean, *Earth Planet. Sc. Lett.*, *194*(1–2), 83–95, doi:10.1016/S0012-821X(01)00550-7.

Wen, L. (2002), An SH hybrid method and shear velocity structures in the lowermost mantle beneath the Central Pacific and South Atlantic Oceans, *J. Geophys. Res.*, *107*(B3), doi:10.1029/2001JB000499.

Wen, L. (2006), A compositional anomaly at the Earth's core-mantle boundary as an

anchor to the relatively slowly moving surface hotspots and as as source to the DUPAL anomaly, *Earth Planet. Sc. Lett.*, *246*, 138–148, doi:10.1016/j.epsl.2006.04.024.

Wen, L., and D. V. Helmberger (1998a), A two-dimensional P–SV hybrid method and its application to modeling localized structures near the core-mantle boundary, *J. Geophys. Res.*, *103*(B8), 17,901–17,918, doi:10.1029/98JB01276.

Wen, L., and D. V. Helmberger (1998b), Ultra-low velocity zones near the core-mantle boundary from broadband PKP precursors, *Science*, *279*, 1701–1703, doi:10.1126/science.279.5357.1701.

Wen, L., P. Silver, D. James, and R. Kuehnel (2001), Seismic evidence for a thermochemical boundary at the base of the Earth's mantle, *Earth Planet. Sc. Lett.*, *189*, 141–153, doi:10.1016/S0012-821X(01)00365-X.

Wentzcovitch, R. M., T. Tsuchiya, and J. Tsuchiya (2006), $MgSiO_3$ post-perovskite at D$''$ conditions, *P. Natl. Acad. Sci. USA*, *103*, 543–546, doi:10.1073/pnas.0506879103.

Wessel, P., and L. W. Kroenke (2008), Pacific absolute plate motion since 145 Ma: An assessment of the fixed hot spot hypothesis, *J. Geophys. Res.*, *113*(B6), B06101, doi:10.1029/2007JB005499.

Wessel, P., Y. Harada, and L. W. Kroenke (2006), Toward a self-consistent, high-resolution absolute plate motion model for the Pacific, *Geochem. Geophy. Geosy.*, *7*(3), Q03L12, doi:10.1029/2005GC001000.

Wicks, J. K., J. M. Jackson, and W. Sturhahn (2010), Very low sound velocities in iron-rich (Mg,Fe)O: Implications for the core-mantle boundary region, *Geophys. Res. Lett.*, *37*, L15304, doi:10.1029/2010GL043689.

Williams, Q., and E. J. Garnero (1996), Seismic evidence for partial melt at the base of Earth's mantle, *Science*, *273*, 1528–1530, doi:10.1126/science.273.5281.1528.

Williams, Q., J. Revenaugh, and E. Garnero (1998), A correlation between ultra-low basal velocities in the mantle and hot spots, *Science*, *281*, 546–549, doi: 10.1126/science.281.5376.546.

Wookey, J., S. Stackhouse, J.-M. Kendall, J. Brodholt, and G. D. Price (2005), Efficacy of the post-perovskite phase as an explanation for lowermost-mantle seismic properties, *Nature*, *438*, doi:10.1038/nature04345.

Wysession, M. E., T. Lay, J. Revenaugh, Q. Williams, E. Garnero, R. Jeanloz, and L. H. Kellogg (1998), The D″ discontinuity and its implications, in *The Core-Mantle Boundary Region*, *Geodyn. Ser.*, Vol. 28, edited by M. Gurnis, M. Wysession, E. Knittle, and B. A. Buffett, pp. 273–297, AGU, Washington, D.C., doi: 10.1029/GD028.

Yamazaki, D., and S. Karato (2001), Some mineral physics constraints on the rheology and geothermal structure of Earth's lower mantle, *Am. Mineral.*, *86*(4), 385–391.

Young, C. J., and T. Lay (1987), Evidence for a shear velocity discontinuity in the lower mantle beneath India and the Indian Ocean, *Phys. Earth Planet. In.*, *49*(1–2), 37–53, doi:10.1016/0031-9201(87)90131-2.

Young, C. J., and T. Lay (1990), Multiple phase analysis of the shear velocity structure in the D″ region beneath Alaska, *J. Geophys. Res.*, *95*(B11), 17,385–17,402, doi:10.1029/JB095iB11p17385.

Youngs, B. A. R., and G. A. Houseman (2009), Formation of steep-sided topography from compositionally distinct dense material at the base of the mantle, *J. Geophys. Res.*, *114*, B04404, doi:10.1029/2007JB005487.

Yuen, D. A., and W. R. Peltier (1980), Mantle plumes and the thermal stability of the D″ layer, *Geophys. Res. Lett.*, *7*(9), 625–628, doi:10.1029/GL007I009P00625.

Zhang, N., S. Zhong, W. Leng, and Z.-X. Li (2010), A model for the evolution of the Earth's mantle structure since the early Paleozoic, *J. Geophys. Res.*, *115*, B06401, doi:10.1029/2009JB006896.

Zhang, Y., J. Ritsema, and M. Thorne (2009), Modeling the ratios of SKKS and SKS amplitudes with ultra-low velocity zones at the core-mantle boundary, *Geophys. Res. Lett.*, *36*, L19303, doi:10.1029/2009GL040030.

Zhao, W., and D. A. Yuen (1987), The effects of adiabatic and viscous heatings on plumes, *Geophys. Res. Lett.*, *14*(12), 1223–1226, doi:10.1029/GL014i012p01223.

Zhong, S., M. Zuber, L. N. Moresi, and M. Gurnis (2000), Role of temperature-dependent viscosity and surface plates in spherical shell models of mantle convection, *J. Geophys. Res.*, *105*(B5), 11,063–11,082, doi:10.1029/2000JB900003.

Zhong, S., N. Zhang, Z.-X. Li, and J. H. Roberts (2007), Supercontinent cycles, true

polar wander, and very long-wavelength mantle convection, *Earth Planet. Sc. Lett.*, *261*, 551–564, doi:10.1016/j.epsl.2007.07.049.

Zhong, S., A. McNamara, E. Tan, L. Moresi, and M. Gurnis (2008), A benchmark study on mantle convection in a 3-D spherical shell using CitcomS, *Geochem. Geophy. Geosy.*, *9*(10), Q10017, doi:10.1029/2008GC002048.